Advanced characterization techniques for the knowledge-based design of hard coatings

Dipl.-Ing. Michael Tkadletz

being a thesis in partial fulfilment of the requirements for the degree of a

Doctor of Montanistic Sciences (Dr. mont.)

at the Montanuniversität Leoben

Leoben, July 2015

Financial support by the Austrian Federal Government (in particular from Bundesministerium für Verkehr, Innovation und Technologie and Bundesministerium für Wissenschaft, Forschung und Wirtschaft) represented by Österreichische Forschungsförderungsgesellschaft mbH and the Styrian and the Tyrolean Provincial Government, represented by Steirische Wirtschaftsförderungsgesellschaft mbH and Standortagentur Tirol, within the framework of the COMET Funding Programme is gratefully acknowledged.

Affidavit

I declare in lieu of oath, that I wrote this thesis and performed the associated research myself, using only literature cited in this volume.

Leoben, July 2015

Acknowledgments

My sincerest gratitude is due to Prof. Dr. Christian Mitterer for the possibility to compose this thesis at the Chair of Functional Materials and Material Systems. I am grateful for his supervision, advice, patience and all the confidence he places in me. *Christian, you are leading an outstanding group and I am proud to be a part of it!*

Further I would like to thank ao. Prof. Dr. Jozef Keckes for his support, supervision and especially for his patience. *Jozef, thank you for sharing your knowledge with me and for all the fun we had!*

I am grateful to ao. Prof. Dr. Reinhold Ebner and to Mag. Alexandra Purkarthofer, managing directors of the Materials Center Leoben (MCL), for giving me the opportunity to carry out my thesis within an MCL project. I also would like to thank the MCL staff and co-workers for their support. Especially, I would like to thank Bernhard Sartory for all the support and fruitful discussions, his never ending motivation and the outstanding work he does on the REM-FIB. *Bernhard, we really did great stuff toghether, thank you!*

Also, I would like to express my gratitude to MSc Marianne Penoy and DI Claude Michotte from CERATIZIT Luxembourg and to Dr. Christoph Czettl and DI Markus Pohler from CERATIZIT Austria for their support and the fruitful discussions.

I am also very grateful to the whole “Thin Film Group” and my student co-workers for the great working atmosphere and solidarity. *Special thanks go to Dr. Oliver Jantschner, sharing an office with you was great fun!*

Especially I would like to thank my former office mate and supervisor Dr. Nina Schalk. *Nina, there are no words to thank you for all your support, patience and friendship!*

I would like to thank my parents and my brother for their love and support. *Without you that would never have been possible.*

Last but not least, I would like to express my gratefulness to Daniela, for being by my side, for her patience and for bringing so much love and happiness into my life. *I love you!*

Contents

1. Introduction

Hard and wear resistant coatings are widely used in the field of cutting applications, for dies and molds as well as for other applications under severe operating conditions [1–3]. The high hardness of the coatings results in a significantly improved resistance of the tools against abrasive wear and their high chemical stability is an important factor minimizing chemical degradation due to for example oxidation [4–7]. The demand to constantly improve the production throughput by increasing cutting speed and feed rate further increases the chemical, thermal and mechanical loads on the tools and consequently also on the coatings. This promotes further optimization of the coatings, where typically the chemical composition and microstructure are adjusted or post-deposition treatments, like thermal annealing or mechanical blasting, are applied [8–12]. Thus, microstructural gradients and consequently, gradients of residual stress, hardness and other properties which are either directly or indirectly affected by the microstructure can be tailored [13–15]. Additionally, the high temperatures during service can result in changes of these properties [16,17]. Thus, the interest in cross-sectional and high temperature characterization techniques has been gradually increasing in the recent years. The aim of this thesis is the evaluation and further enhancement of characterization techniques as well as the establishment of novel techniques for advanced characterization of hard coatings.

Within the first part of the thesis, extensive scanning and transmission electron microscopy investigations were performed on the wear tracks formed on arc evaporated TiAlTaN coatings by ball on disk testing at room temperature (RT) and at 700 °C. Special attention was laid to growth defects such as droplets, where focused ion beam (FIB) techniques were used to get a deeper insight into the coating material. A combination of FIB cut and slice techniques, energy dispersive X-ray spectroscopy (EDX) and grayscale image correlation was applied to obtain tomographical images of selected droplets, providing access to the 3 dimensional distribution of their chemical composition.

Recently, Keckes *et al.* [18] introduced an approach, referred to as synchrotron X-ray nanodiffraction, which enables the determination of depth dependent residual strain as a function of the coating thickness with a resolution of 100 nm or even less. Since this approach is limited to nanocrystalline samples, due to the small size of the X-ray beam which is used to probe the sample (beam diameter < 100 nm), it was modified within the second part of the thesis to improve the diffraction statistics for coarse grained materials to a satisfying level. An X-ray beam with dimensions of 100 nm in height and 10 µm width was implemented at the beamline ID 13 at the European Synchrotron Radiation facility (ESRF).

Measurements on exemplary chemical vapor deposited (CVD) α-Al_2O_3 coatings, with a grain size in the micrometer range, have been performed and the line-focused X-ray beam has been evaluated for the determination of different stress gradients, introduced by blasting treatments with different blasting media [19].

Besides techniques for the determination of chemical, microstructural and mechanical properties, a tool-box of methods for the determination of the thermo-physical properties of hard coatings was established within this thesis. The thermo-physical properties of hard coatings have a major influence on the lateral and depth dependent temperature fields during service, which consequently result in stress gradients [20]. Thus, special attention was paid to the investigation of the thermal conductivity, heat capacity and thermal expansion of wear resistant coatings. For TiN, AlN and TiAlN hard coatings grown by physical vapor deposition (PVD), biaxial stress temperature measurements (BSTM) and high temperature X-ray diffraction (XRD) were successfully applied to reveal the coefficient of thermal expansion (CTE) of the samples. Both techniques were compared to each other and the results are discussed. Differential scanning calorimetry (DSC) was used to investigate the specific heat capacity of the samples and a comparison to values provided by the National Institute of Standards and Technology (NIST) is provided. Measurements of the thermal conductivity of TiAlN coatings with different microstructures, using time-domain thermoreflectance (TDTR), were performed to investigate the effect of microstructural design on preservation of a low thermal conductivity which is stable also after annealing at 1200 °C for 120 min. A comprehensive review, representing the last part of the thesis, summarizes the recent advances in the characterization of microstructure, chemical composition and mechanical, tribological and thermo-physical properties of hard coatings, taking into account the methods developed and/or adapted within this work.

2. Coating technology

2.1. Coating deposition

Typical commercially applied hard coatings are based on nitrides or oxides of one or more (transition) metals like Al, Ti or Cr, sometimes doped with small amounts of B, C or Si. Common representatives are TiN, TiAlN or different polymorphs of Al_2O_3. The synthesis of coatings utilizing vapor deposition methods requires the three following basic steps: (*i)* generation of the vapor phase, (*ii)* transport of the vapor from source to substrate and (*iii)* deposition on the substrate by condensation, nucleation and crystal growth. Techniques which are typically used for the deposition of hard and wear resistant coatings are either physical vapor deposition (PVD) or chemical vapor deposition (CVD) [21–23].

2.1.1 Physical vapor deposition

In PVD, solid materials, so called targets, are used which can either consist of metals, alloys or compounds like nitrides or oxides. In the case of compound targets, the targets more or less exhibit the final chemical composition of the coating. Another possibility is reactive PVD, where metallic targets are used to deposit compounds, whereas other components such as N or O are provided as reactive gas [23]. Further, for PVD different processes can be distinguished by the way how the target is evaporated. Two frequently applied techniques are sputter deposition and cathodic arc evaporation (CAE) [22].

A schematic of a typical sputter process for deposition of metal oxides is shown in Fig. 1 [24]. During deposition, a working gas (typically Ar) is provided in the chamber and by applying a voltage between the targets (cathode) and the chamber (anode), a plasma is ignited. Subsequently, the positively charged Ar^+ ions are attracted to the negatively charged target and hit its surface. Due to the momentum transfer from the Ar^+ ions to the target atoms, collision cascades are initiated. Those cascades recoil within the target, and if the energy of the target atoms becomes higher than their binding energy, they are ejected. Typical ionization rates for sputtering are below 1 %, thus, the ejected particles are mainly neutrals. After ejection, the atoms move through the chamber on a ballistic path. If the atoms hit an obstacle, which can be either the chamber wall or the substrate, they condense and a coating is formed. It has to be noted that although Fig. 1 illustrates formation of the compound in the gas phase only, compound formation might occur also at the target as well as at the substrate surface [21,22,25–27].

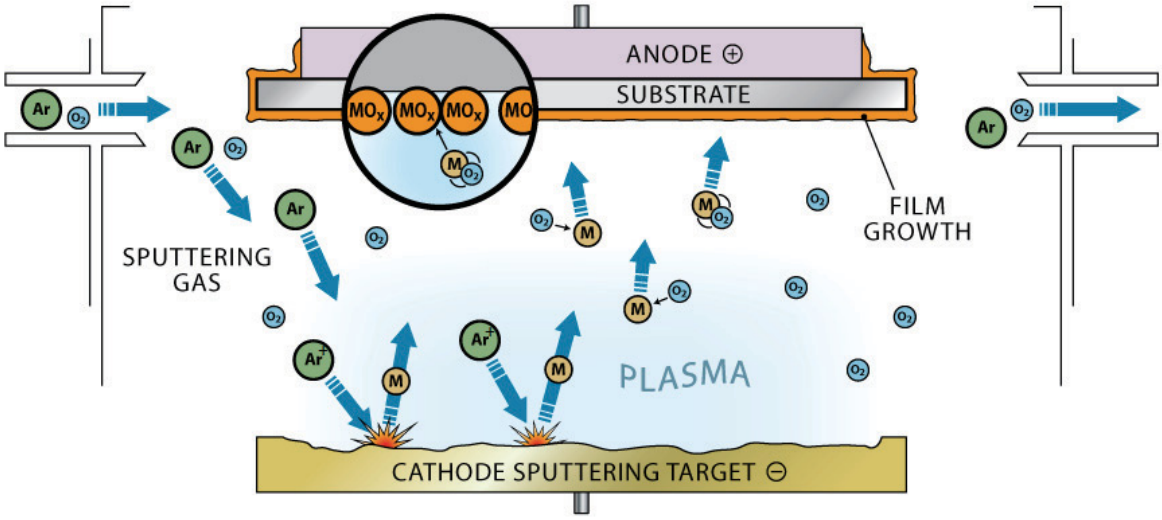

Fig. 1: *Illustration of a typical setup for sputter deposition of metal oxide coatings [24].*

The efficiency of the deposition process and the quality of the deposited coatings can be further enhanced, if unbalanced magnetron sputtering is applied. There, an increase of the plasma ionization rate and the ion flux on the growing film can be achieved by a special arrangement of a magnetic system behind the target. In principle, a magnetron configuration traps electrons within the magnetic field in the target near region, yielding a higher ion density and consequently, increased efficiency of the sputter process and a characteristic erosion track on the target. An unbalanced magnetron configuration allows the magnetic field to reach the negatively biased substrate as the magnetic poles are of different strength. Thus, a certain amount of electrons reaches the substrate near region, again promoting ionization of atoms in that region. The increased amount of ions in the substrate near region results in an a more enhanced ion bombardment of the growing coating, which improves the adherence, increases the density and residual strain of the coating [25,27,28].

In contrast to sputtering, during CAE the evaporation of the target material is achieved by an electric arc discharge moving across the target surface which is shown schematically in Fig. 2a. Due to the high current density (10^6 to 10^{12} A/m²) of the small cathode spot (10^{-8} to 10^{-4} m), i.e. the spot where the arc meets the target, high temperatures arise and the target material is evaporated explosively. CAE processes are usually performed under inert gas or, similar to reactive sputtering, in a reactive gas atmosphere. In contrast to sputter deposition, very high ionization rates of more than 90 % can be reached during CAE. This offers the possibility to adjust the kinetic energy and path of the particles impinging on the substrate

by applying a bias voltage. During CAE, the evaporated species also show higher ionization states, see Fig. 2a where differently charged Ti ions are shown [26,29–32].

One major drawback of CAE is the high number of molten macroscopic particles which are ejected from the target, and subsequently form defects, so called droplets, within the deposited coatings. Droplets are critical as they increase the surface roughness, provide diffusion paths, foster oxidation and deteriorate the mechanical integrity of the coatings [31–35]. A typical droplet surrounded by cavities (indicated by the white arrow) arising from shadowing effects can be found in the secondary electron (SE) scanning electron microscopy (SEM) micrograph in Fig. 2b. The cross-sectional SE-SEM micrograph shown in Fig. 2c was prepared by FIB milling. It reveals a loose bonding of the metallic droplet to the substrate, which was overgrown by the TiAlTaN coating due to the ongoing deposition process. The surrounding cavities can also be identified in the cross-sectional micrograph and are indicated by white arrows.

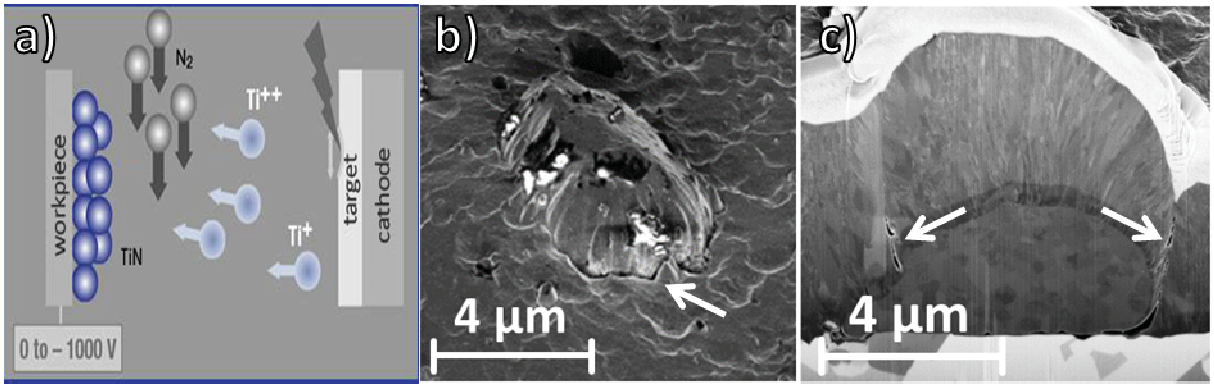

Fig. 2: *(a) Schematic of a CAE deposition process [36]. Secondary electron SEM micrographs of a droplet captured (b) on the surface and (c) within a FIB cross-section [own work].*

During sputtering as well as CAE, the application of a bias voltage, i.e. a negative voltage in the range of -50 to -200 V applied between the substrate and chamber is very common. The bias voltage promotes the ionized particle flux impinging on the growing coating, which results in significantly improved coating properties such as hardness and density. Further, the bias voltage is a common tool to control and adjust the residual stress within PVD coatings [8,23,37,38].

PVD is a line-of-sight process; thus, one inherent drawback is the straightforward deposition which causes shadowing effects and prohibits deposition within cavities such as holes or behind edges. A major advantage of PVD in general is the wide temperature range which can be applied for deposition (from room temperature up to 700 °C) and consequently allows deposition of coatings also on temperature sensitive substrates like e.g. certain steels or even plastics. Further, the wide range of accessible target materials and reactive gases

provides a high flexibility and a vast amount of possible coating materials. The opportunity to adjust the deposition parameters to a great extent allows tailoring of the coating properties to a high degree. Another major advantage of PVD is the possibility to deposit coatings under non-equilibrium conditions, which facilitates the synthesis of metastable coatings like TiAlN [39,40].

2.1.2 Chemical vapor deposition

In CVD, coating deposition is achieved by the use of precursors which can be solid, liquid or gaseous. Solid precursors such as Al, Zr or Hf are typically chlorinated within the deposition plant in order to evaporate and transport the respective species into the reactor. There, the volatile precursors typically react by thermal activation to solid products, which subsequently form the coating. The activation of the chemical reaction can be further assisted by plasma, laser or microwaves in order to decrease reaction temperatures or increase deposition rates. The coatings deposited within this work were synthesized using a so called hot-wall CVD reactor, where the recipient is surrounded by a heating system (furnace) in order to achieve the necessary deposition temperatures, which are in the range of 700 to 1100 °C for hard coatings. An illustration of an industrial scale hot-wall CVD reactor is shown in Fig. 3, including typical examples of solid, liquid and gaseous precursors as well as the vacuum system and a gas scrubber after the reactor [22,27,41–44].

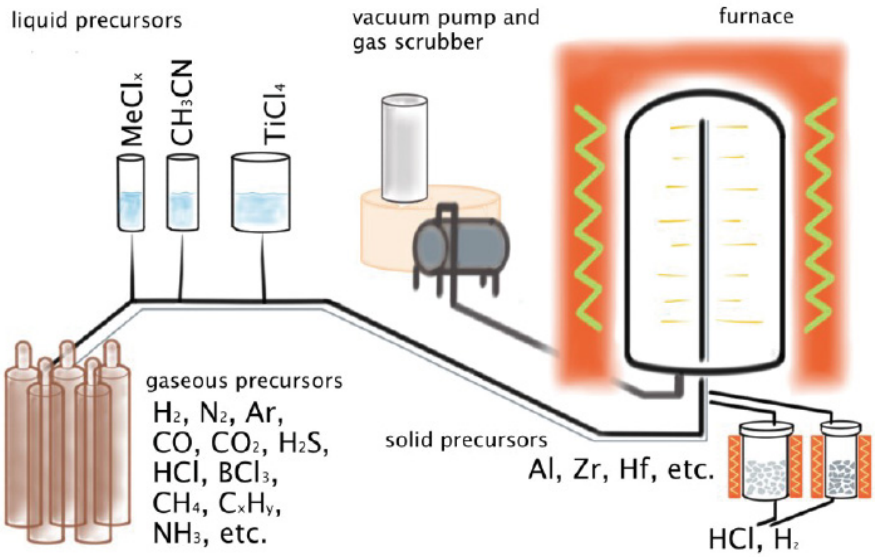

Fig. 3: *Basic components of an industrial scale hot-wall CVD reactor [42].*

During deposition, five basic steps close to the substrate can be distinguished: *(i)* Diffusion of the film forming species through a boundary layer and *(ii)* adsorption on the substrate surface. This step is followed by surface diffusion, *(iii)* the final film forming reaction and *(iv)*

consequential desorption of by-products. In a final step *(v)* the remaining by-products are exhausted from the recipient.

In contrast to PVD, one of the main advantages of CVD is the high so called throwing power, describing the feasibility of coating deposition on out-of-sight areas, enabling deposition also on shadowed parts of the substrate. The large reactors used in CVD allow to process large batch sizes (e.g. 15000 half inch cemented carbide inserts), which makes deposition of rather thick coatings in the range of 10 to 15 µm efficient [21,41,42]. Further, the variation of precursors and reaction conditions, such as for example the gas pressure, provide a high flexibility in terms of the stoichiometry of the deposited coatings.

2.2. Thin film growth

A summary of the basic effects involved in coating growth is illustrated schematically in Fig. 4 [45]. After condensation of the film forming particles on the substrate, two basic surface interactions might occur: *(i)* Surface diffusion or *(ii)* re-evaporation. The particles which diffuse along the surface might be adsorbed at specific sites such as surface asperities, edges or impurities. In addition, there is also the possibility that several particles, diffusing along the surface, form clusters which might either diminish again or grow further, if they reach a critical size which is then referred to as nucleation. A continuous coating grows by coalescence of multiple nuclei. With ongoing deposition, also interdiffusion between substrate and growing coating can take place [21,23,25,45].

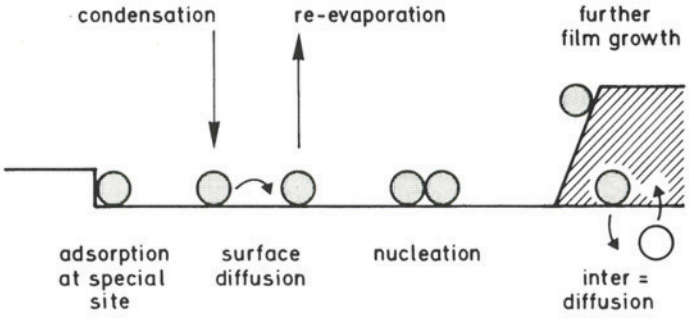

Fig. 4: *Interactions of condensed particles on a surface during coating deposition [45].*

After nucleation, depending on the binding energies of the particles, growth can occur in three different modes which are shown in Fig. 5. Layer-by-layer (Frank-van der Merwe) growth occurs in the case of stronger binding energies between atoms of coating and substrate material (Fig. 5a), while Island (Volmer-Weber) growth occurs when the binding energy between the coating particles is stronger (Fig. 5b). Layer plus island (Stranski-

Krastanov) growth can be observed, if first layer growth is more favorable which changes to island growth after deposition of a uniform layer (Fig. 5c) [25].

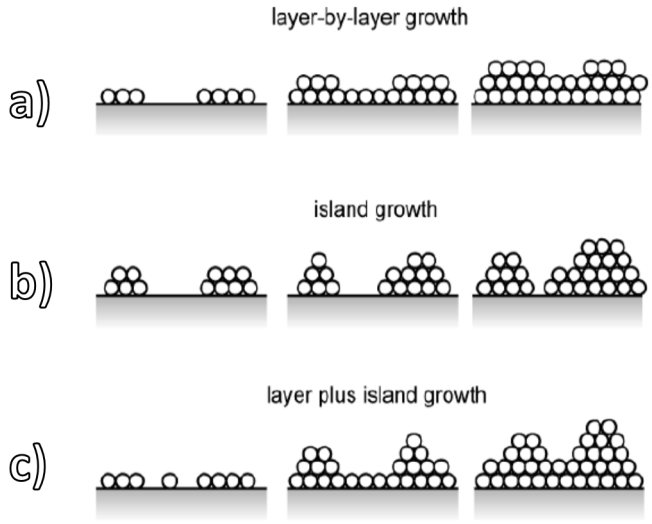

Fig. 5: *Typical growth modes of coatings: (a) layer-by-layer (Frank-van der Merwe), (b) island (Volmer-Weber) and (c) layer plus island (Stranski-Krastanov) growth [25].*

During deposition, the growth kinetics which has a major influence on coating microstructure and thus properties, can be strongly influenced by the deposition parameters such as substrate temperature, working gas pressure and bias voltage. Movchan and Demchishin [46] were the first to introduce a structure zone model (SZM) for thermally evaporated films which relates the homologous temperature (T_s/T_m, where T_s is the substrate temperature and T_m is the melting point of the deposited species) to the observed microstructures. Basically, the model consists of three different zones. In the first zone, at temperatures below 0.3 x T_m, the adatom mobility is rather low and thus, coatings deposited within this zone exhibit a high roughness and porosity caused by shadowing effects. Films deposited in the second zone, ranging from temperatures from 0.3 to 0.45 x T_m, show a smooth surface and columnar, dense structure. The third zone, above temperatures of 0.45 x T_m, is defined by large equiaxed grains formed due to recrystallization and interdiffusion.

Later, Thornton [47] proposed an extended model, including the partial pressure of a working gas in order to expand the model to sputtered coatings. Messier *et al*. [48] introduced a modified model which included the bias voltage during deposition. Both revised models have in common that they added a fourth, so called transition zone between zone 1 and 2, in which the coatings exhibit a dense but fibrous structure. In 2010, Anders [49] revised Thornton´s SZM. By changing the homologous temperature T_s/T_m into the generalized temperature T^*, the revised SZM shown in Fig. 6a also considers the potential

energy of particles arriving at the coating surface. Further, the pressure axis was replaced by a normalized energy (E^*) axis, thus, considering the kinetic energy of bombarding particles. Further, the previously unlabeled third axis is used to represent the coating thickness. With these improvements, the SZM does not only represent the qualitative influence of bias voltage and partial pressure on the coating microstructure, but also expands it to techniques exhibiting a large ion-flux. Finally, Anders' SZM indicates the transition from tensile to compressive stress as well as areas at low and high values for E^* at simultaneous low T^*, which are not accessible.

During CVD the main factors influencing coating growth are the reaction kinetics, basically influenced by the deposition parameters. The deposition temperature, precursor gas throughput (i.e. gas pressure) and the feed gas composition as well as the presence of additional dopants are known to influence the microstructure of the growing coating significantly. A schematic illustrating three typical structure zones occurring in a typical CVD coating is shown in Fig. 6b [44]. There, zone 1 represents a coating consisting of columnar regularly shaped grains with dome-like caps. This can be related to high surface diffusion and uninterrupted grain growth as a result of high deposition temperatures. Within zone 2, the grains are still columnar shaped, but inclined to a certain degree and distinct facets on the surface can be observed. This change in shape from zone 1 to zone 2 can be attributed to lower deposition temperatures and thus, decreased diffusion, as well as increased supersaturation of the precursor mixture. Zone 3 is determined by the growth of rather small equiaxed grains caused by minimized diffusion either at low temperatures, low pressures or high supersaturations [44].

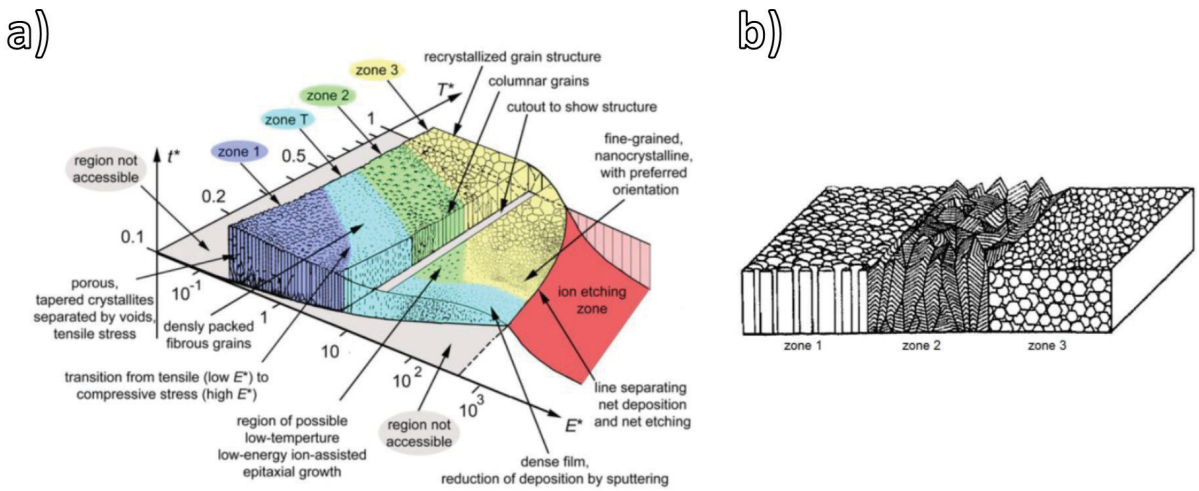

Fig. 6: *Structure zone model for (a) PVD coatings according to Anders [49] and (b) CVD coatings [44].*

2.3. Post-deposition treatment

Post-deposition treatments of hard coatings are widely employed to further improve the coating performance either by surface modification or by improving their mechanical properties. Frequently, mechanical treatments such as polishing, brushing or wet- and dry-blasting are applied in order to smooth the surface and consequently, reduce friction. Moreover, after blasting a certain amount of remaining blasting material, so called transfer material, can be found on the coating surface which further contributes to the modification of the tribological behavior [50,51]. Besides the surface modification, blasting treatments have been proven suitable to tailor the residual stress of hard coatings within a wide range. Depending on the chosen blasting medium and blasting parameters, it is possible to significantly change the residual stress within the uppermost region of the surface or even down into the substrate [10–12,19,52–55].

Especially in the case of CVD coatings, which typically exhibit tensile residual stress in the as-deposited state, blasting has a great potential to improve the mechanical properties [56]. Thus, wet- and dry-blasting has recently gained increasing interest, where not only a change in magnitude but also a change from tensile to compressive stress was reported repeatedly [19,51,52,57,58]. An illustration of a wet-blasting process using two different blasting media is depicted in Fig. 7a [12]. A typical stress-depth gradient computed for blasting of 42CrMo4 steel is presented in Fig. 7b [59], exhibiting a compressive stress maximum below the surface, which is gradually decreasing with increasing depth, ending with a pronounced tensile peak before reaching the initial stress state. According to Schiffner *et al.* [59], the maximum introduced residual stress and its depth below the surface as well as the total affected depth can be significantly influenced by the size of the blasting medium and its velocity. Further, the density and the mechanical properties of the blasting medium, i.e. hardness and Young´s modulus, play an important role. Also blasting parameters like blasting pressure, working distance, working angle and nozzle geometry have significant influence on the effect of the blasting treatment.

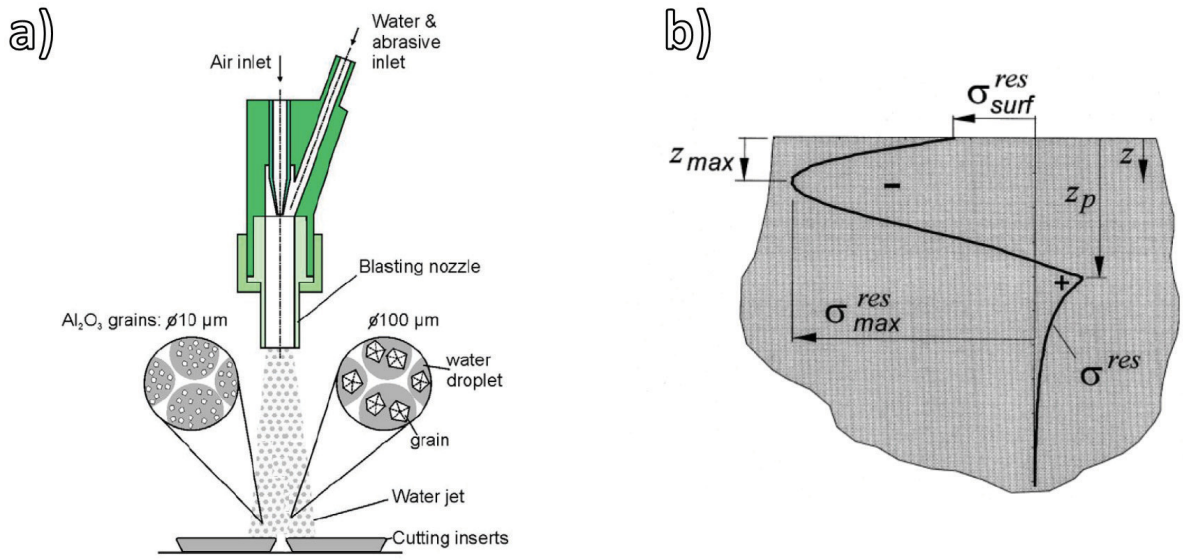

Fig. 7: *(a) Schematic of a wet-blasting process modified after [12]. (b) Resulting stress-depth gradient after blasting of 42CrMo4 steel (computed result) [59].*

Stress-depth gradients similar to Fig. 7b can also be expected for hard coatings. Reports on wet- and dry-blasted hard coatings confirm the influence of the blasting parameters and blasting media. In literature, the determination of the introduced residual stress is often based on depth averaging techniques, thus, only providing mean values of the introduced residual stress. There, the resulting stress values might appear similar, although the actual gradients might be very different. Thus, the determination of the actual stress-depth gradients is crucial to evaluate the impact of the blasting treatment and to relate it to the cutting performance of a coated tool. With ongoing development of depth sensitive techniques such as angle dispersive or energy dispersive XRD measurements, investigations of stress-depth gradients caused by blasting treatments became available but remain still a challenging task [52]. Recently, Keckes *et al.* [18] introduced a technique applying cross-sectional XRD using a synchrotron X-ray beam with a diameter below 100 nm to lamellae of the samples in transmission geometry – a technique which is referred to as synchrotron X-ray nanodiffraction. A schematic of this technique is shown in Fig. 8a [18]. This approach allows the direct determination of the lattice strain and, consequently, stress as a function of the coating thickness with a resolution below 100 nm by recording and evaluating Debye-Scherrer rings for each scanning step. A critical comparison of a nanodiffraction measurement and a depth sensitive lab based approach combined with energy dispersive synchrotron investigations performed on a dry-blasted sample is shown in Fig. 8b [57]. The comparison reveals excellent agreement with Hertzian theory and computed results in terms of the shape of the stress-depth gradient. Also the stress magnitude obtained by both measurements is in good agreement. However, in contrast to X-ray nanodiffraction, the lab

based approach does not allow to resolve the distinct stress relief near the surface, which is a common effect after blasting. Thus, the described X-ray nanodiffraction technique offers the possibility to investigate the effect of blasting treatments on hard coatings with outstanding resolution and precision rather easily.

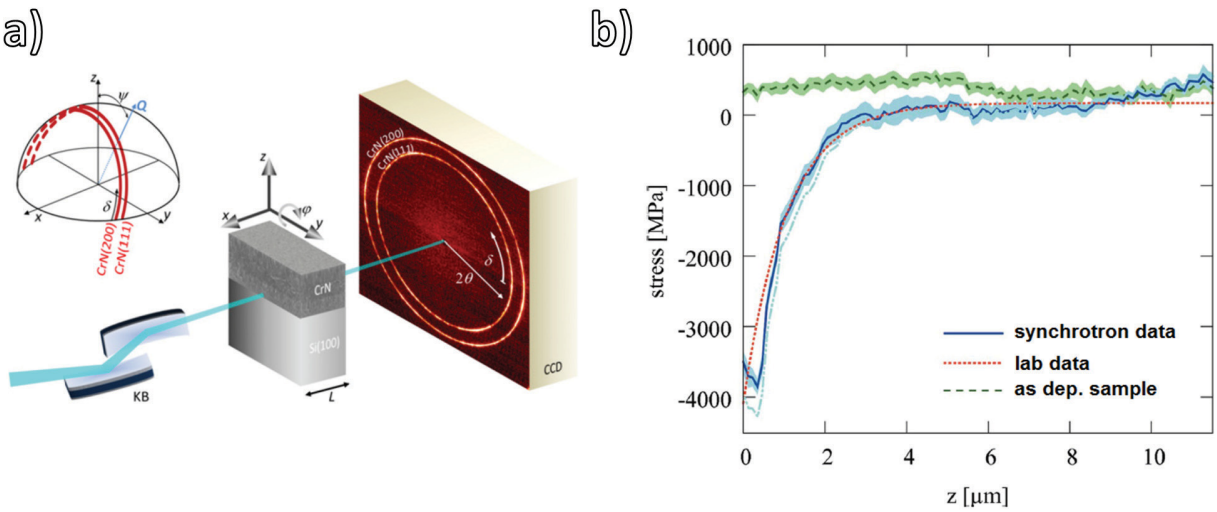

Fig. 8: *(a) Schematic of the synchrotron X-ray nanodiffraction setup [18]. (b) Comparison of laboratory and synchrotron measurements of a blasted TiN sample [57].*

Besides the already mentioned mechanical post treatments, also thermal post treatment strategies might be applied to certain hard coatings in order to increase their hardness by age hardening or to reduce the coefficient of friction. Fig. 9a [60] shows the evolution of the hardness of a TiAlN coating as a function of the annealing temperature, where the peak value around 900 °C is attributed to age hardening and the decreasing hardness at higher annealing temperatures to the formation of wurtzitic AlN domains. In comparison, the TiN reference shows a decreasing hardness starting already at annealing temperatures of 400 °C due to recovery of stresses and recrystallization [60,61]. Friction reduction can be either achieved by out diffusion of elements forming e.g. rutile [51], which acts as lubricant, or by deposition of solid lubricants such as carbon islands on the coating surface [62]. In Fig. 9b [62], a SEM micrograph of a carbon deposit on a TiAlTaN hard coating is shown which was formed during annealing in methane at 900 °C for 1 h. Due to this carbon deposit, the coefficient of friction of the coatings could be decreased from 0.6 to 0.2 [62].

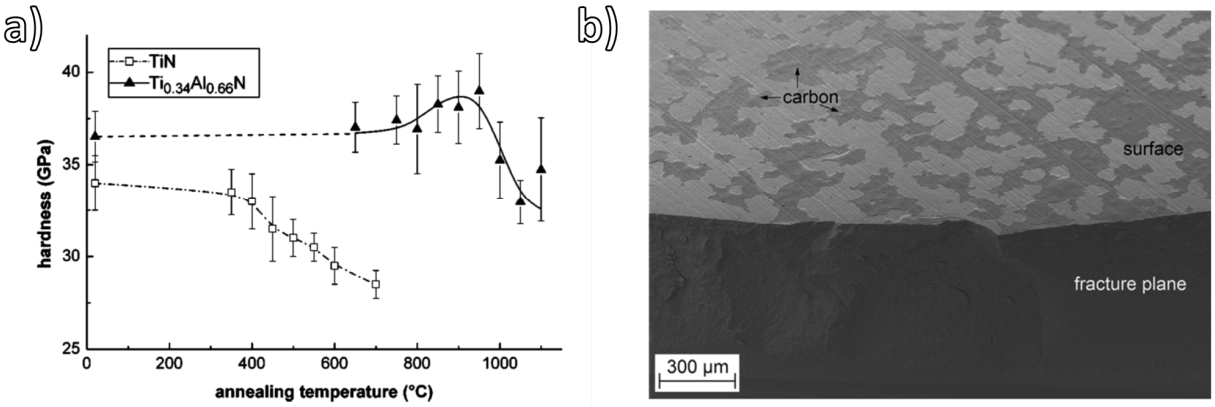

Fig. 9: *(a) Evolution of hardness of TiN and TiAlN with increasing annealing temperature [60]. (b) SEM micrograph showing an inhomogeneous carbon deposit on top of a TiAlTaN coating, responsible for low friction behavior [62].*

3. Hard coating materials

3.1. TiAlN Coatings

In cutting applications, TiAlN based coatings are frequently applied due to their outstanding mechanical properties at room temperature as well as at elevated temperatures. Since the deposition of TiAlN utilizing CVD is still very challenging, the majority of available TiAlN coated tools are produced by PVD. The stable structure of TiN is the face centered cubic (fcc) rock-salt structure, exhibiting a reasonable hardness and wear resistance. However, the oxidation resistance of TiN is rather poor, which usually limits the lifetime and operating temperature during cutting. AlN exhibits a wurtzitic (w) structure with a significantly lower hardness, thus, it is usually not used for cutting applications [39,63,64]. However, the addition of Al to TiN leads to the formation of a metastable fcc-$Ti_{1-x}Al_xN$ solid solution by substitution of Ti by Al atoms in the fcc lattice up to x values of about 0.65 to 0.75, as shown in Fig. 10 [65]. Thereby, an increasing Al content results in an increasing hardness and consequently enhanced wear resistance. Further, the oxidation resistance is significantly improved due to the formation of a stable Al_2O_3 scale on the coating surface [63,66,67]. Above x values of 0.65 to 0.75, the wurtzitic structure becomes predominant, where Al atoms are substituted by Ti atoms [33,68–70]. The change from fcc to wurtzite at high x values results in a pronounced decrease in hardness and wear resistance [33,66,67,70].

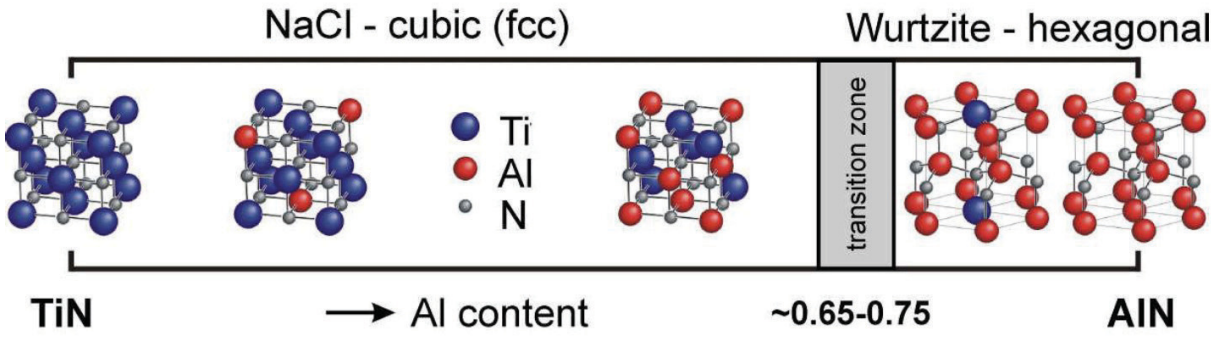

Fig. 10: *Evolution of crystal structure of $Ti_{1-x}Al_xN$ as a function of the Al content [65].*

At temperatures above 800 °C, the metastable fcc-$Ti_{1-x}Al_xN$ is known to undergo spinodal decomposition into fcc-TiN rich and fcc-AlN rich domains. This results in a significant increase in hardness due to age hardening caused by coherency strains (see Fig. 9a). If the temperature is further increased, the metastable fcc-AlN domains transform into stable w-AlN, resulting in deterioration of hardness and wear resistance [33,60,70].

Recently, alloying of transition metals as a third component to the TiAlN system has been intensively investigated [71,72]. Possible transition-metal-nitride candidates for alloying,

including some important properties as well as their relative lattice mismatch with respect to a fcc-TiAlN reference, are depicted in Fig. 11a [8]. The corresponding increase in hardness due to alloying as well as the hardness evolution due to annealing of selected coatings is shown in Fig. 11b [8]. For alloying with Hf or Nb a significant increase in hardness at room temperature can be observed, while the age hardening effect is less pronounced. Alloying with Y slightly increases the hardness at room temperature, but with increasing annealing temperature the hardness deteriorates dramatically. Alloying with Ta results in the most pronounced increase in hardness at room temperature, which can be retained during annealing although no distinct age hardening can be observed. Further, a significantly improved tribological behavior as well as increased oxidation resistance can be related to alloying with Ta. Due to the significant positive effect of Ta, TiAlTaN coatings are today standard coatings for cutting applications.

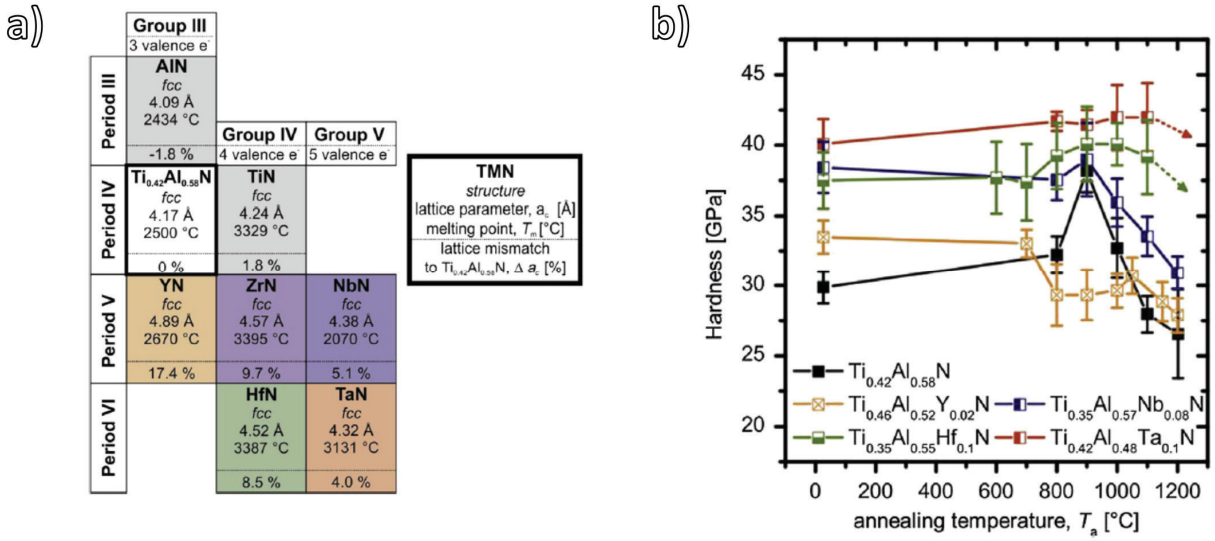

Fig. 11: *(a) Selection of transition metal nitrides suitable as candidates for alloying to TiAlN and (b) their effect on the hardness and age hardening [8].*

Mayrhofer *et al.* [56,73] reported on the influence of microstructure and residual stress on the mechanical properties, in particular the hardness, of various sputtered hard coatings, see Fig. 12a [73]. The residual stress can be tailored by, e.g., varying the bias voltage during deposition. The respective microstructure formed at these different bias voltages enables to adjust the mechanical properties of the deposited coatings with respect to their thickness, as recently shown by Daniel *et al.* for sputtered CrN coatings [74]. Thereby, the X-ray nanodiffraction approach [18] described in the previous section and cross-sectional nanoindentation measurements [74] can be helpful tools to investigate the microstructural evolution of hard coatings. Exemplary, strain plots derived from X-ray nanodiffraction measurements on two different TiAlN coatings can be found in Figs. 12b and c. Both coatings

were ~6 µm thick. During deposition, the bias voltage of the coating shown in Fig. 12b was changed from -50 V to -40 V after half of the deposition time, resulting in a significant reduced residual compressive strain. For the sample shown in Fig. 12b, the bias voltage was -40 V for the initial third of the deposition, followed by -50 V for the second third and -40 V for the last third. Again it can be observed that increasing the bias voltage leads to significantly increased residual compressive strain. The quantitatively determined strain values for both coatings are comparable for -40 V as well as for -50 V bias voltage. Beneficial design sequences, which still need to be determined, might be a key to further enhance TiAlN based coatings.

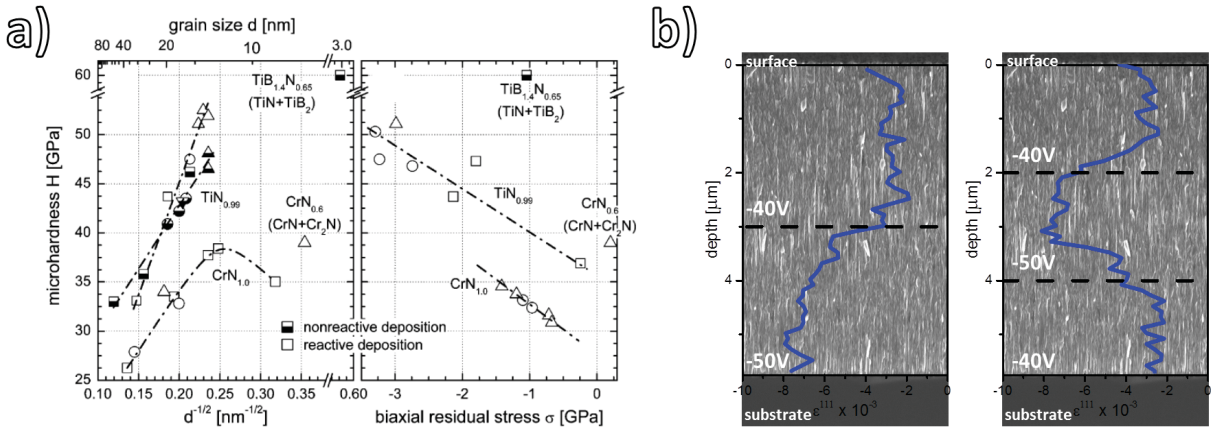

Fig. 12: *(a) Hardness of different sputtered hard coatings as a function of grain size and residual stress [73]. (b) Variation of bias voltage during deposition of sputtered TiAlN resulting in a pronounced strain variation [own work].*

3.2. Al_2O_3 Coatings

Al_2O_3 coatings are widely employed for cutting tools due to their chemical inertness, corrosion resistance and high hardness, also at elevated temperatures. Since the deposition of these coatings is still very challenging using PVD, commercially available Al_2O_3 hard coatings on cemented carbide inserts are typically deposited using CVD [75–77]. They usually exhibit a multilayered architecture consisting of a few hundred nm thick TiN adhesion layer, followed by a TiCN baselayer of 6 to 10 µm thickness. After deposition of the TiCN layer, usually a bonding/nucleation layer of a few 100 nm is deposited, which is followed by the actual Al_2O_3 layer of 6 to 10 µm thickness [19,50,51,78].

Al_2O_3 exists in several polymorphs (α, κ, γ, θ, δ, χ and η), with α-Al_2O_3 being the stable phase. Using CVD, usually either κ- or α-Al_2O_3 are deposited due to their favorable mechanical properties and wear resistance [79]. In the early years of CVD, the metastable κ-modification, which exhibits a primitive orthorhombic structure, was predominant, because the deposition of the stable α-Al_2O_3 polymorph was not possible [75,80–82]. At elevated temperatures, the metastable κ-Al_2O_3 transforms into the stable α-Al_2O_3 which results in a volume shrinkage of approximately 7 %. Consequently, so called secondary crack networks are formed which deteriorate coating cohesion and thus performance [80,83,84]. Further, several authors have shown that not only temperature but also other parameters like precursor gas mixture, deposition time, doping agents and mechanical activation strongly influence the $\kappa \rightarrow \alpha$ transformation [77,85]. Thus, a significant advancement of CVD Al_2O_3 was the introduction of directly nucleated α-Al_2O_3 by utilization of a nucleation layer between TiCN and Al_2O_3 [80,83,86,87].

The α-Al_2O_3 polymorph has a rhombohedrally centered hexagonal lattice belonging to the trigonal system, which is often described as a quasi-hexagonal close packed oxygen superlattice with Al atoms occupying two thirds of the octahedral interstices [80,83]. As a result of this structure, many properties of α-Al_2O_3 are clearly anisotropic, e.g., its mechanical properties. The direction dependent Young´s modulus of α-Al_2O_3, perpendicular to the corresponding surface, calculated from the single crystal elastic constants is shown in Fig. 13a [88,89]. The hardness and Young´s modulus of single crystalline CVD α-Al_2O_3 coatings, grown epitaxially on single crystalline sapphire substrates, determined by nanoindentation measurements, are shown in Fig. 13b. Although nanoindentation measurements do not provide data for one exclusive direction, as the strain induced by the indenter is multiaxial, a significant influence of the crystal orientation on the hardness and Young´s modulus can be observed. Similar to Fig. 13a, the coating with the (0001)

orientation (c-axis perpendicular to coating surface) shows the highest hardness and Young´s modulus, followed by the (11$\bar{2}$0) oriented coating (c-axis parallel to coating surface), whereas the (1$\bar{1}$02) oriented coating revealed the lowest values, which is most likely caused by pronounced twinning along the pyramidal plane [88].

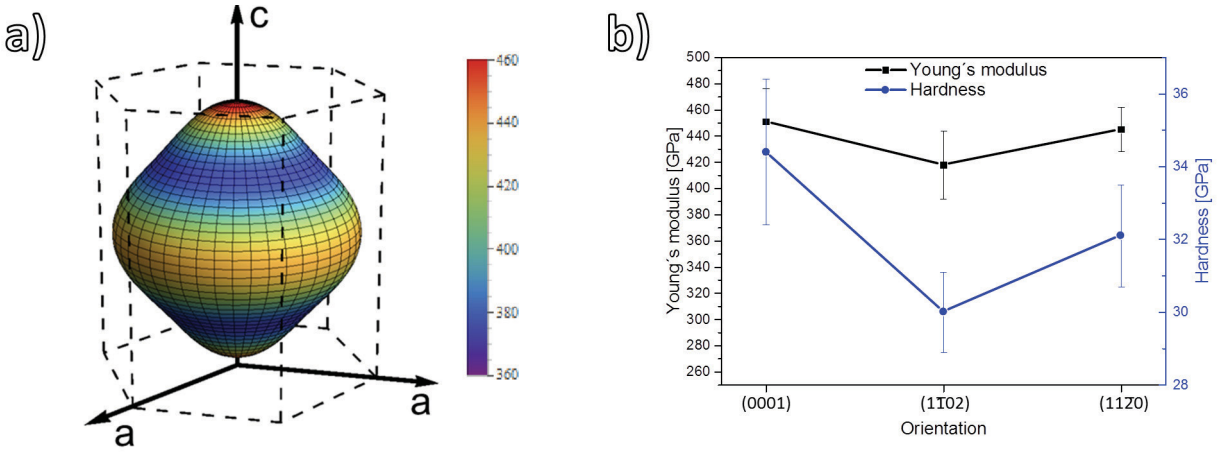

Fig. 13: *(a) Direction dependent Young´s modulus of α-Al_2O_3, perpendicular to the drawn surface, determined from single crystal elastic constants. (b) Hardness and Young´s modulus of epitaxially grown CVD α-Al_2O_3 samples [own work].*

The pronounced anisotropy of the mechanical properties is not only evident in the case of epitaxially grown single crystalline coatings. Ruppi *et al.* recently reported on the anisotropy of polycrystalline textured CVD α-Al_2O_3 coatings [9,82,83]. They reported on the superior mechanical properties of (0001) oriented coatings in nanoindentation experiments and how this knowledge can be used to enhance the coatings performance during cutting [9]. Thus, the control of crystal orientation and texture is an important factor to extend the lifetime of α-Al_2O_3 hard coatings on cutting tools. In application, coatings with a (0001) preferred orientation have proven to perform very well, which is in good agreement with the calculated results and the measurements on the single crystalline as well as polycrystalline coatings, exhibiting the highest values of hardness and elastic modulus for this orientation.

An example of the superior performance of a textured CVD α-Al_2O_3 hard coating is shown in Fig. 14. The electron back-scatter diffraction (EBSD) pole figure measurements depicted in Fig. 14a indicate a pronounced (0001) texture for coating D in contrast to coating E which exhibits a (10$\bar{1}$0) texture. The results of turning tests on steel are shown in Fig. 14b, demonstrating that the flank wear can be reduced by a factor 2 from 0.3 mm for coating E to 0.15 mm for coating D just by the right choice of the coating texture [9].

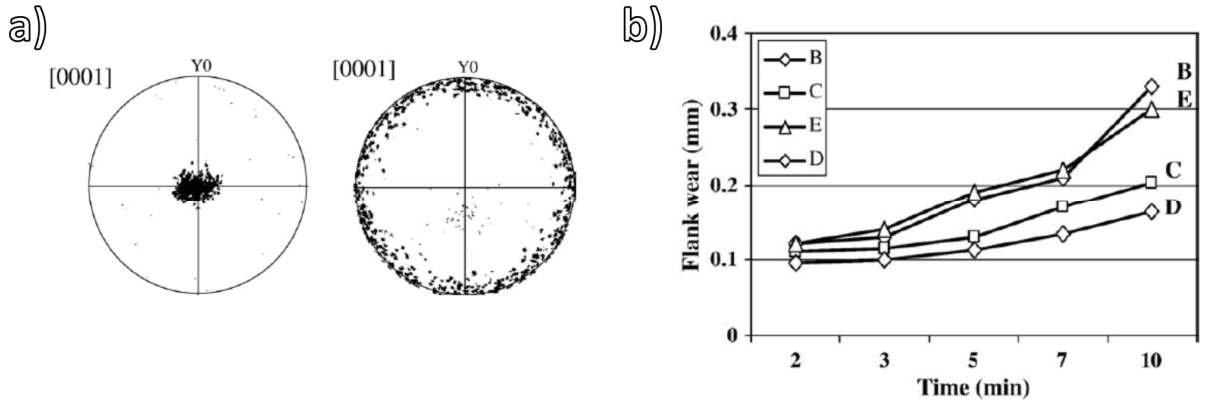

Fig. 14: *(a) EBSD pole figure measurements of a (0001) and a (10$\bar{1}$0) textured CVD α-Al_2O_3 coating. (b) Results of turning tests performed with those coatings, where coating D corresponds to (0001) and E to (10$\bar{1}$0) [9].*

Another example of the influence of the texture is shown in Fig. 15, where XRD pole figure measurements of different reflections are shown for a CVD α-Al_2O_3 coating in the as deposited condition and after dry blasting. While no significant changes due to blasting can be observed for the 0001 and 11$\bar{2}$0 reflections, the 1$\bar{1}$02 reflection changes considerably. As already discussed, this orientation is the weakest one of those three and its tendency to twinning might cause this pronounced effect of the blasting treatment on the XRD pole figure [88]. This example clearly demonstrates that not only the blasting parameters like pressure, working angle and distance or blasting medium play an important role, but also the coating to be blasted and its orientation have major influence on the result of the treatment.

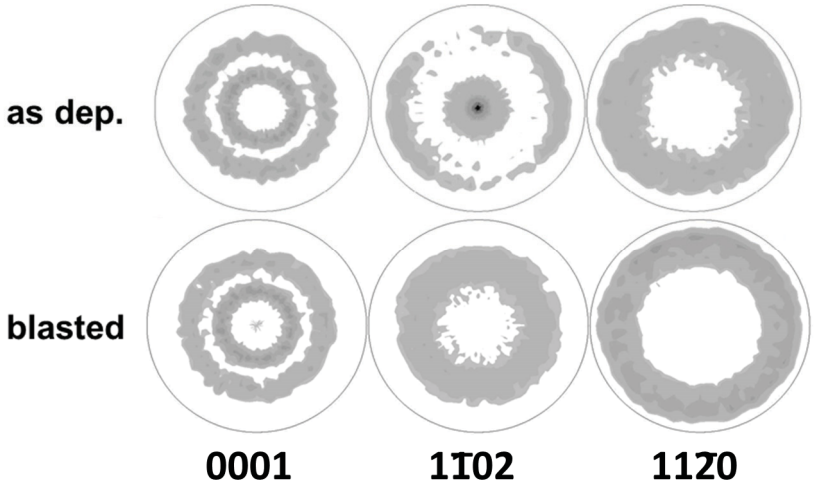

Fig. 15: *XRD pole figure measurements on as deposited and dry-blasted CVD α-Al_2O_3 coatings showing a distinct influence of crystal orientation on the effect of a blasting treatment [own work].*

4. Conclusions

The aim of the present thesis is to improve existing techniques as well as to introduce novel approaches for the characterization of hard and wear resistant coatings. The obtained skills provide the basis for a knowledge based advancement of the investigated coatings. The performed experiments were mainly balanced between two topics: *(i)* cross-sectional characterization methods such as scanning (SEM) and transmission electron microscopy (TEM) utilizing energy dispersive X-ray spectroscopy and electron back-scatter diffraction (EBSD) as well as synchrotron X-ray nanodiffraction in order to reveal the chemical composition and microstructure of the coatings as a function of their thickness and *(ii)* the determination of thermo-physical properties by means of differential scanning calorimetry (DSC) measurements on powdered coatings to reveal their heat capacity, high temperature X-ray diffraction (XRD) and biaxial stress-temperature measurements (BSTM) for the determination of the coefficient of thermal expansion and time-domain thermoreflectance (TDTR) for the determination of the thermal conductivity.

Within a first example to optimize the available characterization methods to the tribological degradation of hard coatings, the influence of droplets on the wear behavior of arc evaporated TiAlTaN coatings in dry sliding contacts has been illuminated. Cross-sectional EDX mapping, extensive SEM imaging and TEM analysis revealed that droplets significantly contribute to coating degradation at room temperature as they deteriorate the mechanical integrity of the coatings and thus, are sources for crack initiation. Further, it was found that the material released due to disintegration of the droplets acts as abrasive wear debris, consequently increasing wear. Testing at elevated temperatures indicated a stabilization effect due to softening of the droplets and simultaneous oxidation within cavities and voids, leading to a self-healing behavior.

To expand synchrotron X-ray nanodiffraction from nanocrystalline materials to coarse grained samples, the conventional synchrotron X-ray nanodiffraction setup was modified from a point focused to a line focused X-ray beam. Using this approach it was possible to investigate microstructure and residual stress of dry-blasted CVD α-Al_2O_3 coatings, with a grain size in the micrometer range, as a function of the coating thickness. The results illuminate the influence of two different blasting media, i.e. with edged and globular shape, on the resulting stress gradients with in the coatings.

A comprehensive survey of advanced characterization techniques for the determination of microstructural, mechanical and thermo-physical properties, as it has been adapted and

optimized within this work for the characterization of hard coatings, is presented in the last part of the thesis. Methods like atom probe tomography, EBSD, synchrotron X-ray nanodiffraction and high temperature nanoindentation provide previously unrevealed insights into microstructure and mechanical properties of wear resistant coatings. Further, high-temperature XRD, BSTM, DSC and TDTR provide access to thermo-physical properties like coefficient of thermal expansion, heat capacity and thermal conductivity. The now available spectrum of advanced characterization techniques provides a key tool-box for the further optimization of hard coatings.

5. References

[1] V. Derflinger, H. Brändle, H. Zimmermann, Surf. Coat. Technol. 113 (1999) 286–292.

[2] W. Kalss, A. Reiter, V. Derflinger, C. Gey, J.L. Endrino, Int. J. Refract. Met. Hard Mater. 24 (2006) 399–404.

[3] F. Klocke, T. Krieg, CIRP Ann. - Manuf. Technol. 48 (1999) 515–525.

[4] S.G. Harris, E.D. Doyle, A.C. Vlasveld, P.J. Dolder, Surf. Coat. Technol. 146-147 (2001) 305–311.

[5] G.S. Fox-Rabinovich, G.C. Weatherly, A.I. Dodonov, A.I. Kovalev, L.S. Shuster, S.C. Veldhuis, G.K. Dosbaeva, D.L. Wainstein, M.S. Migranov, Surf. Coat. Technol. 177-178 (2004) 800–811.

[6] A. Buranawong, N. Witit-Anun, S. Chaiyakun, A. Pokaipisit, P. Limsuwan, Thin Solid Films 519 (2011) 4963–4968.

[7] A. Inspektor, P.A. Salvador, Surf. Coat. Technol. 257 (2014) 138–153.

[8] P.H. Mayrhofer, R. Rachbauer, D. Holec, F. Rovere, J.M. Schneider, in: S. Hashmi (Ed.), Comprehensive Materials Processing, Elsevier, Oxford, 2014.

[9] S. Ruppi, Surf. Coat. Technol. 202 (2008) 4257–4269.

[10] K.-D. Bouzakis, F. Klocke, G. Skordaris, E. Bouzakis, S. Gerardis, G. Katirtzoglou, S. Makrimallakis, Wear 271 (2011) 783–791.

[11] K.-D. Bouzakis, S. Gerardis, G. Skordaris, G. Katirtzoglou, S. Makrimallakis, F. Klocke, E. Bouzakis, Surf. Coat. Technol. 204 (2009) 1081–1086.

[12] K.-D. Bouzakis, E. Bouzakis, G. Skordaris, S. Makrimallakis, A. Tsouknidas, G. Katirtzoglou, S. Gerardis, Surf. Coat. Technol. 205 (2011) 128–132.

[13] R. Daniel, J. Keckes, I. Matko, M. Burghammer, C. Mitterer, Acta Mater. 61 (2013) 6255–6266.

[14] R. Daniel, D. Holec, M. Bartosik, J. Keckes, C. Mitterer, Acta Mater. 59 (2011) 6631–6645.

[15] A. Zeilinger, R. Daniel, T. Schöberl, M. Stefenelli, B. Sartory, J. Keckes, C. Mitterer, Thin Solid Films 581 (2015) 75–79.

[16] M. Rebelo de Figueiredo, M.D. Abad, A.J. Harris, C. Czettl, C. Mitterer, P. Hosemann, Thin Solid Films 578 (2015) 20–24.

[17] D.G. Cahill, S.-M. Lee, T.I. Selinder, J. Appl. Phys. (1998) 5783-5786.

[18] J. Keckes, M. Bartosik, R. Daniel, C. Mitterer, G. Maier, W. Ecker, J. Vila-Comamala, C. David, S. Schoeder, M. Burghammer, Scripta Mater. 67 (2012) 748–751.

[19] M. Tkadletz, J. Keckes, N. Schalk, I. Krajinovic, M. Burghammer, C. Czettl, C. Mitterer, Surf. Coat. Technol. 262 (2015) 134–140.

[20] F. Kone, C. Czarnota, B. Haddag, M. Nouari, Surf. Coat. Technol. 205 (2011) 3559–3566.

[21] R.F. Bunshah, Deposition Technologies for Films and Coatings, Noyes Publications, New Jersey, 1982.

[22] F.-W. Bach, T. Duda, Moderne Beschichtungsverfahren, Wiley-VCH, Weinheim, 2000.

[23] R.A. Haefer, Oberflächen- und Dünnschichttechnologie, Teil I: Beschichtungen von Oberflächen, Springer, Berlin Heidelberg, 1987.

[24] Clear Metals Inc. - Technology: Metal Oxide Deposition, http://clearmetalsinc.com/here/wp-content/uploads/Sputter-illo.png, accessed June 2015.

[25] M. Ohring, The Materials Science of Thin Films – Deposition and Structure, Academic Press, San Diego, 2002.

[26] B. Rother, J. Vetter, Plasmabeschichtungsverfahren und Hartstoffschichten, Deutscher Verlag für Grundstoffindustrie, Leipzig, 1992.

[27] H. Frey, Vakuumbeschichtung 1, Plasmaphysik, Plasmadiagnostik, Analytik, VDI, Düsseldorf, 1995.

[28] W.D. Westwood, Sputter Deposition, AVS, New York, 2003.

[29] R.L. Boxman, D.M. Sanders, P.J. Martin, Handbook of Vacuum Arc Science and Technology: Fundamentals and Applications, Noyes Publications, New Jersey, 1995.

[30] W. Kern, J.L. Vossen, Thin Film Processes II, Academic Press, San Diego, 2012.

[31] D.M. Sanders, A. Anders, Surf. Coat. Technol. 133-134 (2000) 78–90.

[32] H.K. Pulker, Vak. Forsch. und Prax. 11 (1999) 25–25.

[33] A. Hörling, L. Hultman, M. Odén, J. Sjölén, L. Karlsson, J. Vac. Sci. Technol. A 20 (2002) 1815.

[34] U. Helmersson, M. Lattemann, J. Bohlmark, A.P. Ehiasarian, J.T. Gudmundsson, Thin Solid Films 513 (2006) 1–24.

[35] R.L. Boxman, S. Goldsmith, Surf. Coat. Technol. 52 (1992) 39–50.

[36] HCVAC - Dongguan Huicheng Vacuum Technology Co., Ltd.: Arc Evaporation, http://www.hcvacuum.com/node/66, accessed June 2015.

[37] D.M. Mattox, Handbook of Physical Vapor Deposition (PVD) Processing, William Andrew, Oxford, 2010.

[38] P.H. Mayrhofer, C. Mitterer, L. Hultman, H. Clemens, Prog. Mater. Sci. 51 (2006) 1032–1114.

[39] H.A. Jehn, B. Rother, Int. J. Refract. Met. Hard Mater. 14 (1996) 87–95.

[40] J. Kohlscheen, H.R. Stock, P. Mayr, Surf. Coat. Technol. 120-121 (1999) 740–745.

[41] N. Schalk, Synthesis and Post-treatment of Hard Coatings for Cemented Carbide Cutting Tools, PhD Thesis, Montanuniversität Leoben, 2013.

[42] C. Czettl, Design of CVD Coatings for Cutting Tools, PhD Thesis, Montanuniversität Leoben, 2013.

[43] K.L. Choy, Prog. Mater. Sci. 48 (2003) 57–170.

[44] H.O. Pierson, Handbook of Chemical Vapor Deposition (CVD), William Andrew, New York, 1999.

[45] H. Lüth, Solid Surfaces, Interfaces and Thin Films, Springer, Berlin, Heidelberg, 2010.

[46] B.A. Movchan, A. V Demchishin, Phys. Met. Met. 28 (1969) 653–660.

[47] J.A. Thornton, J. Vac. Sci. Technol. 11 (1974) 666–670.

[48] R. Messier, J. Vac. Sci. Technol. A 2 (1984) 500–503.

[49] A. Anders, Thin Solid Films 518 (2010) 4087–4090.

[50] A. Riedl, N. Schalk, C. Czettl, B. Sartory, C. Mitterer, Wear 289 (2012) 9–16.

[51] N. Schalk, C. Mitterer, C. Czettl, B. Sartory, M. Penoy, C. Michotte, Tribol. Lett. 52 (2013) 147–154.

[52] M. Klaus, C. Genzel, H. Holzschuh, Thin Solid Films 517 (2008) 1172–1176.

[53] K.-D. Bouzakis, G. Skordaris, I. Mirisidis, N. Michailidis, G. Mesomeris, E. Pavlidou, G. Erkens, Surf. Coat. Technol. 200 (2005) 1879–1884.

[54] K.-D. Bouzakis, G. Skordaris, F. Klocke, E. Bouzakis, Surf. Coat. Technol. 203 (2009) 2946–2953.

[55] C. Barbatti, J. Garcia, R. Pitonak, H. Pinto, A. Kostka, A. Di Prinzio, M.H. Staia, A.R. Pyzalla, Surf. Coat. Technol. 203 (2009) 3708–3717.

[56] P.H. Mayrhofer, C. Mitterer, L. Hultman, H. Clemens, Prog. Mater. Sci. 51 (2006) 1032–1114.

[57] M. Stefenelli, J. Todt, A. Riedl, W. Ecker, T. Müller, R. Daniel, M. Burghammer, J. Keckes, J. Appl. Cryst. 46 (2013) 1378–1385.

[58] M. Bartosik, R. Pitonak, J. Keckes, Adv. Eng. Mater. 13 (2011) 705–711.

[59] K. Schiffner, C. Droste gen. Helling, Comput. Struct. 72 (1999) 329–340.

[60] P.H. Mayrhofer, A. Hörling, L. Karlsson, J. Sjölén, T. Larsson, C. Mitterer, L. Hultman, Appl. Phys. Lett. 83 (2003) 2049–2051.

[61] P.H. Mayrhofer, F. Kunc, J. Musil, C. Mitterer, Thin Solid Films 415 (2002) 151–159.

[62] N. Schalk, C. Mitterer, I. Letofsky-Papst, C. Czettl, B. Sartory, M. Penoy, C. Michotte, Tribol. Int. 67 (2013) 54–60.

[63] S. PalDey, S.C. Deevi, Mater. Sci. Eng. A 361 (2003) 1–8.

[64] M. Durandurdu, J. Phys. Chem. Solids 69 (2008) 2894–2897.

[65] M. Kawate, A. Kimura, T. Suzuki, J. Vac. Sci. Technol. A 20 (2002) 569–571.

[66] I.W. Park, D.S. Kang, J.J. Moore, S.C. Kwon, J.J. Rha, K.H. Kim, Surf. Coat. Technol. 201 (2007) 5223–5227.

[67] E. Spain, J.C. Avelar-Batista, M. Letch, J. Housden, B. Lerga, Surf. Coat. Technol. 200 (2005) 1507–1513.

[68] W.D. Cho, H.Y. Sohn, M. Minerals, M.S. Meeting, Value-Addition Metallurgy, TMS, San Antonio, 1998.

[69] A. Kimura, H. Hasegawa, K. Yamada, T. Suzuki, Surf. Coat. Technol. 120-121 (1999) 438–441.

[70] A. Hörling, L. Hultman, M. Odén, J. Sjölén, L. Karlsson, Surf. Coat. Technol. 191 (2005) 384–392.

[71] M. Pfeiler, C. Scheu, H. Hutter, J. Schnöller, C. Michotte, C. Mitterer, M. Kathrein, J. Vac. Sci. Technol. A 27 (2009) 554–560.

[72] M. Pfeiler, G.A. Fontalvo, J. Wagner, K. Kutschej, M. Penoy, C. Michotte, C. Mitterer, M. Kathrein, Tribol. Lett. 30 (2008) 91–97.

[73] P.H. Mayrhofer, C. Mitterer, J. Musil, Surf. Coat. Technol. 174-175 (2003) 725–731.

[74] R. Daniel, A. Zeilinger, T. Schöberl, B. Sartory, C. Mitterer, J. Keckes, J. Appl. Phys. 117 (2015) 235301.

[75] S. Ruppi, J. Phys. IV 11 (2001) 847–859.

[76] A. Osada, E. Nakamura, H. Homma, T. Hayahi, T. Oshika, Int. J. Refract. Met. Hard Mater. 24 (2006) 387–391.

[77] D. Hochauer, C. Mitterer, M. Penoy, C. Michotte, H.P. Martinz, M. Kathrein, Surf. Coat. Technol. 204 (2010) 3713–3722.

[78] D. Hochauer, C. Mitterer, M. Penoy, C. Michotte, H.P. Martinz, M. Kathrein, Surf. Coat. Technol. 203 (2008) 350–356.

[79] I. Levin, D. Brandon, J. Am. Ceram. Soc. 81 (1998) 1995–2012.

[80] S. Vuorinen, L. Karlsson, Thin Solid Films 214 (1992) 132–143.

[81] S. Ruppi, A. Larsson, Thin Solid Films 388 (2001) 50–61.

[82] S. Ruppi, A. Larsson, A. Flink, Thin Solid Films 516 (2008) 5959–5966.

[83] S. Ruppi, Int. J. Refract. Met. Hard Mater. 23 (2005) 306–316.

[84] J. Skogsmo, M. Halvarsson, S. Vuorinen, Surf. Coat. Technol. 54-55 (1992) 186–192.

[85] M. Kathrein, W. Schintlmeister, W. Wallgram, U. Schleinkofer, Surf. Coat. Technol. 163-164 (2003) 181–188.

[86] A.A. Layyous, D.M. Freinkel, R. Israel, Surf. Coat. Technol. 56 (1992) 89–95.

[87] M. Halvarsson, H. Nordén, S. Vuorinen, Surf. Coat. Technol. 61 (1993) 177–181.

[88] V. Pishchik, L.A. Lytvynov, E.R. Dobrovinskaya, Sapphire: Material, Manufacturing, Applications, Springer, New York, 2009.

[89] J.F. Nye, Physical Properties of Crystals: Their Representation by Tensors and Matrices, Clarendon Press, Oxford, 1985.

6. Publications

6.1. List of included publications

I. The effect of droplets in arc evaporated TiAlTaN hard coatings on the wear behavior

M. Tkadletz, C. Mitterer, B. Sartory, I. Letofsky-Papst, C. Michotte

Surface and Coatings Technology 257 (2014) 95-101.

II. Residual stress gradients in α-Al_2O_3 hard coatings determined by pencil-beam X-ray nanodiffraction: The influence of blasting media

Michael Tkadletz, Jozef Keckes, Nina Schalk, Ivan Krajinovic, Manfred Burghammer, Christoph Czettl, Christian Mitterer

Surface and Coatings Technology 262 (2015) 134-140.

III. Advanced characterization methods for wear resistant hard coatings: A review on recent progress

Michael Tkadletz, Nina Schalk, Rostislav Daniel, Jozef Keckes, Christoph Czettl, Christian Mitterer

Invited review submitted to Surface and Coatings Technology.

6.2. Publications related to this work

IV. Restrictions of stress measurements using the curvature method by thermally induced plastic deformation of silicon substrates

Christian Saringer, Michael Tkadletz, Christian Mitterer

Surface and Coatings Technology 274 (2015) 68-75.

6.3. My contribution to the included publications

Publication I

For the first publication, the coating samples were provided by the project partner Ceratizit Austria GmbH. I performed the ball on disk tests, nanoindentation measurements and X-ray diffraction measurements. Further, I evaluated the scanning electron microscopy investigations, which were performed with the help of Bernhard Sartory. The interpretation of the transmission electron microscopy investigations, which were performed with Ilse Letofsky-Papst, was also done by myself. The interpretation of the obtained results as well as the development of the publication concept and writing of this manuscript was done by my own.

Publication II

Also for this publication, the coating samples were provided by Ceratizit Austria GmbH. I performed the X-ray diffraction measurements as well as the synchrotron measurements at the ID13 beamline located at the ESRF in Grenoble, France. The evaluation of the synchrotron data was supported by Prof. Jozef Keckes. SEM investigations as well as the EBSD measurements were performed together with Bernhard Sartory. The FEM simulations were provided by Ivan Krajinovic. The development of the manuscript concept, planning and writing was done by myself.

Publication III

Within this publication, a comprehensive overview on characterization techniques for hard coatings is provided. The conception and planning was done together with Prof. Christian Mitterer and Dr. Nina Schalk. I performed the extensive literature research and collection of results of the different techniques. Parts of the previous two publications are included within this publication representing the success of the development and improvement of characterization techniques within this thesis. Further, I deposited the PVD coatings for the chapter discussing the thermo-physical properties myself. The HT-XRD measurements were performed by Dr. Manfred Wießner (Materials Center Leoben) and I evaluated the data and calculated the coefficients of thermal expansion. The annealing treatments for the thermal conductivity series were performed by myself and the time-domain thermoreflectance measurements were performed by Dr. Markus Winkler (Fraunhofer Institute for Physical Measurement Techniques IPM, Freiburg, Germany). For the measurements of the specific heat capacity by DSC, I prepared the powders after deposition and carried out and evaluated the experiments. Finally, I also wrote the manuscript.

	Conception and planning	Experiments	Analysis and interpretation	Manuscript preparation
Publication I	**100**	**80**	**100**	**100**
Publication II	**100**	**100**	**90**	**100**
Publication III	**100**	**30**	**100**	**90**

Supervision not included.

Publication I

The effect of droplets in arc evaporated TiAlTaN hard coatings on the wear behavior

M. Tkadletz, C. Mitterer, B. Sartory, I. Letofsky-Papst, C. Czettl, C. Michotte

Surface and Coatings Technology 257 (2014) 95-101

The effect of droplets in arc evaporated TiAlTaN hard coatings on the wear behavior

M. Tkadletz[1], C. Mitterer[2], B. Sartory[1], I. Letofsky-Papst[3], C. Czettl[4], C. Michotte[5]

[1] *Materials Center Leoben Forschung GmbH, Roseggerstraße 12, A-8700 Leoben, Austria*

[2] *Department of Physical Metallurgy and Materials Testing, Montanuniversität, Franz-Josef-Straße 18, A-8700 Leoben, Austria*

[3] *Institute for Electron Microscopy and Nanoanalysis, Graz University of Technology, Steyrergasse 17, A-8010 Graz, Austria*

[4] *CERATIZIT Austria GmbH, Metallwerk-Plansee-Straße 71, A-6600 Reutte, Austria*

[5] *CERATIZIT Luxembourg Sàrl, Route de Holzem, B.P.51, L-8201 Mamer, Luxembourg*

Abstract

Hard coatings deposited by cathodic arc evaporation are often characterized by droplets, deteriorating their surface roughness and oxidation resistance. Within this work, the response of these droplets to tribological loading and their contribution to the tribological system was investigated. Ball-on-disk tests against Al_2O_3 counterparts were done on TiAlTaN coated cemented carbide disks at room temperature and 700 °C. Surfaces as well as cross-sections through the wear tracks were investigated by scanning and transmission electron microscopy. While droplets were found to contribute to coating degradation by providing nucleation sites for shear cracks and by the release of abrasive fragments into the sliding contact, oxidation at elevated temperature leads to a more efficient embedding into the surrounding coating matrix. This suggests an oxidation induced self-healing process, contributing to the enhanced wear resistance of TiAlN-based hard coatings at elevated temperatures.

Keywords:

Hard coatings, TiAlTaN, arc evaporation, droplets, macroparticles, tribological properties

1. Introduction

The wear behavior of hard coatings plays an important role for coated cutting tools as wear directly affects the tool lifetime. For cutting inserts, the wear resistance is often evaluated by milling or turning tests, which provide information about tool lifetime and performance of different coatings. These field tests include a large number of variables like cutting speed, cutting force and cutting temperature, which are often not known to a sufficient extent. Hence, it is difficult to relate a certain observed cutting or wear behavior to specific properties of particular coating systems [1-5]. Another possibility is to perform tests, which are reduced to a small number of controlled variables, like ball-on-disk tests [6]. Those give detailed reproducible information about the tribological properties of different coating systems. Selected variations of their properties, for example due to changes in the deposition process [7, 8], can be compared to each other. Wear-resistant hard coatings are often deposited by cathodic arc evaporation, with its inherent benefits of increased deposition and high ionization rates compared to sputtering. However, cathodic arc evaporated coatings are often characterized by droplets, which negatively affect the surface roughness, the corrosion and oxidation stability (as they act as diffusion paths), and subsequently the tribological properties [9-11]. Up to now, a comprehensive understanding of their effect on the wear behavior of the coating – both in cutting as well as in tribological tests – is essentially missing.

Previous reports have shown that the addition of small amounts of Ta to the TiAlN system do not change the crystal structure of the coating significantly but its mechanical properties, the decomposition temperature and oxidation resistance are significantly increased [12]. Modern cutting operations are known to result in very high temperatures on the tools cutting edge [13]. Hence, within this work ball-on-disk tests were performed at room temperature (RT) and 700 °C on cemented carbide disks coated by cathodic arc evaporation with a state-of-the-art commercial TiAlTaN coating to gain knowledge about the high temperature behavior of the used coating system. The surface as well as cross-sections of the wear tracks prepared by focused ion beam (FIB) techniques were investigated using scanning and transmission electron microscopy (SEM, TEM). Special emphasis was laid on the role of droplets in the performed ball-on-disk tests, where possible mechanisms triggering coating degradation have been determined.

2. Experimental Details

The coating investigated within this work was deposited on polished cemented carbide disks (∅ 30 × 4 mm) consisting of 77 wt% tungsten carbide, 12 wt% mixed carbides and 11 wt% cobalt. An industrial-scale cathodic arc evaporation system of type Oerlikon Balzers RCS using a deposition process according to Pfeiler *et al.* [14] was used. The coating consists of a ~0.4 μm thick adhesion layer of TiN and a ~2.8 μm thick TiAlTaN toplayer with a composition of $Ti_{0.38}Al_{0.58}Ta_{0.04}N$ [14].

Ball-on-disk tests were performed at RT and 700 °C with a CSM high temperature tribometer applying a load of 5 N for a sliding distance of 300 m, a wear track radius of 7 mm and Al_2O_3 balls (Ø 6 mm) as counterparts. The tests were performed at ambient atmosphere with a relative humidity of 25%. Wear track profiles were determined using a Nanofocus μsurf white-light confocal interferometer. X-ray diffraction (XRD) measurements were performed utilizing a Bruker Advance D8 diffractometer in grazing incidence mode with an inclining angle of 2° from 20 to 85° with a step size of 0.02° and a measuring time of 1.2 s using copper K_α radiation. For determination of the coating hardness, a UMIS nano-indenter from Fischer-Cripps Laboratories was used. Due to the rather high roughness of the arc evaporated coatings, a small area of the surface was carefully polished and plateau tests applying a force decreasing from 25 to 5 mN in steps of 1 mN leading to an indentation depth of 75 to 200 nm were performed. To achieve reasonable statistics, at least 16 indents on each sample were used to determine the mechanical properties. Surface examinations as well as the cross-section investigations were performed with a Zeiss Auriga Crossbeam field emission gun SEM. Cross-sections as well as TEM lamellas were prepared with an Orsay Physics Cobra Z-05 FIB extension. Energy-dispersive X-ray spectroscopy (EDS) measurements were performed with an EDAX Apollo 40+ detector. All TEM imaging, TEM EDS and energy filtering TEM (EFTEM) elemental distribution investigations were performed with a FEI Tecnai F20 TEM equipped with a field emission gun combined with a quantum energy filter. The selected area electron diffraction (SAED) measurements were conducted with a FEI T12 TEM equipped with a LaB_6 cathode and an acceleration voltage of 120 kV.

3. Results

The performed ball-on-disk tests reveal that the coefficient of friction is decreasing with increasing temperature from 0.8 to 0.5 (see Figs. 1a and c). Figs. 1b and d indicate that also the maximum wear track depth is decreasing from 1.5 to 0.75 µm. This corresponds to a decrease of the wear coefficient of almost one order of magnitude from 1.36×10^{-14} to 2.27×10^{-15} m^3/Nm. Decreasing friction and wear coefficients with increasing testing temperature for TiAlN-based coatings were previously also reported by Kutschej *et al.* [15] and Pfeiler *et al.* [7], respectively. Similar behavior was reported for other coating systems like AlSiTiN [16, 17] while these effects do not appear when CrAlN or CrAlSiN is tested [18]. However, within this work special attention is paid to the response of droplets to mechanical loading and their contribution to the tribological system.

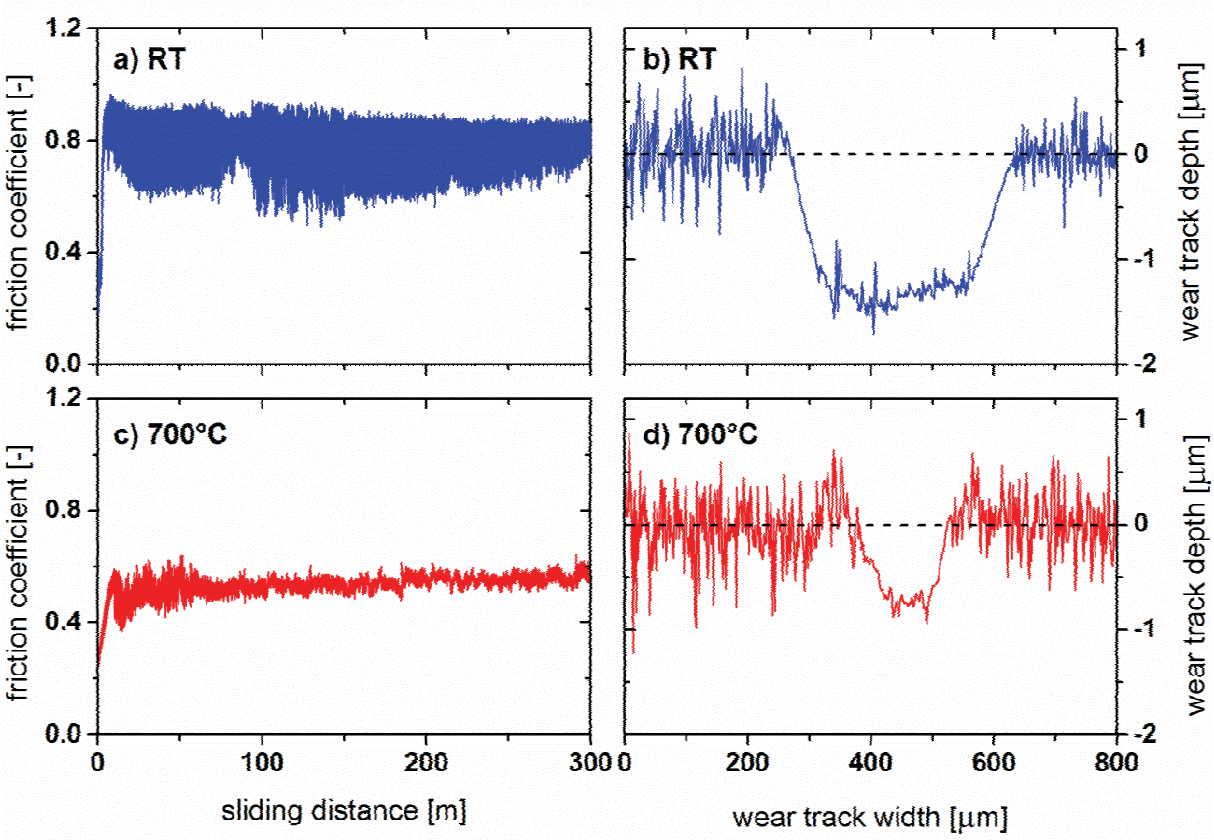

Fig. 1: *Coefficient of friction as a function of the sliding distance and 2D profile of the wear track obtained for tribological testing at RT (a, b) and 700 °C (c, d).*

To shed light on the wear behavior and thus to determine possible mechanisms triggering coating degradation, surface and cross-sectional SEM investigations on the wear tracks of the tested samples were performed. After RT testing, comet tail like features originating from droplets were found inside the wear tracks. A representative comet tail is marked by

the white arrow in Fig. 2a, while a detailed surface view of a droplet within the wear track on a sample tested at 700 °C is shown in Fig. 2b. In front (with respect to the sliding direction) of the droplet in Fig. 2b, cracks are visible (indicated by white arrows). Those cracks are related to tensile stresses caused by the friction force acting during the ball-on-disk test. This corroborates the assumption that droplets significantly contribute to the degradation of the coating material in sliding contacts.

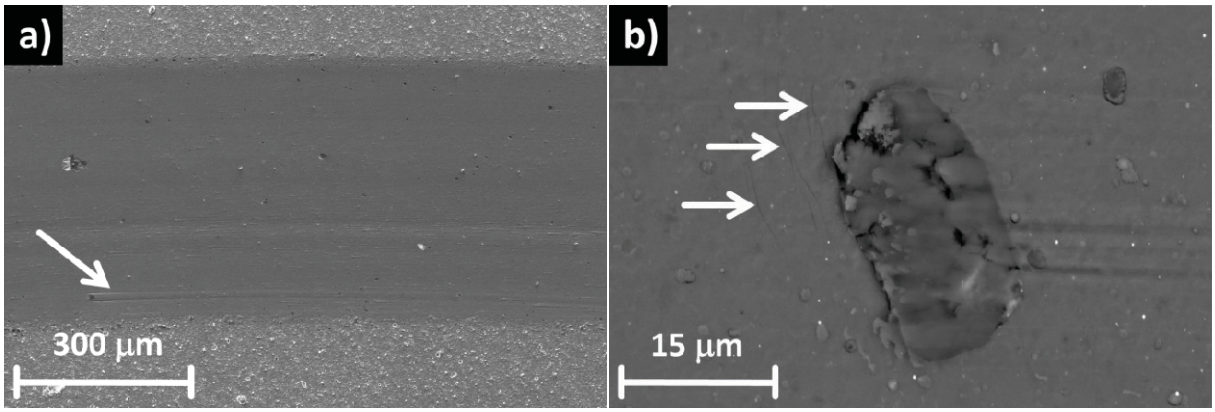

Fig. 2: *Top view of a RT wear track, sliding direction from left to right (a). A comet tail, originating from a droplet, can be seen and is indicated by the white arrow. A higher magnification of a droplet (b) exhibits surface (tensile) cracks which are marked by the white arrows.*

To illuminate this damage behavior further, the nature of the droplets without tribological loading has been characterized. The top view of a pristine coating surface, i.e. outside the wear track of a sample tested at RT, including a representative droplet is shown in Fig. 3a. Figure 3b shows a cross-sectional view of the same droplet with a superimposed EDS mapping. From both, the top- as well as the cross-sectional view, a droplet diameter of ~6 µm can be obtained. The EDS mapping in Fig. 3b reveals that the core region of the droplet mainly consists of titanium. Within this metallic core, brighter and darker areas are visible, corresponding to local differences in chemical composition. On top of the core, coating material can be seen which has overgrown the droplet during the ongoing deposition process. On the very top, a platinum layer is visible, which was deposited to obtain a smooth FIB cut. Droplets with essentially metallic character and a chemical composition corresponding to the used target material were previously reported by several authors [19-22]. Their shape and size has been reported to be determined whether they arrive at the substrate in a molten or semi-molten condition [19-21].

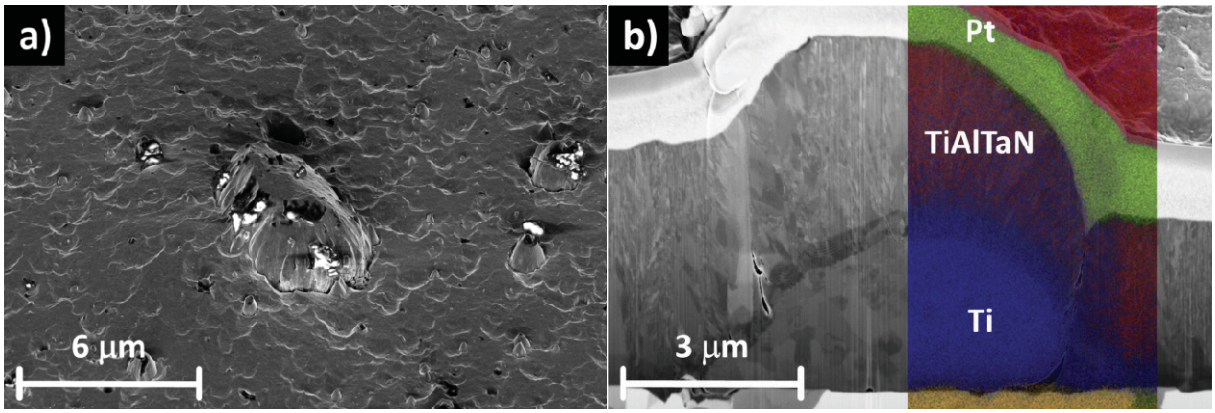

Fig. 3: *Top view of a typical droplet in the as deposited state outside the wear track (a). The cross-section of the same droplet including an EDS mapping is shown in (b) indicating the metallic Ti core, the coating material and a Pt layer which is promoting a smoother FIB cut.*

Within the wear track, droplets with similar structure, shape and size were found. Depending on the geometry and appearance of the droplets, three different possibilities of their effect on coating wear could be distinguished. In the first case, (*i*), the droplet is stable and no evidence of droplet-initiated coating degradation can be found. The second case, (*ii*), is illustrated in Figs. 4a and b. The top view SEM image (Fig. 4a) reveals no evidence of obvious coating damage with the exception of material accumulation in front of the droplet with respect to the sliding direction. In contrast, in the cross-sectional view of the same droplet (Fig. 4b) cracks can be seen behind the droplet (again with respect to the sliding direction). A closer view of the crack is provided by Fig. 4c, where the direction of the crack suggests that it propagates due to shear stresses. The third case of coating degradation, (*iii*), illustrated in Fig. 4d, is related to droplets, which are mechanically not stable and collapse due to the load applied by the ball-on-disk test. In this case, fragments of the collapsed droplet are released into the wear track forming wear debris. This increased amount of wear debris inside the wear track, acting as abrasive medium, is expected to significantly increase coating wear. The droplets collapsing within the coating matrix generate cavities, which are subsequently filled with accumulated and compacted wear debris (see the featureless area above the remaining part of the droplet in Fig. 4d). The same material accumulation can be found within surface cavities for all three cases or if obstacles are present which hinder the flow of wear debris within the sliding contact.

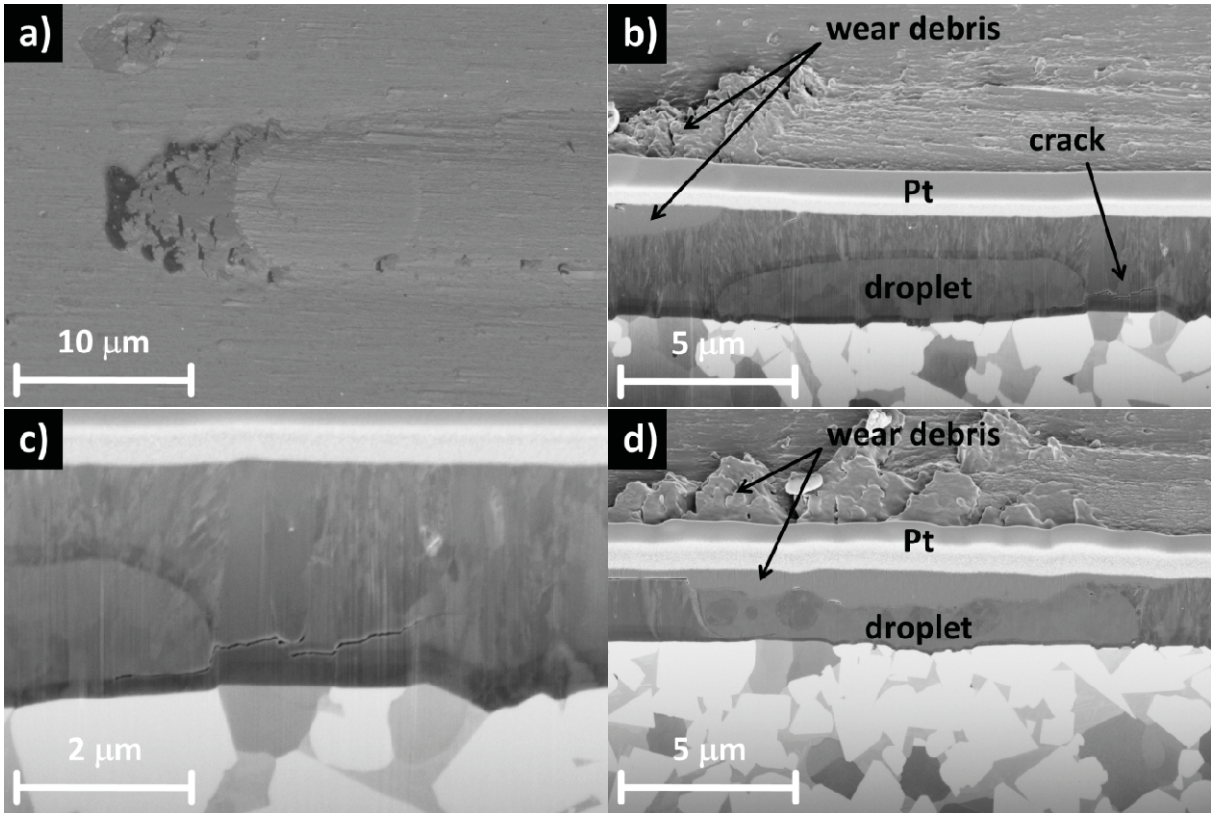

Fig. 4: *Top view of a RT sample droplet inside the wear track (sliding direction from left to right) including material accumulation in front of the droplet (a). The cross-section of the same droplet (b) shows the accumulation in the front and a crack at the end of the droplet. A closer view of the subsurface (shear) crack is shown in (c) and a collapsed droplet filled with accumulated material is shown in (d).*

To characterize the material accumulations (see Fig. 4d) and the areas with differing brightness within the droplet core (see Fig. 3b), TEM lamellas through the wear track of a coating sample with a droplet tested at RT and at 700 °C, respectively, were prepared. Figure 5a shows a bright-field (BF) TEM micrograph of a droplet within the wear track of the RT sample. Figure 5b to d present the corresponding EFTEM elemental distributions for titanium, nitrogen and oxygen. The BF micrograph in Fig. 5a shows, beneath the top platinum layer, the coating which has overgrown the droplet core. This area is characterized by compositional variations originating from substrate rotation during the deposition process [23], which is best seen in the titanium and nitrogen mappings in Figs. 5b and c. Also the TiN adhesion layer close to the cemented carbide substrate is clearly seen. The titanium and nitrogen mappings in Figs. 5b and c confirm that the droplet core mainly consists of titanium. The nitrogen distribution (Fig. 5c) indicates that the areas with differing brightness within the droplet core correspond to areas with more or less nitrogen. They are assumed to origin from the different nitriding behavior of liquid or semi-liquid droplets in the reactive gas atmosphere during their transport from the target to the substrate. Partially nitrided

metallic macro-particles, in particular titanium droplets, in arc evaporated TiN coatings have also been reported by Ljungcrantz *et al.* [22]. The oxygen distribution in Fig. 5d clearly shows that the cavity on top of the droplet, which is filled with accumulated wear debris, is characterized by an increased oxygen concentration with respect to the genuine coating material. Higher oxygen levels are also found in the underdense areas surrounding the droplet.

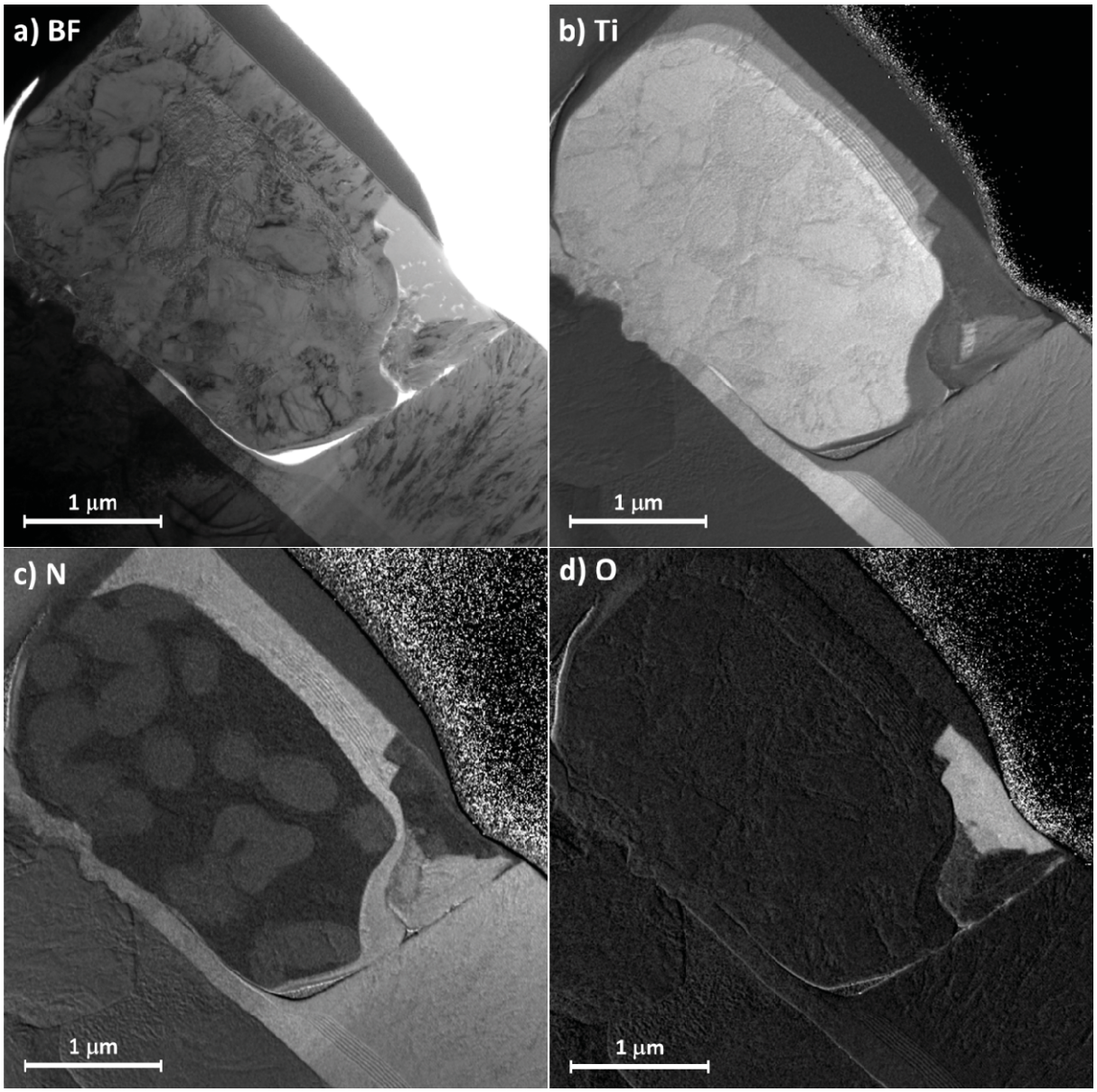

Fig. 5: *TEM bright field micrograph of a RT sample droplet inside the wear track (a) and EFTEM elemental distributions of Ti (b), N (c) and O (d). The Ti distribution (b) of the droplet reveals a metallic core including nitrided areas which can be seen in the N distribution (c). The O distribution (d) shows a highly oxygen enriched material accumulation on top of the droplet.*

To characterize the structure of the droplets in more detail and to illuminate the wear debris accumulated within the cavity, SAED investigations were carried out. A BF TEM micrograph of a droplet in the RT sample is shown in Fig. 6a. There, the white circle marks the area where the SAED pattern shown in Fig. 6b was recorded. The discrete diffraction spots reveal the metallic droplet core to essentially consist of the α-Ti phase. The material accumulated within the cavity appears almost featureless in the BF TEM micrograph in Fig. 6c, where again the area for taking the SAED pattern is indicated by a white circle. The SAED pattern in Fig. 6d exhibits a diffuse diffraction ring, which can be related to an amorphous or nanocrystalline structure. TEM EDS measurements on the same area indicate this area to consist of oxidized coating material. Summarizing the findings obtained by SAED and the EDS, the accumulated material found on the RT coating sample could be identified as worn coating material, presumably formed by accumulation and compaction of wear debris in coating surface cavities. Besides oxygen, no evidence of remaining nitrogen was found, which reveals that this material is completely oxidized as a result of the occurring local flash temperatures [24] and the ambient environment.

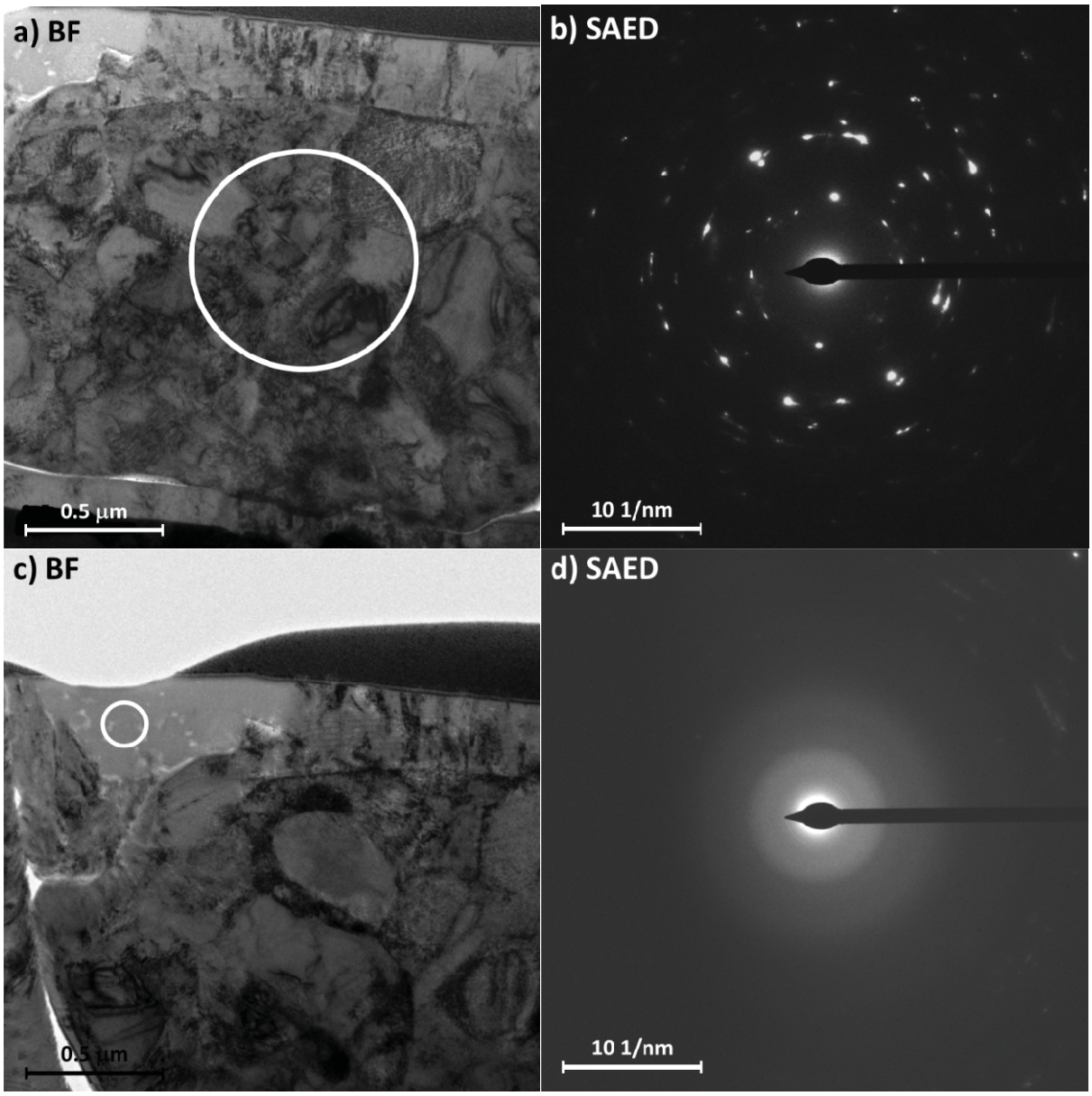

Fig. 6: *BF TEM micrograph of a RT sample droplet (a) and the corresponding SAED pattern (b) of the area marked by the white circle, which reveals a crystalline structure identified as α-Ti. The BF TEM picture (c) shows material accumulation. The corresponding SAED measurement (d), which reveals an amorphous or nano-crystalline structure, was conducted within that accumulation and is marked by a white circle.*

A SEM micrograph of a cross-section through the wear track of the coating sample tested at 700 °C is shown in Fig. 7. The structure of the droplet is similar to the RT sample, where the core essentially consists of titanium and the cavity above the droplet is filled with worn coating material. In contrast to the RT sample, the originally underdense area between the droplet and the genuine coating material appears gray, indicating dense agglomerates (see the white arrows in Fig. 7). Also cracks are hardly visibly in the cross-sections through the 700 °C sample.

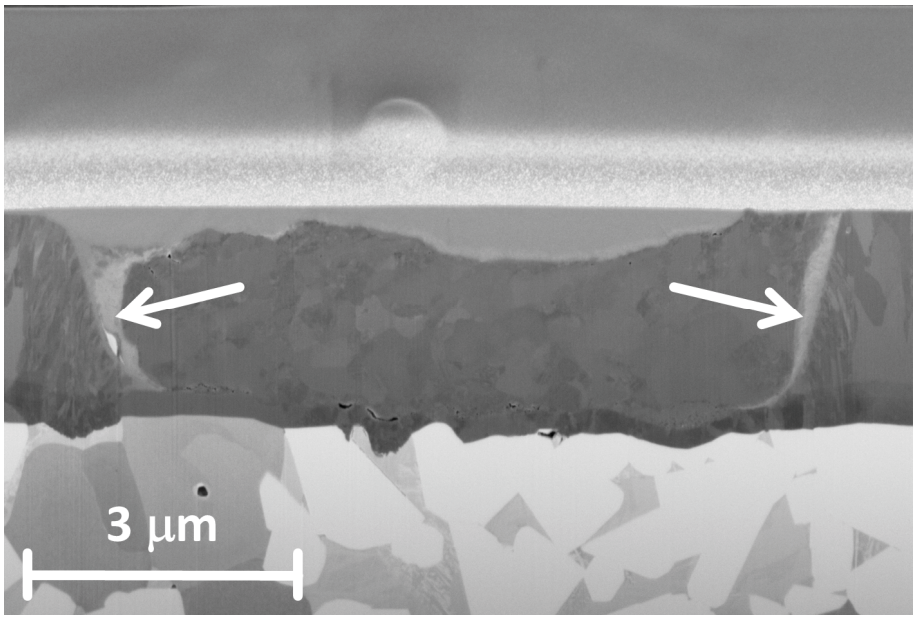

Fig. 7: *SEM Cross-section of a 700 °C sample droplet inside the wear track. The droplet partially collapsed and exhibits material accumulation on top. Oxidized zones are indicated by the white arrows.*

To shed light on the formerly underdense areas surrounding the droplets, again a TEM lamella through a droplet in the wear track of a coating sample tested at 700 °C was prepared. The BF TEM micrograph in Fig. 8a shows the droplet and the area surrounding the droplet, while Fig. 8b exhibits the EFTEM oxygen distribution map of the same area. The agglomerates formerly seen in the SEM and the TEM BF micrograph (see Figs. 7 and 8a) are characterized by a significantly increased oxygen level. In addition, also the cracks within the wear track through the coating show high oxygen concentrations (see Fig. 8c), while they are hardly visible in the SEM and TEM BF micrographs. Taking into account the high level of oxygen indicated by EDS and the dense appearance in the SEM and BF TEM micrographs, these areas are assumed to consist of oxidized material.

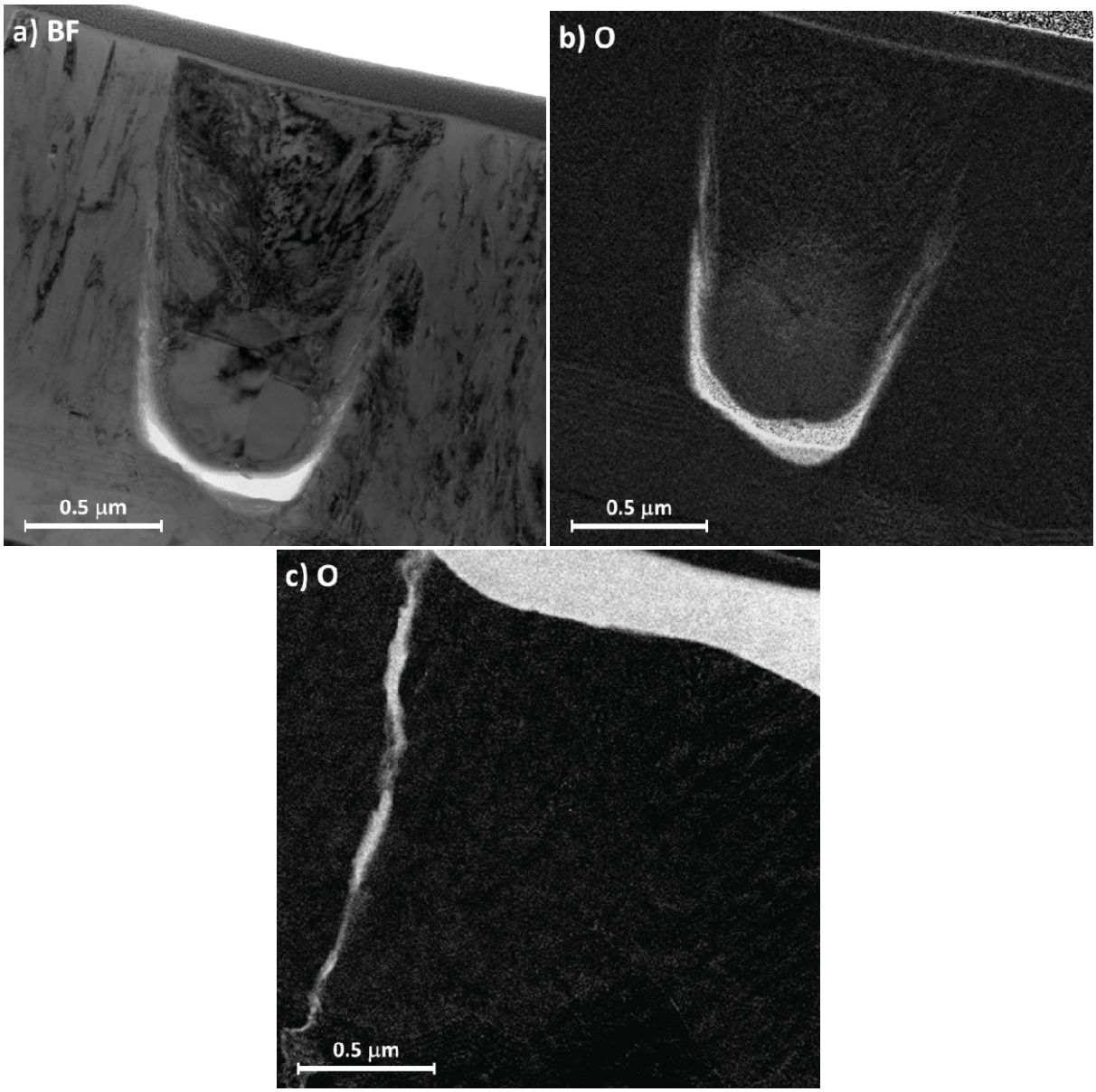

Fig. 8: *BF TEM micrograph of a 700 °C sample droplet inside the wear track (a). The oxygen distribution of the droplet (b) reveals oxidation in the region of cavities. An oxygen distribution of another area including a crack (c) exhibits oxidation inside the crack as well.*

Figure 9a shows a TEM BF detail of the material accumulated on top of the droplet, where the white circle indicates the area for the SAED pattern in Fig. 9b. The discrete diffraction rings indicate crystalline phases, either caused by crystal growth or recrystallization due to exposure to elevated temperature, while the diffuse ring indicates remaining amorphous phase fractions. The analysis of the diffraction rings reveals the presence of crystalline Ti_3AlO. The existence of this phase has been reported previously [25-27]. The SAED patterns obtained for the droplet itself did only reveal minor microstructural changes, where in the nitrogen enriched areas within the droplet cores the $Ti_4N_{2.33}$ phase was found. Such an interstitial Ti-N phase exists in a wide range of compositions [28]; due to the high Ti

concentration available within the droplet, formation of this Ti-enriched nitride is reasonable.

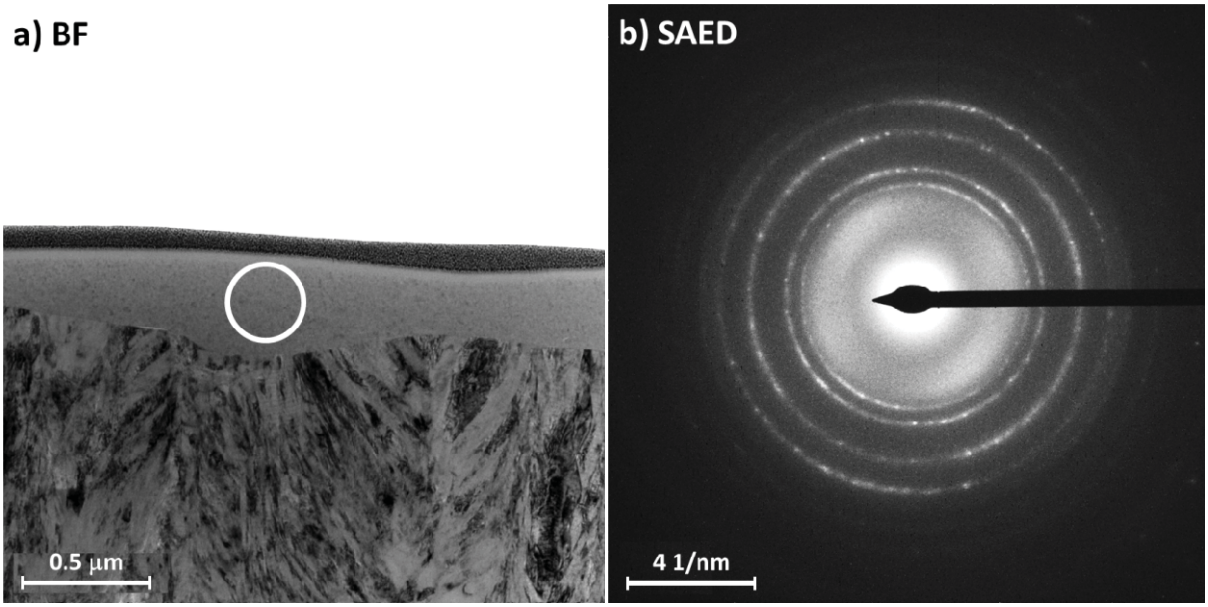

Fig. 9: *BF TEM micrograph of a 700 °C sample droplet inside the wear track (a) showing material accumulation and indicating the area (white circle) where the SAED measurement (b) has been performed.*

4. Discussion

Droplets in arc evaporated TiAlTaN hard coatings were found to contribute to coating degradation in tribological sliding contacts via two different mechanisms, i.e. by introducing cracks into the coating and/or by collapsing of the droplet itself, where material is released into the wear track as wear debris. Most pronounced at RT, the latter increases on the one hand coating wear immediately, as droplet material is removed from the coating. On the other hand, the formed wear debris acts as abrasive medium, which consequently also increases wear. However, at sufficiently high temperatures the oxidation of coating and droplet material provides an efficient mechanism to enhance the wear resistance of TiAlN based coatings (see Fig. 1 and ref. [29]). The SEM cross-sections prepared on several droplets within the wear track of coatings tested at 700 °C lead to the conclusion, that these droplets are more efficiently embedded into the coating matrix compared to those in samples tribologically tested at RT.

XRD investigations yielded no significant microstructural change of the whole coating material during 700 °C exposure. Both, the as-deposited coating and the sample tested at 700 °C show a face-centered cubic structure with a (100) preferred orientation. No signs of spinodal decomposition or subsequent phase transformation as reported by Mayrhofer *et al.*

[30] were found, which indicates that the activation temperature for decomposition of the metastable TiAlN phase was not yet reached. This is also corroborated by the coating hardness, where nanoindenation measurements on the as-deposited sample yielded a hardness of 33 ± 1.7 GPa. Considering the low amount of Ta within the coating [14], this value corresponds well to those for unalloyed TiAlN reported by Kutschej *et al.* [31]. Hardness measurements of the coated sample after tribologically testing at 700 °C yielded a value of 32 ± 2.6 GPa. This slightly decreasing hardness can be related to recovery processes as the testing temperature was above deposition temperature [32, 33]. So neither a change in the crystallographic structure nor hardening effects seem to contribute to the obtained lower wear coefficient at 700 °C.

It could be speculated that the enhanced wear resistance at 700 °C is related to the commonly observed and within this study confirmed lower coefficient of friction [14, 29, 31], which is caused by the formation of a protective oxide scale [34]. Moreover, the reported significantly reduced fracture probability of TiAlN coatings at higher temperatures [35] should contribute to the reduction of the wear coefficient. Likewise, the expected pronounced softening of metallic droplets at elevated temperatures might lead to a lower fraction of collapsed droplets; see e.g. ref. [36] for the significantly reduced flow stresses for titanium with increasing temperature.

Nevertheless, also oxidation of droplets and their surrounding areas strongly contribute to the wear resistance. After testing at 700 °C, surface-near cavities around and above collapsed droplets were found to be filled with oxidized material, which was identified as accumulated wear debris. In cracks formed by shear stresses in the neighborhood of droplets and underdense areas around the droplet, also oxidized coating material was found. However, these areas are not originating from wear debris, since there are no sufficient paths for material migration (i.e. from the tribological contact area to e.g. the crack, see Fig. 4d, or to the underdense area below the droplet, see Fig. 8b) are often missing. In contrast, these areas are formed by the inward diffusion of oxygen, as described in detail by Hörling *et al.* [10].

The discussed oxidation mechanism seems to mechanically stabilize droplets within the coating matrix, subsequently enhancing the overall wear resistance. This could be regarded as an oxidation-triggered self-healing effect [37]. In addition, there is less abrasive debris present within the sliding contact if less droplets collapse. Both mechanisms, in combination with the well described formation of stable oxide scales [14, 34], lead to the observed higher wear resistance of arc evaporated TiAlN-based coatings at elevated temperatures.

5. Conclusions

The aim of the present work was to illuminate mechanisms responsible for degradation of arc evaporated TiAlTaN hard coatings with their growth-inherent droplets in dry sliding contacts. Mild abrasive wear was found for room temperature ball-on-disk testing for defect-free areas within the wear track. In contrast, for coating areas with droplets three different responses to tribological testing could be distinguished:

i. The droplets are mechanically stable; wear is comparable to the surrounding coating matrix and no cracks are generated.

ii. During mechanical loading of the droplet, cracks are induced in the coating matrix, due to the formed shear stresses.

iii. The droplet collapses due to the applied tribological load, resulting in the release of droplet fragments into the wear track, where they act as abrasive medium leading to increased wear.

In addition to the formation of oxide scales on top of the coating, the significantly lower wear coefficient obtained during tribological testing at 700 °C can be related to an oxidation induced self-healing mechanism, which results in more efficient embedment of the droplets within the coating matrix.

Acknowledgements

The authors are grateful to Nina Schalk for fruitful discussions and scientific support whenever needed. Financial support by the Austrian Federal Government (in particular from the Bundesministerium für Verkehr, Innovation und Technologie and the Bundesministerium für Wirtschaft, Familie und Jugend) and the Styrian Provincial Government, represented by Österreichische Forschungsförderungsgesellschaft mbH and by Steirische Wirtschaftsförderungsgesellschaft mbH, within the research activities of the K2 Competence Centre on “Integrated Research in Materials, Processing and Product Engineering”, operated by the Materials Center Leoben Forschung GmbH in the framework of the Austrian COMET Competence Centre Programme, is gratefully acknowledged.

References

[1] F. Klocke, T. Krieg, K. Gerschweiler, R. Fritsch, V. Zinkann, M. Pöhls, G. Eisenblätter, Improved cutting processes with adapted coating systems, Annals of the CIRP 47 (1998) 65-68

[2] F. Klocke, T. Krieg, Coated tools for metal cutting – features and applications, Annals of the CIRP Vol. 48 (1999) 515-525

[3] F. Klocke, G. Eisenblätter, Dry cutting, Annals of the CIRP Vol. 46 (1997) 519-526

[4] W. Kalss , A. Reiter, V. Derflinger, C. Gey, J.L. Endrino, Modern coatings in high performance cutting applications, Int. J. Refract. Metal. Hard Mater. 24 (2006) 399–404

[5] J. Rech, A. Kusiak, J.L. Battaglia, Tribological and thermal functions of cutting tool coatings, Surf. Coat. Technol. 186 (2004) 364– 371

[6] M. Meozzi, Special use of the ball-on-disc standard test, Tribol. Int. 39 (2006) 496–505

[7] M. Pfeiler, G.A. Fontalvo, J. Wagner, K. Kutschej, M. Penoy, C. Michotte, C. Mitterer, M. Kathrein, Arc evaporation of Ti–Al–Ta–N coatings: The effect of bias voltage and Ta on high-temperature tribological properties, Tribol. Lett. 30 (2008) 91–97

[8] S.E. Franklin, J. Beuger, A comparison of the tribological behaviour of several wear-resistant coatings, Surf. Coat. Technol. 54 (1992) 459-465

[9] R.L. Boxman, S. Goldsmith, Macroparticle contamination in cathodic arc coatings: generation, transport and control, Surf. Coat. Technol. 52 (1992) 39-50

[10] A. Hörling, L. Hultman, M. Odén, J. Sjölén, L. Karlsson, Thermal stability of arc evaporated high aluminum-content $Ti_{1-x}Al_xN$ thin films, J. Vac. Sci. Technol. A 20 (2002) 1815-1823

[11] P. Harlin, U. Bexell, M. Olsson, Influence of surface topography of arc-deposited TiN and sputter-deposited WC/C coatings on the initial material transfer tendency and friction characteristics under dry sliding contact conditions, Surf. Coat. Technol. 203 (2009) 1748–1755

[12] R. Rachbauer, D. Holec, P.H. Mayrhofer, Increased thermal stability of Ti–Al–N thin films by Ta alloying, Surf. Coat. Technol. 211 (2012) 98–103

[13] G. List, G. Sutter, A. Bouthiche, Cutting temperature prediction in high speed machining by numerical modelling of chip formation and its dependence with crater wear, Int. J. Mach. Tool Manuf. 54–55 (2012) 1–9

[14] M. Pfeiler, C. Scheu, H. Hutter, J. Schnöller, C. Michotte, C. Mitterer, M. Kathrein, On the effect of Ta on improved oxidation resistance of Ti–Al–Ta–N coatings, J. Vac. Sci. Technol. A 27 (2009) 554-560

[15] K. Kutschej, P.H. Mayrhofer, M. Kathrein, P. Polcik, C. Mitterer, Influence of oxide phase formation on the tribological behaviour of Ti–Al–V–N coatings, Surf. Coat. Technol. 200 (2005) 1731 – 1737

[16] M.G. Faga, G. Gautier, R. Calzavarini, M. Perucca, E. Aimo Boot, F. Cartasegna, L. Settineri, AlSiTiN nanocomposite coatings developed via Arc Cathodic PVD: Evaluation of wear resistance via tribological analysis and high speed machining operations, Wear 263 (2007) 1306–1314

[17] G.G. Fuentes, E. Almandoz, R. Pierrugues, R. Martínez, R.J. Rodríguez, J. Caro, M. Vilaseca, High temperature tribological characterisation of TiAlSiN coatings produced by cathodic arc evaporation, Surf. Coat. Technol. 205 (2010) 1368–1373

[18] T. Polcar, A. Cavaleiro, High-temperature tribological properties of CrAlN, CrAlSiN and AlCrSiN coatings, Surf. Coat. Technol. 206 (2011) 1244–1251

[19] M. Pohler, R. Franz, J. Ramm, P. Polcik, C. Mitterer, Cathodic arc deposition of $(Al,Cr)_2O_3$: Macroparticles and cathode surface modifications, Surf. Coat. Technol. 206 (2011) 1454–1460

[20] W.D. Münz, D.B. Lewis, S. Creasey, T. Hurkmans, T. Trinh, W.v. Ijzendorn, Defects in TiN and TiAlN coatings grown by combined cathodic arc/unbalanced magnetron technology, Vacuum 4 (1995) 323-330

[21] A. Anders, Cathodic Arcs: From Fractal Spots to Energetic Condensation, 1st edition Springer, New York, 2008

[22] H. Ljungcrantz, L. Hultman, J.E. Sundgren, G. Håkansson, L. Karlsson, Microstructural investigation of droplets in arc-evaporated TiN films, Surf. Coat. Technol. 63 (1994) 123-128

[23] J. Neidhardt, M. O'Sullivan, A.E. Reiter, W. Rechberger, W. Grogger, C. Mitterer, Structure–property–performance relations of high-rate reactive arc-evaporated Ti–B–N nanocomposite coatings, Surf. Coat. Technol. 201 (2006) 2553–2559

[24] G. Stachowiak, A.W. Betchelor, Engineering Tribology, 3rd edition, Elsevier, Burlington, 2005

[25] Y. Chen, D.J. Young, B. Gleeson, A new Ti-rich ternary phase in the Ti-Al-O system, Mater. Lett. 22 (1995) 125-129

[26] X.L. Li, R. Hillel, F. Teyssandier, S.K. Choi, F.J.J. Van Loo, Reactions and phase relations in the Ti-Al-O system, Acta. Metal. Mater. 40 (1992) 3149-3157

[27] M.X. Zhang, K.C. Hsieh, J. DeKock, Y.A. Chang, Phase diagram of Ti-Al-O at 1100 °C, Scripta Metall. Mater. 27 (1992) 1361-1366

[28] H.O. Pierson, Handbook of Refractory Carbides & Nitrides, William Andrew/Noyes, Park Ridge, 1996

[29] T. Weirather, K. Kutschej, D. Caliskanoglu, R. Cremer, W. Kölker, J. Kohlscheen, C. Mitterer, High temperature sputter deposition of $Ti_{1-x}Al_xN$ coatings on powder metallurgical high speed steels, Proceedings of the 8th International Tooling Conference, RWTH Aachen University, Aachen, (2009) 881-889

[30] P.H. Mayrhofer, A. Hörling, L. Karlsson, J. Sjölén, T. Larsson, C. Mitterer, L. Hultman, Self-organized nanostructures in the Ti–Al–N system, Appl. Phys. Lett. 83 (2003) 2049-2051

[31] K. Kutschej, P.H. Mayrhofer, M. Kathrein, P. Polcik, R. Tessadri, C. Mitterer, Structure, mechanical and tribological properties of sputtered $Ti_{1-x}Al_xN$ coatings with $0.5 \leq x \leq 0.75$, Surf. Coat. Technol. 200 (2005) 2358– 2365

[32] P.H. Mayrhofer, C. Mitterer, L. Hultman, H. Clemens, Microstructural design of hard coatings, Prog. Mater. Sci. 51 (2006) 1032–1114

[33] K.J. Martinschitz, R. Daniel, C. Mitterer, J. Keckes, Stress evolution in CrN/Cr coating systems during thermal straining, Thin Solid Films 516 (2008) 1972–1976

[34] D. McIntyre, J.E. Greene, G. Håkansson, J.E. Sundgren, W.-D. Münz, Oxidation of metastable single-phase polycrystalline $Ti_{0.5}Al_{0.5}N$ films: Kinetics and mechanisms, J. Appl. Phys. 67 (1990) 1542-1553

[35] B.D. Beake, J.F. Smith, A. Gray, G.S. Fox-Rabinovich, S.C. Veldhuis, J.L. Endrino, Investigating the correlation between nano-impact fracture resistance and hardness/modulus ratio from nanoindentation at 25–500 °C and the fracture resistance and lifetime of cutting tools with $Ti_{1-x}Al_xN$ (x=0.5 and 0.67) PVD coatings in milling operations, Surf. Coat. Technol. 201 (2007) 4585-4593

[36] Z. Zeng, Y. Zhang, S. Jonsson, Deformation behaviour of commercially pure titanium during simple hot compression, Mater. Design 30 (2009) 3105–3111

[37] G.M. Song, Y.T. Pei, W.G. Sloof, S.B. Li, J.Th.M. De Hosson, S. van der Zwaag, Oxidation-induced crack healing in Ti_3AlC_2 ceramics, Scripta mater. 58 (2008) 13-16

Publication II

Residual stress gradients in α-Al_2O_3 hard coatings determined by pencil-beam X-ray nanodiffraction: The influence of blasting media

Michael Tkadletz, Jozef Keckes, Nina Schalk, Ivan Krajinovic, Manfred Burghammer, Christoph Czettl, Christian Mitterer

Surface and Coatings Technology 262 (2015) 134-140

Residual stress gradients in α-Al_2O_3 hard coatings determined by pencil-beam X-ray nanodiffraction: The influence of blasting media

Michael Tkadletz[1], Jozef Keckes[2], Nina Schalk[3], Ivan Krajinovic[1], Manfred Burghammer[4, 5], Christoph Czettl[6], Christian Mitterer[3]

[1]*Materials Center Leoben Forschung GmbH, Roseggerstraße 12, A-8700 Leoben, Austria*

[2]*Department of Materials Physics, Montanuniversität Leoben, Jahnstrasse 12, A-8700 Leoben, Austria*

[3]*Department of Physical Metallurgy and Materials Testing, Montanuniversität Leoben, Franz-Josef-Straße 18, A-8700 Leoben, Austria*

[4] *ESRF, F-38043 Grenoble Cedex 9, France*

[5]*Department of Analytical Chemistry, Ghent University, Krijgslaan 281, S12, B-9000 Ghent, Belgium*

[6]*CERATIZIT Austria GmbH, Metallwerk-Plansee-Straße 71, A-6600 Reutte, Austria*

Contact: michael.tkadletz@mcl.at

Abstract

Post-deposition blasting treatments are widely used to introduce compressive residual stress into CVD hard coatings, which are typically in a tensile stress state after deposition on cemented carbide substrates. Within this work, α-Al_2O_3 coatings grown by CVD on TiCN base-layers were dry-blasted using a globular as well as an edged blasting medium and subsequently annealed at 900 °C. The as-deposited, blasted and annealed samples were characterized using cross-sectional synchrotron X-ray nanodiffraction using a pencil X-ray beam of 10 µm x 100 nm in size as well as complementary synchrotron energy dispersive and laboratory monochromatic X-ray diffraction. The results document that the maximum compressive stress of 4 GPa in the samples blasted with the edged medium is significantly higher compared to the samples blasted with the globular medium, which showed maximum compressive stress of 2 GPa. The stress gradient obtained after blasting with the edged medium is steeper, while the zone with compressive stress reaches deeper into the coating for the samples blasted with the globular medium. In the substrate, significantly increased compressive stress of 400 ± 60 MPa compared to 90 ± 30 MPa in the as-deposited state was observed only after blasting with the globular medium and relaxed fully after annealing. In

addition, the observed stress gradients were corroborated by the particle impact using a finite element contact mechanics approach.

Keywords: Hard coatings; X-ray diffraction; nanodiffraction; pencil X-ray beam; blasting treatment; α-Al_2O_3

1. Introduction

Al_2O_3 hard coatings deposited by chemical vapor deposition (CVD) on cemented carbide are widely used in cutting applications due to their high wear resistance and beneficial high temperature properties [1–3]. However, one major drawback of CVD are the high deposition temperatures around 1000 °C, which result in the evolution of tensile residual stress due to the mismatch of the thermal expansion coefficients of the coating and the substrate material [4–6]. Consequently, crack networks are formed during cooling after deposition which negatively affect the tools lifetime as they decrease the mechanical stability of the coating. These crack networks also provide diffusion paths and consequently foster diffusion wear and oxidation [7,8]. In the last years, special attention has been paid to overcome the negative effects of these tensile residual stresses. By applying post-deposition treatments like wet- or dry blasting, compressive residual stress can be introduced into the coating [9,10], which positively affects its mechanical properties [11–13]. In addition, it has been reported that carefully chosen blasting parameters can result in a change of the stress state of the substrate material as well [9]. That might further increase the tools lifetime if the formation of comb-cracks, which is reported to correlate with the formation of tensile residual stress in the substrate [14], can be delayed.

In a previous work, Schalk *et al*. have shown that the magnitude of compressive stresses introduced by blasting can be significantly influenced by the chosen blasting medium and blasting pressure. Full relaxation of the introduced stress was observed after annealing at 900 °C [15]. Bartosik *et al*. demonstrated that annealing of blasted TiN hard coatings results in stress relaxation already at 200 °C and higher annealing temperatures result in the buildup of even higher tensile stresses after cooling down [16]. However, the stress characterizations within those works were performed using the conventional $\sin^2\psi$ method; thus, no depth resolved information about the stress gradients after blasting or annealing was obtained.

The aim of this work is to perform a detailed characterization of residual stress and microstructure gradients in blasted α-Al_2O_3 hard coatings using the recently developed synchrotron cross-sectional X-ray nanodiffraction [17]. Since this approach operates with a point X-ray beam of about 100 nm in diameter [17], it was modified in order to achieve

sufficient diffraction statistics for coarse grained materials like CVD α-Al_2O_3 coatings with a grain size in the µm range. For this purpose, an X-ray beam with a pencil-like shape similarly to Vaxelaire *et al.* [18] was applied to as-deposited, blasted and annealed α-Al_2O_3 coatings. Complementary, laboratory monochromatic X-ray diffraction (XRD) and energy dispersive synchrotron polychromatic XRD were used to obtain volume-averaged data from the coatings and substrates. To analyze the effect of the blasting media on the stress formation in the coating surface, finite element (FE) simulations were performed using the software package Abaqus*/Explicite 6.13-3*.

2. Experimental and Theoretical Methods

The coatings investigated within this work were deposited using a SuCoTec SCT600TH industrial-scale CVD plant. Cemented carbide inserts in SNUN 120412 geometry (according to ISO 1832) with a chemical composition of 77 wt% tungsten carbide, 12 wt% mixed carbides and 11 wt% cobalt were used as substrates. A TiCN base-layer [19] with a thickness of ~9 µm was deposited using $TiCl_4$-CH_3CN-H_2-N_2-CO precursors at a temperature of 900 °C and a pressure of 100 mbar. Afterwards, the ~8 µm thick α-Al_2O_3 layer was grown using $AlCl_3$-CO_2-H_2-H_2S precursors at a temperature of 1000 °C and a pressure of 75 mbar [20]. Subsequently, the samples were dry blasted using (i) a globular medium provided by Kuhmichel Abrasiv shown in Fig. 1a and (ii) an edged medium provided by Treibacher Schleifmittel shown in Fig. 1b. The globular medium has a particle diameter of 125-250 µm, a hardness of ~700 HV and a phase composition of ~62 % ZrO_2, ~28 % SiO_2 and ~5 % Al_2O_3 (remaining fraction ceramic impurities). The mesh grit size of the edged medium is 180/220, the hardness ~2000 HV and the phase composition is ~55 % Al_2O_3 and ~42 % ZrO_2 (remaining fraction ceramic impurities). The chosen blasting pressure was 1.5 bar, applied under a working angle of 15° for a time of 14 s.

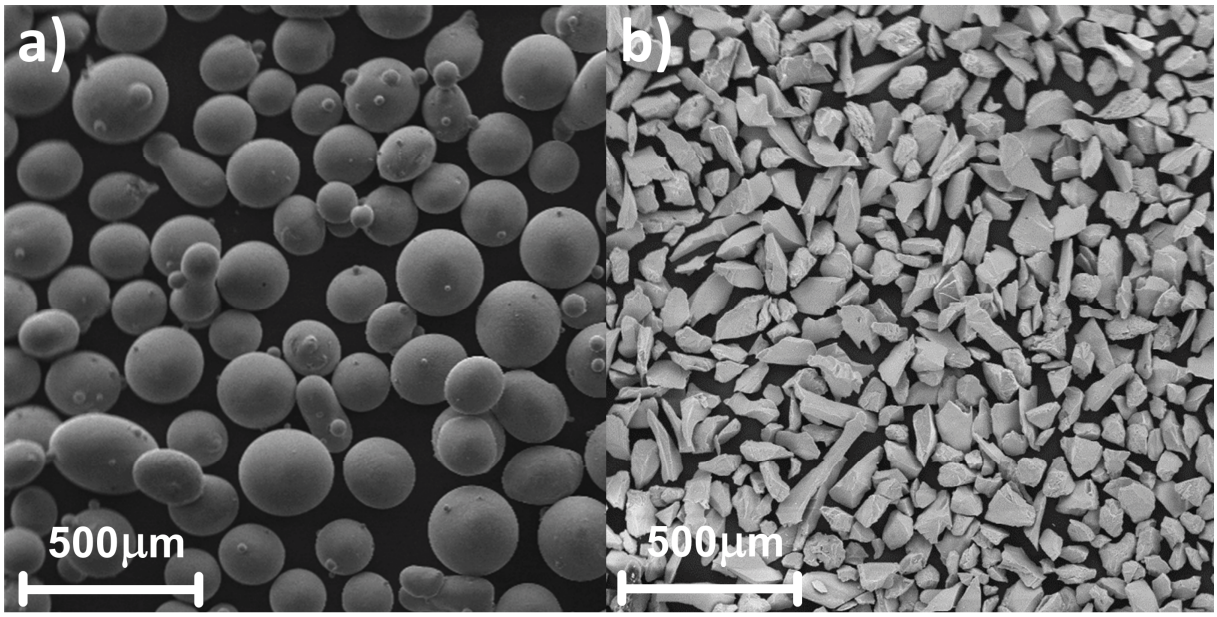

Fig. 1: *SEM micrograph of the globular (a) and the edged (b) blasting medium.*

The blasted samples were tempered at 900 °C for 15 min in a HTM Reetz vacuum furnace (base pressure <5 x 10^{-4} Pa), using a heating rate of 20 K/min and a cooling rate of 60 K/min. The laboratory XRD investigations of the coatings were performed using a Rigaku SmartLab five-axis X-ray diffractometer equipped with Cu-K_α radiation, a parabolic multilayer mirror in the primary beam and a secondary graphite monochromator. The stress characterization was performed using the conventional $\sin^2\psi$ method [21]. All scanning electron microscopy (SEM) investigations were performed using a Zeiss Auriga Crossbeam field emission gun SEM. The electron backscatter diffraction (EBSD) measurement was performed with an EDAX DigiView IV EBSD detector. Prior to the EBSD measurement, the surface of the fracture cross section was polished with an Orsay Physics Cobra Z-05 focused ion beam (FIB) extension.

For the cross-sectional X-ray nanodiffraction experiments, 100-150 µm thick lamellae were cut out from the samples using a Struers Accutom precision saw equipped with a diamond cutting wheel. Subsequently, the lamellae were manually polished down to a thickness of approximately 30 to 50 µm. The synchrotron measurements were performed at the nano-focus extension of the ID13 beamline of the European Synchrotron Radiation Facility (ESRF) in Grenoble, France using a monochromatic X-ray beam with an energy of 14.9 keV. A conventional cross-sectional X-ray nanodiffraction setup operating with a beam diameter of 100 nm did not provide sufficient diffraction statistics as demonstrated by the spotty diffraction pattern from the charge-coupled device (CCD) in Fig. 2a. Therefore, a pencil-shaped X-ray nanobeam with dimensions of 10 µm x 100 nm was implemented for this study using dedicated focusing optics [22]. The diffraction experiment using the pencil beam

aligned parallel to the coating-substrate interface resulted in a significant improvement of the diffraction statistics, as demonstrated in Fig. 2b.

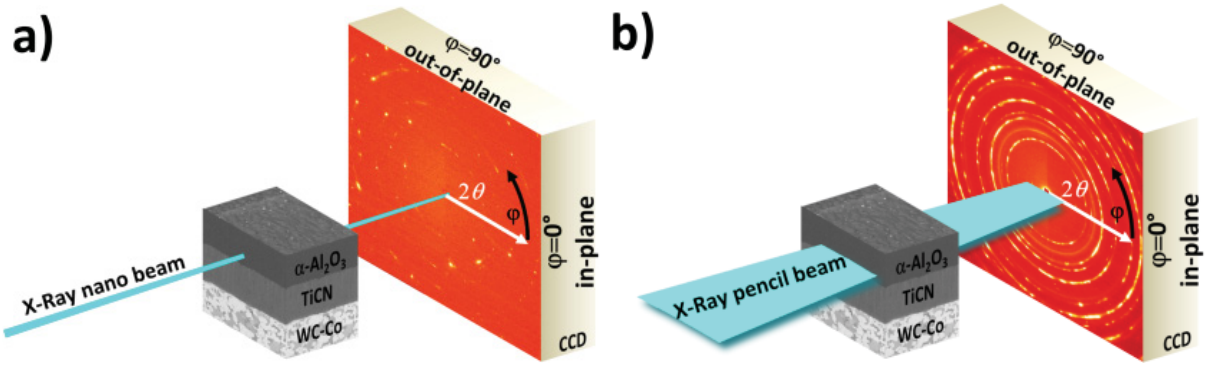

Fig. 2: *Schematic description of the cross-sectional X-ray nanodiffraction setup according to [17] (a) and the setup using a pencil-like X-ray nano-beam (b). The two dimensional images indicate an improved diffraction statistics of the Debye-Scherrer rings in (b).*

The lamellar samples were scanned in transmission geometry along the coating depth in steps of 100 nm and the two dimensional data (2D) from the CCD were evaluated using the software package Fit2D [23]. To achieve even better diffraction statistics, for each coating depth five measurements were performed at different positions and the 2D patterns were summed. The residual X-ray elastic strain at different coating depths was evaluated from the elliptical distortion of the Debye-Scherrer rings of TiCN (111) and α-Al_2O_3 (104) reflections according to [17,24]. To derive the residual stress from the residual strain, the X-ray elastic constants (XEC) were used which were determined from the single crystal elastic constants [25,26] using the Kröner-model [27].

The residual stress state in the surface region of the cemented carbide substrates was determined at the materials science synchrotron-beamline EDDI (Energy Dispersive Diffraction) of the synchrotron source BESSY in Berlin, Germany using energy dispersive XRD as specified in Ref. [28,29]. Volume-averaged residual stresses were calculated from the measured X-ray elastic strains, determined from the shift of substrate WC (001) reflections by applying XEC from Ref. [30]. The experimental conditions corresponded to an information depth of approximately 500 nm.

The FE simulations were performed using the software package *Abaqus/Explicite 6.13-3*. An axisymmetric model was defined with a spherical body similar to the globular blasting medium and a sample with a substrate/coating architecture close to the samples used in the experiments. For the cemented carbide, a density of 13.23 g/cm³ was determined using the Archimedes principle [31]. The Poisson ratio of 0.22 and Young´s modulus of 617 GPa were obtained by resonant ultrasound spectroscopy [32]. In order to get information about the

stress-strain data uniaxial compression tests were performed. For the coatings, literature values for density (5.22 g/cm³ for TiCN and 3.95 g/cm³ for α-Al_2O_3) and Poisson ratio (0.19 for TiCN and 0.234 for α-Al_2O_3) were used [33–35]. The Young´s moduli of 570 GPa for TiCN and 465 GPa for α-Al_2O_3 were determined by nanoindentation according to Oliver and Pharr [36]. For each coating at least 15 indents were performed using a Berkovich indenter. Choosing a load range of 15 to 25 mN, the indentation depth was kept below 10% of the layer thickness. The stress-strain data of the coatings were determined by inverse modeling of the load-displacement curves derived from the nanoindentation experiments [37]. The surface roughness of the coatings was determined using a NanoFocus µSurf white-light confocal microscope and was implemented into the FE model. For the blasting media which were defined as elastic bodies, a density of 3.7 g/cm³, a Poisson ratio of 0.22 and a Young´s modulus of 165 GPa were estimated. The blasting parameters were varied in terms of size and velocity of the shots from Ø 150 to Ø 250 µm and 165 to 300 m/s. To approximate the small contact radius of an edged particle, additionally a shot with Ø 20 µm and the mass of an Ø 75 µm ball was simulated.

3. Results and Discussion

3.1 As-deposited state

In Figure 3, a representative XRD pattern from the as-deposited sample is presented. The peak positions for α-Al_2O_3 and TiCN, according to ICDD 00-042-1468 and 01-076-2484, respectively, are indicated. The pattern reveals the presence of α-Al_2O_3 and TiCN crystalline phases for the top and the base layer, respectively. Weak peaks (e.g. at 48°) which are not indicated are related to the cemented carbide substrate.

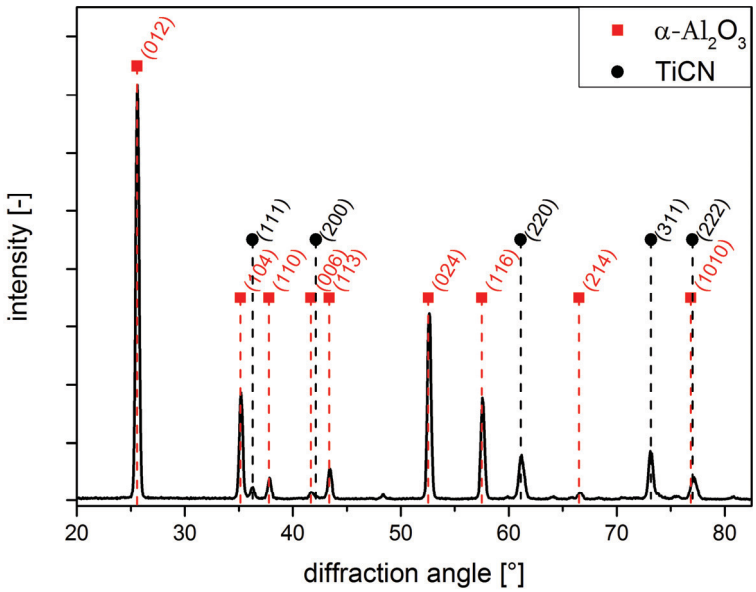

Fig. 3: *X-ray diffractogram of the as-deposited sample.*

A SEM micrograph of a fracture cross-section of the sample is shown in Fig. 4a and a SEM micrograph including a superimposed EBSD measurement of the same sample can be found in Fig. 4b. Both figures reveal a fine grained nucleation zone of the TiCN base-layer followed by a columnar structure with a column diameter of ~1 µm. The α-Al_2O_3 layer shows a nucleation zone at the interface followed by a more or less randomly oriented grain structure with a grain size of approximately 3 to 4 µm.

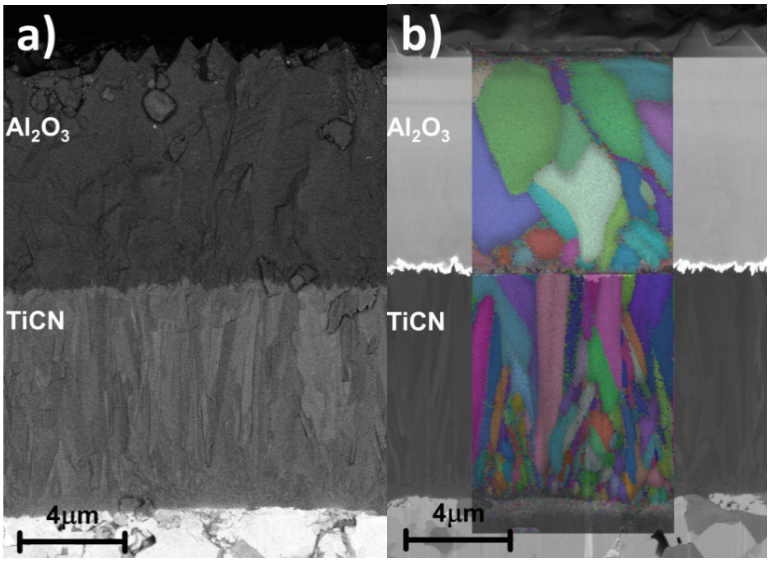

Fig. 4: *SEM of a fracture cross-section of the as-deposited sample (a) and FIB polished cross-section of the same sample showing a superimposed EBSD measurement (b).*

In Fig. 5a the in-plane phase-plot obtained from 2D diffraction patterns collected along the coating depth during the X-ray nanodiffraction experiment on the as-deposited sample is shown. Such phase-plots are created by plotting the intensities of the Debye-Scherrer rings

(Fig. 2b) from a certain azimuthal angle φ range over the vertical scan direction (i.e. the coating thickness). Using that approach, it is possible to display diffraction data from crystallographic planes oriented perpendicular to the interface and tilted θ angle with respect to the sample by choosing the corresponding φ angle of 0° or 90° within the Debye-Scherrer rings. The in-plane phase-plot (φ=0°) of the as-deposited sample reveals a homogenous phase composition over the coating thickness and no peak shift or peak broadening can be detected. The overlapping diffraction lines at the interface between α-Al_2O_3 and TiCN base-layer can be related to a certain interface roughness and a slight misalignment of the pencil beam. The in-plane stress-depth-profile in Fig. 5b shows a constant stress level over the whole coating thickness for the TiCN base- layer as well as for the α-Al_2O_3. For both layers, tensile residual stress in the range of several hundred MPa was determined by nanodiffraction and additionally confirmed by laboratory XRD measurements. The energy dispersive synchrotron investigations revealed low compressive residual stress of 95 ± 40 MPa in the surface near region of the cemented carbide substrate.

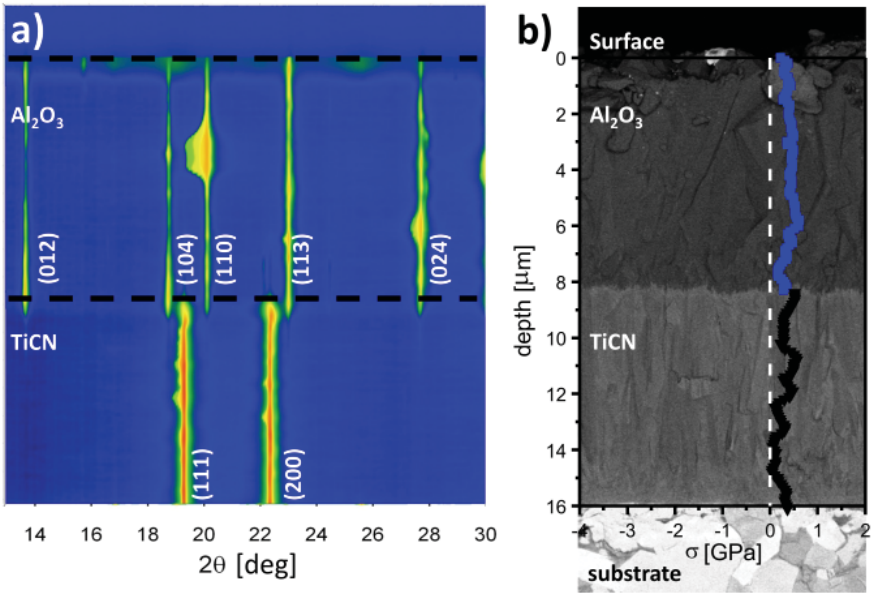

Fig. 5: *In-plane phase-plot of the as-deposited sample (a) and corresponding stress-depth-profile (b).*

3.2 Blasted state

The in-plane phase-plots (φ=0°) derived from the nanodiffraction measurements of the blasted samples are shown in Figs. 6a and b for the globular and the edged medium, respectively. Both samples show no significant changes within the TiCN base-layer. However, the reflections of the α-Al_2O_3 layer exhibit a distinct peak broadening and peak shift in the surface near region for both samples. Those effects are even more pronounced for the sample blasted with the edged medium (Fig. 6b). The peak shift can be related to

compressive stress which reduces the in-plane lattice parameter [24] and consequently, increases the diffraction angle, while the peak broadening can be attributed to an increased defect density and/or a reduced size of coherently diffracting domains [38,39].

A detailed in-plane phase-plot (φ=0°) of the surface near region of the α-Al_2O_3 layer blasted with the edged medium and the corresponding out-of-plane phase-plot (φ=90°) are shown in Figs. 6c and d to illustrate the effect of introduced in-plane stress to the different crystallographic planes. The range of the diffraction angle 2θ, from 18 to 24°, includes α-Al_2O_3 (104), (110), (006) and (113) reflections. However, not every reflection is visible in the phase-plots determined for certain azimuthal angles. The visibility of reflections strongly depends on the texture of the measured sample and the chosen azimuthal angle, which is used to create the phase-plot as the crystallographic orientation determines the distribution of the intensity within the Debye-Scherer rings [40,41]. Both phase-plots exhibit very strong (104) and (113) reflections and if they are compared to each other, it can be seen that the in-plane phase-plot (φ=0°, Fig. 6c) shows a reflection shift to higher diffraction angles towards the surface, while the out-of-plane phase-plot (φ=90°, Fig. 6d) shows a shift to lower diffraction angles. These effects can be related to induced in-plane compressive residual stress [24] and indicate the reaction of differently oriented crystallographic planes to residual stress. If the lattice planes are perpendicular to the surface, the lattice parameter is decreasing as a reaction to the compressive stress while it is increasing if the planes are oriented parallel to the surface. The out-of-plane peak shift is less pronounced compared to the in-plane peak shift; this is related to the Poisson's ratio determining the out-of-plane lattice distortion [38]. The Poisson´s ratio is typically in the range of ~0.23 to ~0.26 for α-Al_2O_3 [33,42].

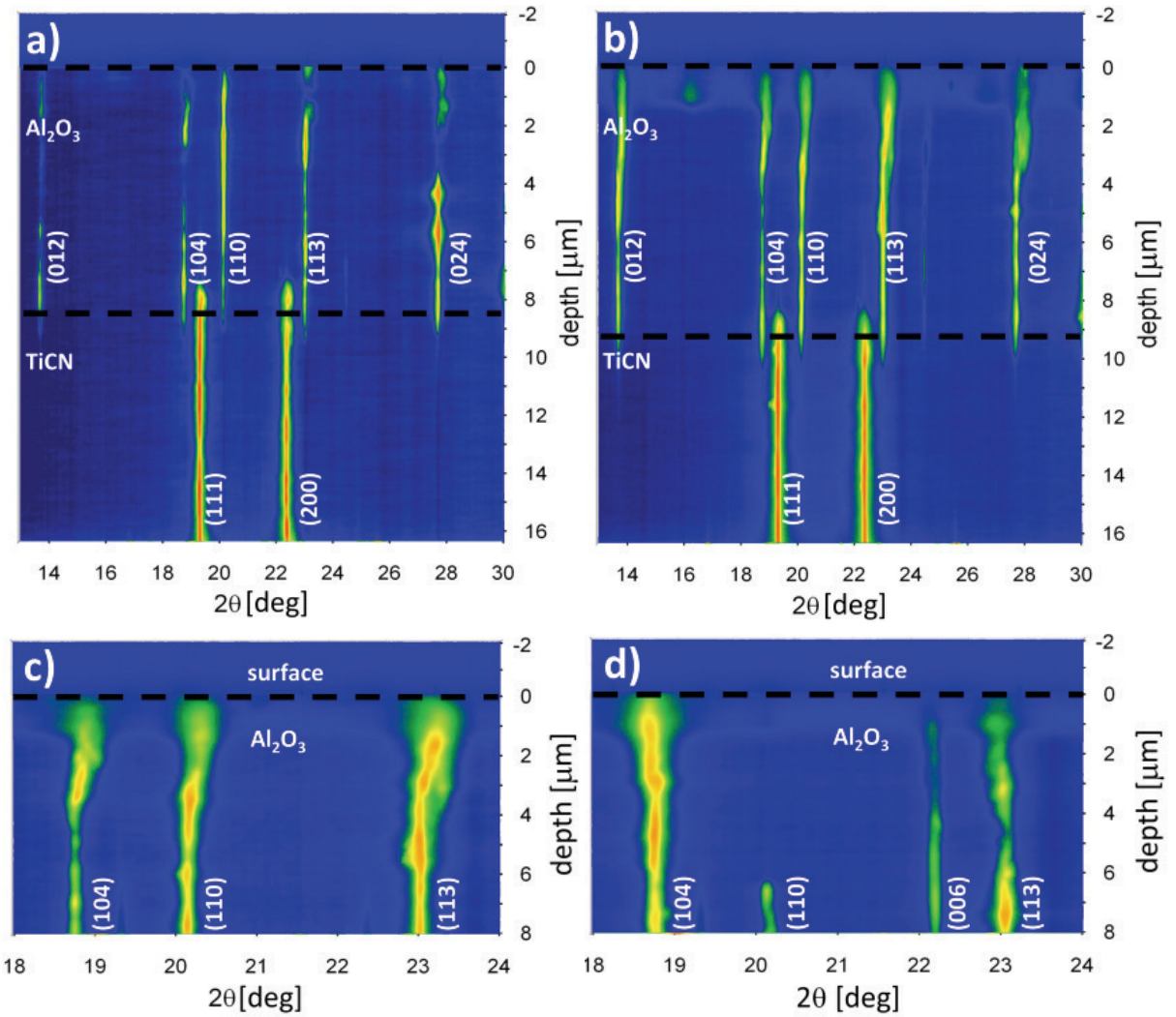

Fig. 6: *In-plane phase-plot of the sample blasted with the globular (a) and the edged medium (b). Detailed phase-plot of the surface near region of the sample blasted with the edged medium for the in-plane (c) and the out-of-plane direction (d) indicate a presence of high compressive stresses. The peak broadening can be interpreted by the increased strains of II. and III. order as well as by the smaller size of the coherently diffracting domains formed after the blasting.*

The in-plane residual stress-depth-profiles, shown in Figs. 7a for the samples blasted with the globular and 7b for the samples using the edged medium, highlight the difference between both blasting media. In comparison to the as-deposited state (Fig. 5b), both samples exhibit a slightly changed stress level in the TiCN base-layer, while the stress in the α-Al_2O_3 layer changed significantly from tensile to compressive. The sample blasted with the globular medium (Fig. 7a) shows a maximum compressive stress of ~2 GPa, while the sample blasted with the edged medium (Fig. 7b) exhibits a maximum compressive stress level of almost 4 GPa. The gradient of the stress is less pronounced within the sample blasted with the globular medium, the stress change is ~1 GPa per µm. In contrast, the gradient induced

by the edged medium is much steeper and the stress decreases by almost 4 GPa within 1 µm. The affected zone for both samples reaches ~4 µm into depth. But in contrast to the sample blasted with the globular medium, which only shows compressive stress, the sample blasted with the edged medium shows a tensile peak in a depth of 3-4 µm and an area of reduced stress in the surface near region. Stress-depth-profiles with such a shape can be found in literature for shot-peened steels and other metals [43,44].

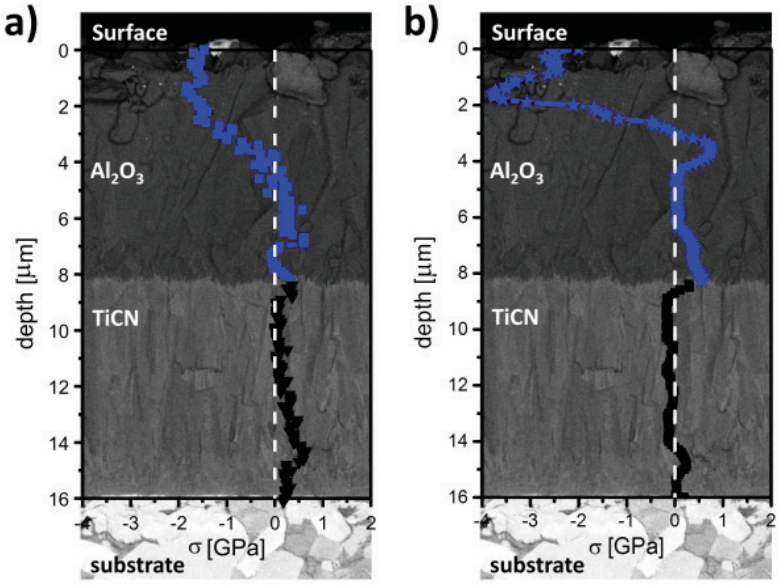

Fig. 7: *Residual stress-depth-profiles in the samples blasted with the globular (a) and edged (b) media.*

Considering the differences in the two blasting media, the determined stress profiles can be explained by simple contact mechanics. The edged medium has due to its smaller size a lower mass, smaller contact radii due to the edges and a high hardness. These properties promote rather high peak levels of stress and a steep gradient, which is in perfect agreement with the profile measured within this work. The globular medium has a higher mass compared to the edged medium, a lower hardness and resulting big contact radii. These properties promote the formation of stress profiles with reduced maximum stress, which in turn reach rather deep into the material like it was observed for the globular medium within this work [45,46].

The energy dispersive synchrotron measurements of the interface near region of the substrate revealed no significant change of the residual stress for the sample blasted with the edged medium, while the sample blasted with the globular medium showed significantly increased compressive stress of 400 ± 60 MPa compared to the as-deposited coating with 90 ± 30 MPa. This is in good agreement with the results from the nanodiffraction experiments, which revealed that the edged medium has a high impact on the surface near

zone but the affected depth is rather limited. Opposite to that, the globular medium has a less pronounced effect on the surface near region, but affects a high depth even down to the substrate. Blasting treatments of coated samples, which affect the substrate as well, were previously reported by Klaus *et al*. [9].

3.3 Annealed state

The in-plane phase-plots (φ=0°) of the samples blasted with the edged and the globular medium annealed at 900 °C can be found in Figs. 8a and c. No evidence of peak broadening or peak shift in the surface near region can be observed for both samples. The in-plane stress plots (Figs. 8b and d) show low tensile stress in the TiCN base-layer and a significantly reduced compressive stress gradient in the α-Al_2O_3 layer for the sample blasted with the globular medium (Fig. 8b). The sample blasted with the edged medium reveals almost zero stress in the TiCN base-layer and low tensile stress, which is comparable to the as-deposited state, in the α-Al_2O_3 layer (Fig. 8d). A possible reason for the still existing slight gradient in the sample blasted with the globular medium might be, that due to the lower stress which was induced by the blasting treatment, also the driving forces for relaxation are lower compared to the sample blasted with the edged medium. The residual stress measurements of the substrate reveal no change of the stress after annealing within the sample blasted with the edged medium. The increased compressive stress of the sample blasted with the globular medium was almost fully relaxed after annealing (Fig. 8b). The observed relaxation of the stress introduced by blasting treatments during annealing is in good agreement with literature [15,16].

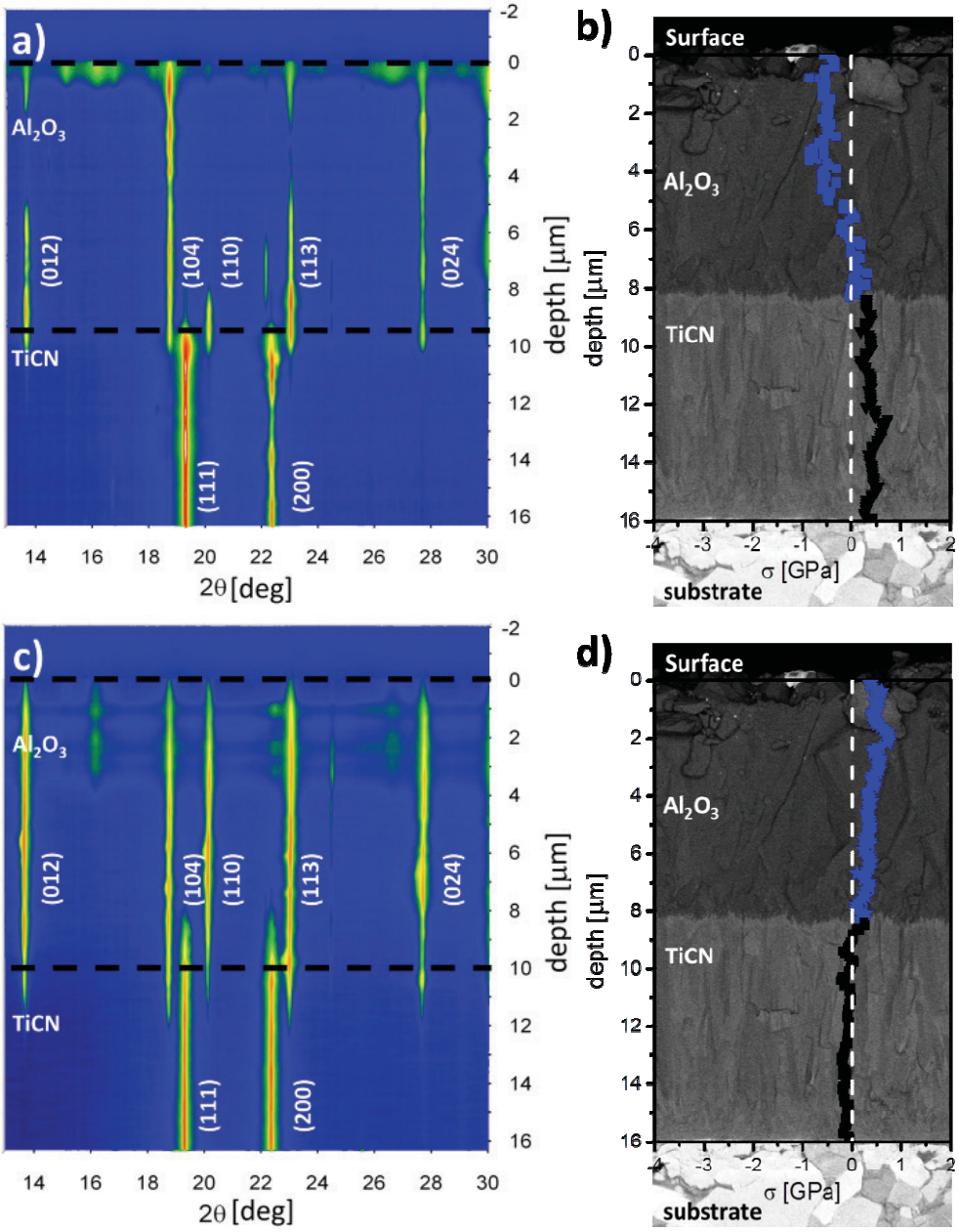

Fig. 8: *In-plane phase-plots for the samples blasted with the globular (a) and edged (c) media after the annealing with the corresponding stress-depth-profiles in (b) and (d).*

3.4 FE simulations

In Fig. 9 results of FE simulations of globular particles impinging on the coating surface can be seen. The images show the residual in-plane plastic strains within the α-Al_2O_3 layer, the TiCN base-layer and the WC grains of the substrate, induced by particles of different size and velocity. Fig. 9a shows the influence of a Ø 150 µm sized particle hitting the surface with a velocity of 165 m/s. In this case, the maximum plastic strain is induced into the α-Al_2O_3 layer. However, the substrate is significantly affected as well, while only a minor influence on the TiCN base-layer can be found. Obviously, also the surface roughness plays a major role as the

maximum induced plastic strain is concentrated at surface asperities, as also observed in [47]. With increasing particle velocity, the plastic strain within both layers as well as in the substrate increases (Fig. 9b for 300 m/s). The same effect, although slightly less pronounced, can be observed for a particle with an increased size of Ø 250 µm and a velocity of 165 m/s (Fig. 9c). If both, particle size and velocity are increased, the highest influence on the plastic strains can be achieved (Fig. 9d). There, in particular the effect on the substrate is very pronounced.

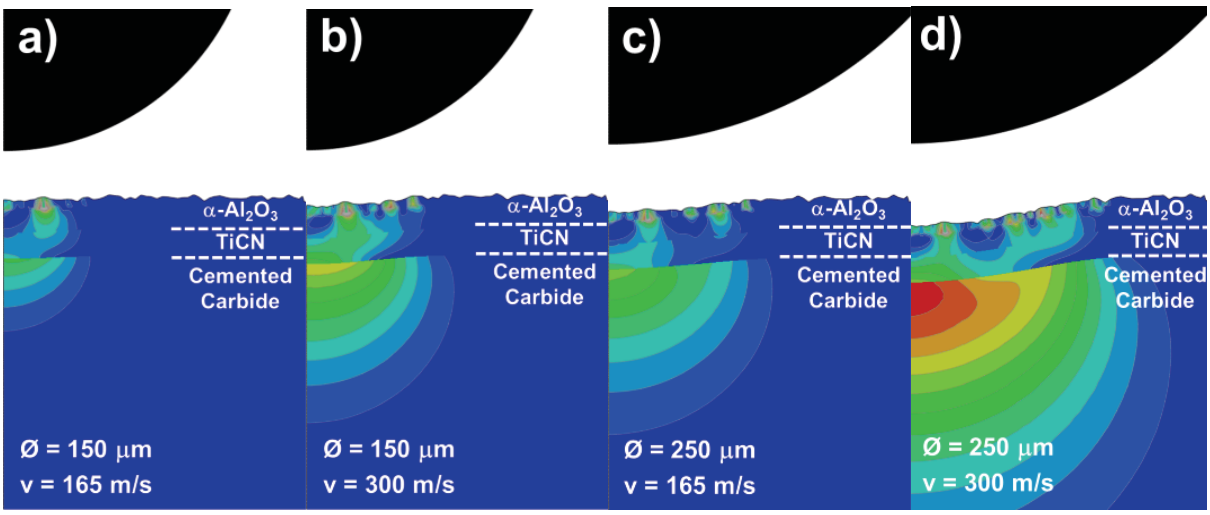

Fig. 9: *FE simulations of introduced plastic residual strains in the samples after impact of a spherical particle with Ø 150 µm and velocity of 165 m/s (a). Evolution of the plastic strains with increasing velocity (b) or size (c) of the shot. Influence of increased size and velocity (d).*

The fact that magnitude of the plastic strains and the affected depth is increasing with velocity and size of the particles, which corresponds to an increase of their kinetic energy, is in good agreement with literature on shot-peening of bulk metals [43–46]. The present simulations show that significant plastic strains can also be introduced into the substrate, if a layered sample comparable to a state-of-the-art coating architecture is considered. This strain within the substrate was even found, when the induced strain in the coating decayed in the first layer. The plastic strains in the substrate consequently result in a change of the residual stress in the substrate, which is in good agreement with the performed measurements and literature [9].

To approximate the impact of an edged particle, a simulation of a spherical particle with a reduced size of Ø 20 µm and an increased density corresponding to the mass of a Ø 75 µm sized particle was performed. Using that approach it was possible to significantly reduce the contact radius of the colliding particle while the mass was kept rather high. The results suggest that the plastic strain after the impact of such a particle is mainly concentrated within the first few microns of the α-Al_2O_3 layer, while the TiCN base-layer and the WC

substrate are almost unaffected. These results are in good agreement with the performed measurements on the sample blasted with the edged medium, which revealed no significant change of the residual stress within the TiCN base-layer or the cemented carbide substrate.

Conclusion

The effect of dry-blasting with a globular and a edged blasting medium on the residual stress of α-Al_2O_3 hard coatings deposited on cemented carbide substrates was investigated using XRD techniques. As the conventional nanodiffraction setup does not provide sufficient diffraction statistics for the coarse grained CVD α-Al_2O_3 samples, a pencil-shaped focused nanodiffraction setup was successfully implemented within this work. Utilizing this setup, phase-plots and the residual in-plane stress-depth-profiles of the samples could be determined with a resolution of ~100 nm. The measurements of the sample blasted with the edged medium revealed stress-depth-profiles with a maximum compressive residual stress of ~4 GPa and a steep stress gradient, while the globular medium resulted in a significantly lower maximum compressive residual stress of ~2 GPa and a less steep gradient. The complementary performed energy dispersive synchrotron investigations showed that the residual stress within the substrate can also be influenced by choosing the appropriate blasting medium and parameters. The experimental findings could also be confirmed by finite element simulations. After annealing to 900 °C, the introduced stress was found to almost completely relax in all samples for both, coating and substrate.

Concluding, the comparison of the two blasting media showed that it is possible to adjust the resulting stress profiles by the choice of the blasting medium and the blasting parameters.

Acknowledgements

The authors want to thank Bernhard Sartory (Materials Center Leoben) for the work on the SEM and Tamara Teppernegg (Materials Center Leoben) for providing material data of the cemented carbide. Further Manuela Klaus (Helmholtz Zentrum Berlin) is highly acknowledged for the energy dispersive synchrotron investigations. Financial support by the Austrian Federal Government (in particular from the Bundesministerium für Verkehr, Innovation und Technologie and the Bundesministerium für Wissenschaft, Forschung und Wirtschaft) and the Styrian Provincial Government, represented by Österreichische Forschungsförderungsgesellschaft mbH and by Steirische Wirtschaftsförderungsgesellschaft mbH, within the research activities of the K2 Competence Centre on “Integrated Research in Materials, Processing and Product Engineering”, operated by the Materials Center Leoben

Forschung GmbH in the framework of the Austrian COMET Competence Centre Programme, is gratefully acknowledged.

Bibliography

[1] S. Ruppi, Advances in chemically vapour deposited wear resistant coatings, J. Phys. IV 11 (2001) Pr3 847–859

[2] B. Lux, R. Haubner, C. Wohlrab, Chemically vapour-deposited hard coatings: Applications and selection guidelines, Surf. Coat. Technol. 38 (1989) 267–280

[3] P.K. Mehrotra, D.T. Quinto, High temperature microhardness profiles of hard CVD coatings, High Temp. High Press. 18 (1986) 199–210

[4] A. Osada, E. Nakamura, H. Homma, T. Hayahi, T. Oshika, Wear mechanism of thermally transformed CVD Al_2O_3 layer, Int. J. Refract. Met. Hard Mater. 24 (2006) 387–391

[5] P. Schlund, P. Kindermann, R. Schulte, H.G. Sockel, U. Schleinkofer, K. Görting, W. Heinrich, Mechanical behaviour of PVD/CVD-coated hard metals under cyclic loads, Int. J. Refract. Met. Hard Mater. 17 (1999) 179–185

[6] S. Vuorinen, L. Karlsson, Phase transformation in chemically vapour-deposited κ-alumina, Thin Solid Films 214 (1992) 132–143

[7] D. Hochauer, C. Mitterer, M. Penoy, S. Puchner, C. Michotte, H.P. Martinz, H. Hutter, M. Kathrein, Carbon doped α-Al_2O_3 coatings grown by chemical vapor deposition, Surf. Coat. Technol. 206 (2012) 4771–4777

[8] X. Chen, H. Liu, Q. Guo, S. Sun, Oxidation behavior of WC–Co hard metal with designed multilayer coatings by CVD, Int. J. Refract. Met. Hard Mater. 31 (2012) 171–178

[9] M. Klaus, C. Genzel, H. Holzschuh, Residual stress depth profiling in complex hard coating systems by X-ray diffraction, Thin Solid Films 517 (2008) 1172–1176

[10] K.-D. Bouzakis, G. Skordaris, F. Klocke, E. Bouzakis, A FEM-based analytical–experimental method for determining strength properties gradation in coatings after micro-blasting, Surf. Coat. Technol. 203 (2009) 2946–2953

[11] P.H. Mayrhofer, C. Mitterer, J. Musil, Structure–property relationships in single-and dual-phase nanocrystalline hard coatings, Surf. Coat. Technol. 174-175 (2003) 725–731

[12] K.-D. Bouzakis, F. Klocke, G. Skordaris, E. Bouzakis, S. Gerardis, G. Katirtzoglou, S. Makrimallakis, Influence of dry micro-blasting grain quality on wear behaviour of TiAlN coated tools, Wear 271 (2011) 783–791

[13] K.-D. Bouzakis, G. Skordaris, E. Bouzakis, Methods for Determining Coating's Strength Properties Changes After Inducing Plastic or Elastic Residual Stresses, Procedia Eng. 19 (2011) 34–39

[14] T. Teppernegg, T. Klünsner, P. Angerer, C. Tritremmel, C. Czettl, J. Keckes, R. Ebner, R. Pippan, Evolution of residual stress and damage in coated hard metal milling inserts over the complete tool life, Int. J. Refract. Met. Hard Mater. 47 (2014) 80–85

[15] N. Schalk, C. Mitterer, C. Czettl, B. Sartory, M. Penoy, C. Michotte, Dry-Blasting of α- and κ-Al_2O_3 CVD Hard Coatings: Friction Behaviour and Thermal Stress Relaxation, Tribol. Lett. 52 (2013) 147–154

[16] M. Bartosik, R. Pitonak, J. Keckes, In Situ High Temperature X-Ray Diffraction Reveals Residual Stress Depth-Profiles in Blasted TiN Hard Coatings, Adv. Eng. Mater. 13 (2011) 705–711

[17] J. Keckes, M. Bartosik, R. Daniel, C. Mitterer, G. Maier, W. Ecker, J. Vila-Comamala, C. David, S. Schoeder, M. Burghammer, X-ray nanodiffraction reveals strain and microstructure evolution in nanocrystalline thin films, Scripta Mater. 67 (2012) 748–751

[18] N. Vaxelaire, P. Gergaud, G.B.M. Vaughan, Sub-micrometre depth-gradient measurements of phase, strain and texture in polycrystalline thin films: a nano-pencil beam diffraction approach, J. Appl. Crystallogr. 47 (2014) 495–504

[19] C. Czettl, C. Mitterer, U. Mühle, D. Rafaja, S. Puchner, H. Hutter, M. Penoy, C. Michotte, M. Kathrein, CO addition in low-pressure chemical vapour deposition of medium-temperature TiC_xN_{1-x} based hard coatings, Surf. Coat. Technol. 206 (2011) 1691–1697

[20] D. Hochauer, C. Mitterer, M. Penoy, C. Michotte, H.P. Martinz, M. Kathrein, Titanium doped CVD alumina coatings, Surf. Coat. Technol. 203 (2008) 350–356

[21] I.C. Noyan, J.B. Cohen, Residual Stress: Measurement by Diffraction and Interpretation, Springer, Berlin, 1987

[22] C. Riekel, M. Burghammer, R. Davies, Progress in micro- and nano-diffraction at the ESRF ID13 beamline, IOP Conf. Ser. Mater. Sci. Eng. 14 (2010) 012013

[23] A.P. Hammersley, S.O. Svensson, M. Hanfland, A.N. Fitch, D. Hausermann, Two-dimensional detector software: From real detector to idealised image or two-theta scan, High Press. Res. 14 (1996) 235–248

[24] M. Stefenelli, J. Todt, A. Riedl, W. Ecker, T. Müller, R. Daniel, M. Burghammer, J. Keckes, X-ray analysis of residual stress gradients in TiN coatings by a Laplace space approach and cross-sectional nanodiffraction: a critical comparison, J. Appl. Crystallogr. 46 (2013) 1378–1385

[25] J. Almer, U. Lienert, R.L. Peng, C. Schlauer, M. Odén, Strain and texture analysis of coatings using high-energy x-rays, J. Appl. Phys. 94 (2003) 697

[26] Landolt-Börnstein, Numerical Data and Functional Relationships in Science and Technology, Group III Vol. 11, Springer, Berlin, 1979

[27] E. Kröner, Berechnung der elastischen Konstanten des Vielkristalls aus den Konstanten des Einkristalls, Z. Phys. 151 (1958) 504–518

[28] C. Genzel, I.A. Denks, J. Gibmeier, M. Klaus, G. Wagener, The materials science synchrotron beamline EDDI for energy-dispersive diffraction analysis, Nucl. Instrum. Meth. A. 578 (2007) 23–33

[29] M. Klaus, W. Reimers, C. Genzel, Application of energy-dispersive diffraction to the analysis of highly inhomogeneous residual stress fields in thin film structures, Powder Diffr. 24 (2012) 82–86

[30] B. Eigenmann, E. Macherauch, Röntgenographische Untersuchung von Spannungszuständen in Werkstoffen, Materialwiss. Werkst. 27 (1996) 426–437

[31] DIN ISO 3369, Impermeable Sintered Metal Materials and Hardmetals - Determination of Density, Beuth, Berlin, 2010

[32] W. Lins, G. Kaindl, H. Peterlik, K. Kromp, A novel resonant beam technique to determine the elastic moduli in dependence on orientation and temperature up to 2000 °C, Rev. Sci. Instrum. 70 (1999) 3052–3058

[33] R.G. Munro, Evaluated Material Properties for a Sintered α-Alumina, J. Am. Ceram. Soc. 80 (1997) 1919–1928

[34] J. Kim, S. Kang, Elastic and thermo-physical properties of TiC, TiN, and their intermediate composition alloys using ab initio calculations, J. Alloys Compd. 528 (2012) 20–27

[35] T.-H. Fang, S.-R. Jian, D.-S. Chuu, Nanomechanical properties of TiC, TiN and TiCN thin films using scanning probe microscopy and nanoindentation, Appl. Surf. Sci. 228 (2004) 365–372

[36] W.C. Oliver, G.M. Pharr, An improved technique for determining hardness and elastic modulus using load and displacement sensing indentation experiments, J. Mater. Res. 7 (1992) 1564–1583

[37] K.-D. Bouzakis, N. Michailidis, G. Erkens, Thin hard coatings stress–strain curve determination through a FEM supported evaluation of nanoindentation test results, Surf. Coat. Technol. 142-144 (2001) 102–109

[38] M. Birkholz, P.F. Fewster, C. Genzel, Thin Film Analysis by X-Ray Scattering, Wiley-VCH, Weinheim, 2006

[39] B.D. Cullity, Elements of X-Ray Diffraction, Addison-Wesley, Menlo Park, 1956

[40] R. Allmann, A. Kern, Röntgenpulverdiffraktometrie: Rechnergestütze Auswertung, Phasenanalyse und Strukturbestimmung, Springer, Berlin Heidelberg, 2002

[41] L. Spiess, G. Teichert, R. Schwarzer, H. Behnken, C. Genzel, Moderne Röntgenbeugung: Röntgendiffraktometrie für Materialwissenschaftler, Physiker und Chemiker, Vieweg + Teubner, Wiesbaden, 2009

[42] S. Ruppi, Enhanced performance of α-Al_2O_3 coatings by control of crystal orientation, Surf. Coat. Technol. 202 (2008) 4257–4269

[43] K. Schiffner, C. Droste gen. Helling, Simulation of residual stresses by shot peening, Comput. Struct. 72 (1999) 329–340

[44] T. Kim, H. Lee, H.C. Hyun, S. Jung, A simple but effective FE model with plastic shot for evaluation of peening residual stress and its experimental validation, Mater. Sci. Eng. A 528 (2011) 5945–5954

[45] T. Hong, J.Y. Ooi, B. A. Shaw, A numerical study of the residual stress pattern from single shot impacting on a metallic component, Adv. Eng. Softw. 39 (2008) 743–756

[46] S.A. Meguid, G. Shagal, J.C. Stranart, J. Daly, Three-dimensional dynamic finite element analysis of shot-peening induced residual stresses, Finite Elem. Anal. Des. 31 (1999) 179–191

[47] W.K. Kubin, M. Pletz, W. Daves, S. Scheriau, A new roughness parameter to evaluate the near-surface deformation in dry rolling/sliding contact, Tribol. Int. 67 (2013) 132–139

Publication III

Advanced characterization methods for wear resistant hard coatings: A review on recent progress

Michael Tkadletz, Nina Schalk, Rostislav Daniel, Jozef Keckes, Christoph Czettl, Christian Mitterer

Invited review submitted to: Surface and Coatings Technology, July 2015

Advanced characterization methods for wear resistant hard coatings: A review on recent progress

Michael Tkadletz[1], Nina Schalk[2], Rostislav Daniel[2], Jozef Keckes[3], Christoph Czettl[4], Christian Mitterer[2]

[1]*Materials Center Leoben Forschung GmbH, Roseggerstraße 12, A-8700 Leoben, Austria*

[2]*Department of Physical Metallurgy and Materials Testing, Montanuniversität Leoben, Franz-Josef-Straße 18, A-8700 Leoben, Austria*

[3]*Department of Materials Physics, Montanuniversität Leoben, Jahnstraße 12, A-8700 Leoben, Austria*

[4]*CERATIZIT Austria GmbH, Metallwerk-Plansee-Straße 71, A-6600 Reutte, Austria*

Abstract

Due to economical demands to further increase the efficiency of production processes, it is essential to exploit the full potential of wear resistant hard coatings. This is, however, possible only if the coating microstructure and properties are well characterized. Thus, in the present work, recently suggested advanced characterization techniques for coatings are reviewed. The application of atom probe tomography, electron backscatter diffraction and synchrotron X-ray nanodiffraction enables previously unrevealed insights in their chemical composition, microstructure and crystallographic structure. For the determination of mechanical and tribological properties at elevated temperatures, high-temperature nanoindentation and high-temperature ball-on-disk tests in combination with *in-situ* measurement techniques are discussed. Utilization of micromechanical tests for coatings provides information about their fracture toughness and rupture strength. High-temperature X-ray diffraction and biaxial stress temperature measurements for the determination of the coefficient of thermal expansion are compared. The thermal conductivity as well as the specific heat capacity of coatings can be studied using the 3-ω technique, time domain thermoreflectance and differential scanning calorimetry. The introduced portfolio of characterization techniques enables the determination of a complementary microstructural, mechanical and thermo-physical fingerprint of wear resistant hard coatings, which allows to understand the complex structure-property relations in these materials and subsequently to further improve their performance.

Keywords: hard coatings; advanced characterization; thermo-physical properties; atom probe tomography; electron backscatter diffraction; nanodiffraction; high-temperature nanoindentation; time domain thermoreflectance; 3-ω technique; coefficient of thermal expansion; thermal conductivity; specific heat capacity

1. Introduction

Hard and wear resistant coatings are commonly deposited on tools which are used for severe cutting, forming and casting applications, where the conditions typically result in high temperatures, mechanical loads and pronounced wear [1–4]. Figs. 1a and b show scanning electron microscopy (SEM) images of a worn κ-Al_2O_3 coating, deposited by chemical vapor deposition (CVD), on a cemented carbide cutting insert at the end of its life time [5]. There, different effects which can be related to the severe operating conditions as well as to the high deposition temperatures can be observed. Distinct abrasive and diffusion wear is visible in Fig. 1a in the region where the highest temperatures during operation are present [6]. A focused ion beam (FIB) cross-section from the marked area at the edge of the wear crater was prepared for further investigations and is shown in more detail in Fig. 1b. Within the FIB cross-section, a thermal crack is visible which can be attributed to significant differences between the coefficient of thermal expansion (CTE) of coating and substrate material. The mismatch of the CTE´s results in high tensile residual stresses for the common CVD hard coatings on cemented carbide substrates, which have typically a significantly lower CTE than the coatings. Consequently, cracks during cooling after deposition are formed [7–9].

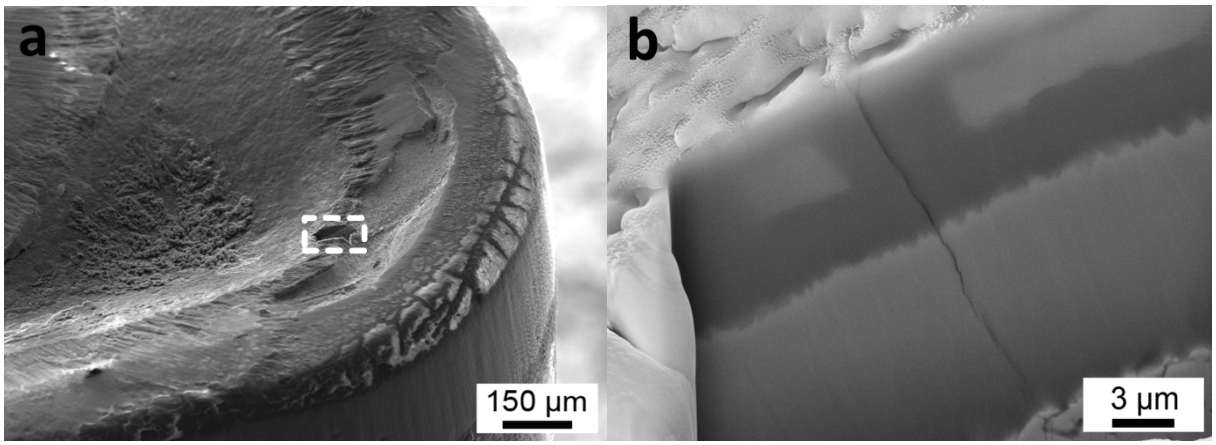

Fig. 1: *(a) SEM micrograph of a worn CVD κ-Al_2O_3 coating exhibiting pronounced crater wear after cutting a 42CrMo4 quenched and tempered steel. A FIB cross-section was prepared in the marked area. (b) Detail of the FIB cross-section, exhibiting a thermal crack developed during cooling due to the different CTE´s of coating and substrate [5].*

These degradation effects occurring during coating deposition and application highlight the importance to gain not only knowledge on the microstructure of the used coatings to be

able to tailor their design for the particular application, but also on a wide range of properties, including mechanical properties at elevated temperatures and thermo-physical properties. In the last decade, huge progress in advanced characterization techniques and methods available for coating characterization and testing has been achieved, which will be summarized within this review.

2. Chemical composition and microstructure

2.1 Chemical composition on the atomic scale

Common analytical methods applied as a characterization tool in the development of hard coatings such as energy- or wavelength-dispersive X-ray spectroscopy provide a limited local resolution; the analyzed volume is typically in the range of 1 μm^3 or slightly less. On the other hand, glow discharge optical emission spectroscopy, Auger electron and X-ray photoelectron spectroscopy as well as secondary electron mass spectroscopy offer the possibility of depth-resolved measurements, but again with only limited lateral resolution. These limitations have recently been overcome with the implementation of atom probe tomography (APT), which offers the possibility of chemical analysis on the atomic scale. In the early 1950´s Müller *et al.* [10] developed the field ion microscope (FIM), which enables the field ionization of noble gas atoms like He or Ne at a very sharp metal tip. The gas ions are subsequently accelerated towards a fluorescence screen where they are used for imaging and thus, represent the crystallographic arrangement of the atoms within the metal tip. The atom probe, introduced in the late 1970's represents a further improvement of the FIM, where the imaging ions originate directly from the sample tip [11]. With integration of time-of-flight mass spectrometry and position resolved channeling plate detectors, it is nowadays possible to determine the species and position of atoms or clusters within the sample on the atomic scale. The collected data allows to reconstruct the three-dimensional arrangement of the atoms within the sample; this method is referred to as three-dimensional atom probe tomography [12–16].

In order to evaporate ions from electrically conducting specimens by means of field evaporation, a high positive DC base-voltage of about 10 kV is applied to a sharp tip which is held at cryogenic temperatures, to prevent diffusion, under ultra-high vacuum (base pressure $<10^{-8}$ Pa). The typical tip radius of less than 100 nm results in a high electric field of approximately 10-40 V/nm at the apex [13,14]. Voltage pulses which are 10-20 % higher than the base-voltage with a frequency in the kHz range are applied to the tip, resulting in evaporation of the sample material [12]. In modern APT devices, instead of positively pulsing the sample tip, field evaporation is achieved by applying negative pulses on local counter

electrodes situated next to the specimen, which is referred to as local electrode atom probe [17]. A further development is the laser-pulsed APT [18], which induces sample evaporation by utilization of short (< 1 ns) intense laser pulses and the subsequent temperature increase. Using laser assisted evaporation makes APT also suitable for investigations on electrically non-conducting samples [18,19]. Modern systems are operated with evaporation/analysis rates in the range of 10^8 ions/h, which corresponds to an volume of about 8×10^6 nm^3 (i.e. about 4.8×10^8 atoms) or a sample size of $100\times100\times1000$ nm^3 investigated within 1 h [15]. The atomic resolution of APT and the restriction to very small sample volumes make it interesting for coatings and thin films, which recently can be prepared with a small volume and site-specific by precise high-performance FIB workstations [20–22]. An example for FIB assisted preparation of an atom probe specimen cut out of a thin film sample is shown in Figs. 2a to c. After choosing an area of interest, two opposite wedges are cut into the sample in order to prepare a lamella (Fig. 2a), which is subsequently attached to a micromanipulator and cut free at both sides and the bottom. The lamella is then transferred (Fig. 2b) and attached to a pre-assembled sample holder (e.g. a Si tip) and detached from the micromanipulator. The final preparation step is annular FIB milling and polishing of the sample to sharpen the tip until the desired tip radius is reached (Fig. 2c).

Recently, topics related to the thermal stability of TiAlN based coatings [21,23–26], as well as fluctuations and distributions of the elemental and phase composition in general [27,28] are subject to intensified investigations. An APT reconstruction of a TiAlN coating annealed at 1350 °C is shown in Fig. 2d. Annealing of a metastable cubic (c) TiAlN solid solution results in spinodal decomposition into c-TiN and c-AlN and subsequent phase transformation of c-AlN into wurtzitic (w) AlN [29]. Due to the spinodal decomposition, Ti- and Al-enriched domains are formed within the sample, which can be clearly recognized in the Al and Ti distribution and the combined concentration reconstruction shown in Fig. 2d [21,26,30]. The excellent resolution of APT has also been demonstrated by determining diffusion lengths of a few nanometers of Cu in TiN barrier coatings and Cu in Si and vice versa [31,32].

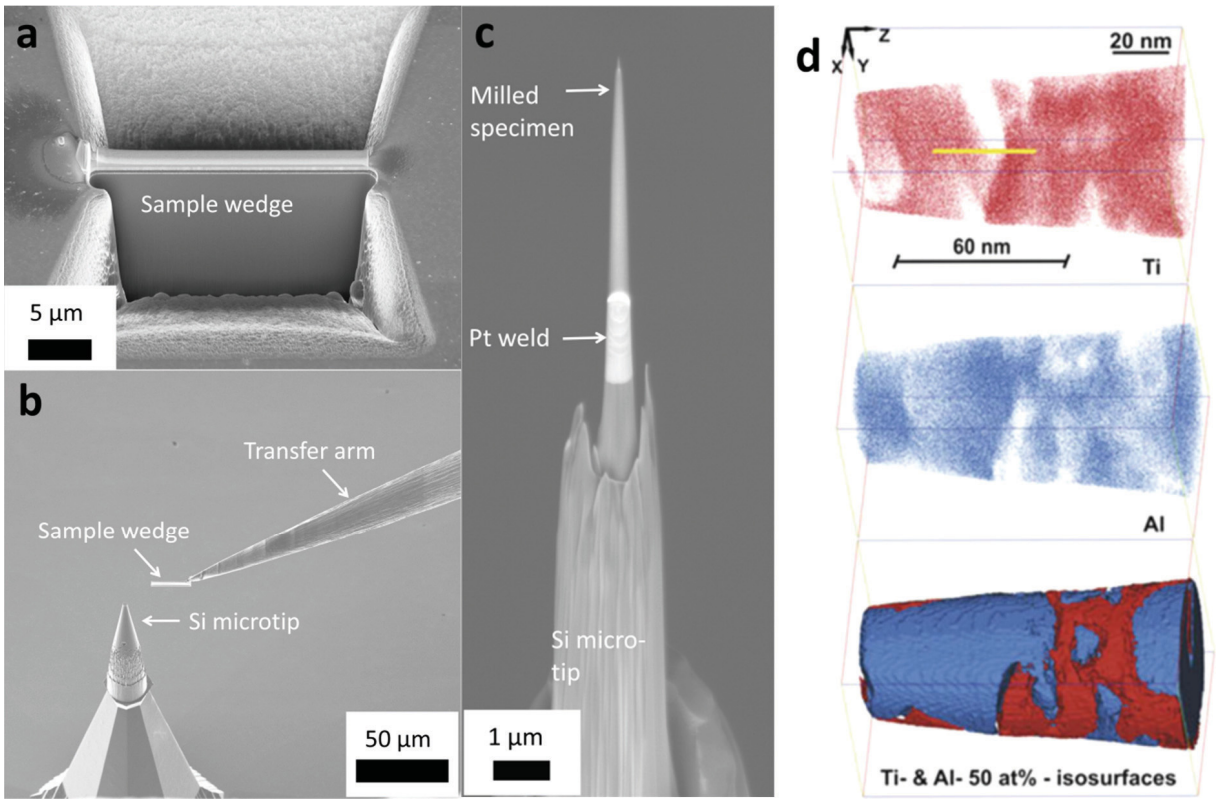

Fig. 2: *Preparation procedure of a hard coating specimen for APT. (a) FIB fabrication of a freestanding wedge of the area of interest. (b) Transfer of the wedge to a Si micro-tip using a micromanipulator. (c) FIB milling to the final shape, exhibiting a tip radius of a few nm. (d) 3D reconstruction of a measurement on a sputtered TiAlN coating annealed at 1350 °C, indicating formation of Al and Ti rich domains [26].*

2.2 Microstructure on the nanometer scale

2.2.1 Microstructure characterization using electron backscatter diffraction

Electron backscatter diffraction (EBSD) has become a standard characterization method for bulk materials in the last two decades [33,34]. Detectors are commercially available and the analysis using software, provided by manufacturers, is nowadays fully automated. That makes EBSD a powerful tool for crystal orientation mapping, phase imaging, determination of grain size distributions and strain analysis [35–40].

Prior to a measurement, the sample has usually to be polished to guarantee a smooth surface resulting in satisfying signal quality. This can either be done by mechanical or ion polishing (e.g. using a FIB) [39,41]. Subsequently the polished sample is aligned on the sample stage of a SEM and tilted to an angle of 60-70° with respect to the horizontal [35,39,40]. After alignment, the sample can be either scanned by movement of the stage or the electron beam itself [35]. The EBSD patterns are usually collected using a phosphor

screen and a charge-coupled device (CCD) camera [35,39]; the typical depth of information is ~50 nm below the sample surface [37,40]. EBSD patterns consist of so called Kikuchi bands [39,42], which are commonly automatically Hough transformed by the software for easier data treatment [43]. Crystallographic planes and zone axes are indexed by the software and the orientation of different grains can be determined and displayed [39]. The speed of data acquisition of modern systems is in the range of almost thousand data points per second, which allows to perform measurements with high resolution in reasonable time [39,44]. Humphreys and Randle [35,41] propose to probe at least 200 grains to obtain a representative result of the microstructure of the sample, thereby, each grain should exhibit at least ~10 points across and a total number of ~100 points per grain. The lateral resolution is mainly determined by the diameter and the energy of the electron beam, which is used to probe the sample, and by the backscatter coefficient of the sample which is given by its atomic number [45–47]. Using modern EBSD systems, operated in a field emission gun (FEG) SEM, enables to determine single grains as small as 20 nm in diameter [48–50]. A further improvement of EBSD is the so-called image quality analysis, for which the intensity, contrast, sharpness and noise level of the Kikuchi bands is investigated as well. Thereby, the contribution of topographic effects and grain boundaries can be considered, which results in a far more descriptive micrograph of the measurement [51]. To get an insight into the volume of the sample material, an interesting possibility is to combine FIB cut-and-slice techniques and EBSD measurements, which enables to calculate a three-dimensional reconstruction of the investigated volume, as for example recently shown for ceramic materials [52,53].

The high spatial resolution combined with FIB sample preparation techniques results in increasing interest in EBSD measurements within the hard coatings community to obtain information about orientation, texture and evolution of grain size and shape with respect to film thickness [54–58]. An EBSD measurement on a FIB cross-section of a CVD α-Al_2O_3/TiCN bilayer coating deposited on a cemented carbide cutting insert [59] is shown in Fig. 3. There, the SEM image acquired with an energy-selective detector for backscattered electrons within a FEG-SEM is superimposed with an image quality orientation map EBSD measurement. Differently oriented grains appear in different colors, thus, neighboring grains can be distinguished, providing insight into the microstructure of the investigated sample. Next to the interface with the substrate, the TiCN layer exhibits a fine grained nucleation zone followed by a dense columnar structure. The α-Al_2O_3 top layer shows a less fine grained nucleation zone near the TiCN/α-Al_2O_3 interface, followed by almost equiaxed rather big grains towards the sample surface.

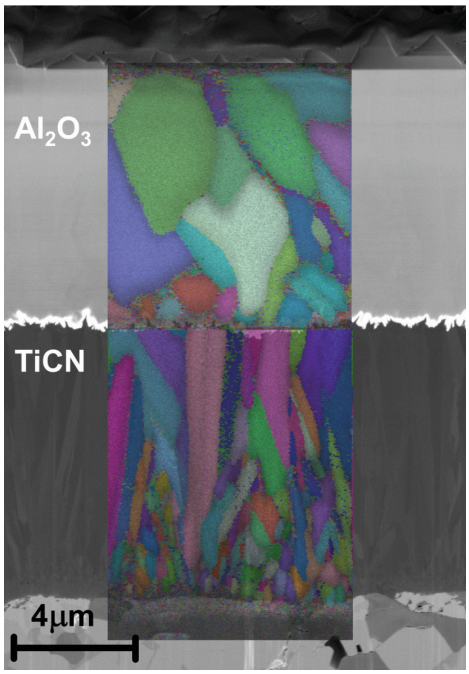

Fig. 3: *SEM micrograph of a cross-section of a CVD α-Al_2O_3/TiCN hard coating superimposed by an EBSD image quality measurement [59].*

2.2.2 Microstructure characterization using synchrotron X-ray nanodiffraction

Typically, the term nanodiffraction is used in relation with transmission electron microscopy, where 2D electron diffraction patterns can be collected with nanometer resolution from different sample positions applying either parallel or convergent electron beams [60–62]. For X-ray diffraction (XRD), the term nanodiffraction is related to the use of X-ray beam diameters of 100 nm or less. Using such small beam sizes in reflection geometry, a high spatial resolution across the surface as well as depth-resolved information has can be gained using monochromatic and polychromatic X-ray beams, respectively [63–66].

Recently, a combination of transmission diffraction geometry and a highly focused monochromatic X-ray beam provided by a synchrotron source has been introduced to analyze depth-dependent microstructure of hard coatings, which is referred to as cross-sectional synchrotron X-ray nanodiffraction [67,68]. There, a lamella of the sample with a thickness in the range of 20-400 µm, depending on the energy of the used X-ray beam, required diffraction statistics and tolerable, unavoidable residual stress relaxation effects has to be prepared [68,69]. The lamella is scanned in transmission geometry along the coating thickness and Debye-Scherrer rings are recorded stepwise with a resolution of 100 nm or even less, depending on the available beam size [68]. The collected data of an extensive volume requires comprehensive treatment performed for example using the software packages Fit2D [70] or PyFAI [71,72]. Utilizing this technique, phase information, microstructural data such as grain size and crystallographic texture, as well as elastic strain

and stress, provided X-ray elastic constants for the materials of interest are known, can be extracted as a function of the coating thickness [73–77].

Phase evolution and strain analysis as a function of the coating thickness of a nanocrystalline sputtered CrN coating measured with a point-focused nanobeam of 100 nm in diameter is shown in Fig. 4a [68]. During deposition, the bias voltage was changed from -40 to -120 V in the mid-section of the coating. This results in increased residual strain, which is evidenced by the pronounced shifts of the in-plane (δ=0°) CrN 111 and 200 reflections towards higher diffraction angles. However, one drawback of this technique is that when it comes to beam sizes below 100 nm and/or if rather coarse grained materials are investigated, the diffraction statistics might become insufficient. In Fig. 4b, an example of a very spotty diffraction pattern obtained during a nanodiffraction experiment on a coarse grained CVD α-Al_2O_3 coating with crystallite size in the µm range, performed using a point focus X-ray beam of 100 nm in diameter is presented. Recently, approaches to overcome this experimental drawback have been published, which are based on the utilization of pencil-shaped focused nanobeams with dimensions down to 50 nm in height and 15-50 µm in width. Those provide considerably improved diffraction statistics, while the spatial resolution over the film thickness is kept high, if the coating surface is correctly aligned to the pencil-shaped beam [59,69]. This significant improvement of diffraction statistics is demonstrated in Fig. 4c, where the same CVD α-Al_2O_3 coating as in Fig. 4b was measured using a pencil-shaped beam, resulting in a diffraction pattern with fully developed Debye-Scherrer rings. The results of nanodiffraction measurements of a post-deposition dry-blasted CVD α-Al_2O_3 coating with a TiCN base-layer are shown in Fig. 4d. Both layers can be clearly distinguished in the in-plane phase depth-profile as portions of the coating characterized by diffraction peaks of different crystallographic structures (note cubic and trigonal structure of TiCN and α-Al_2O_3, respectively). A pronounced in-plane peak shift towards higher diffraction angles in the surface near region of the α-Al_2O_3 layer is related to in-plane compressive stress introduced by the blasting treatment, where the resulting depth-profile is shown on the right hand side of Fig. 4d.

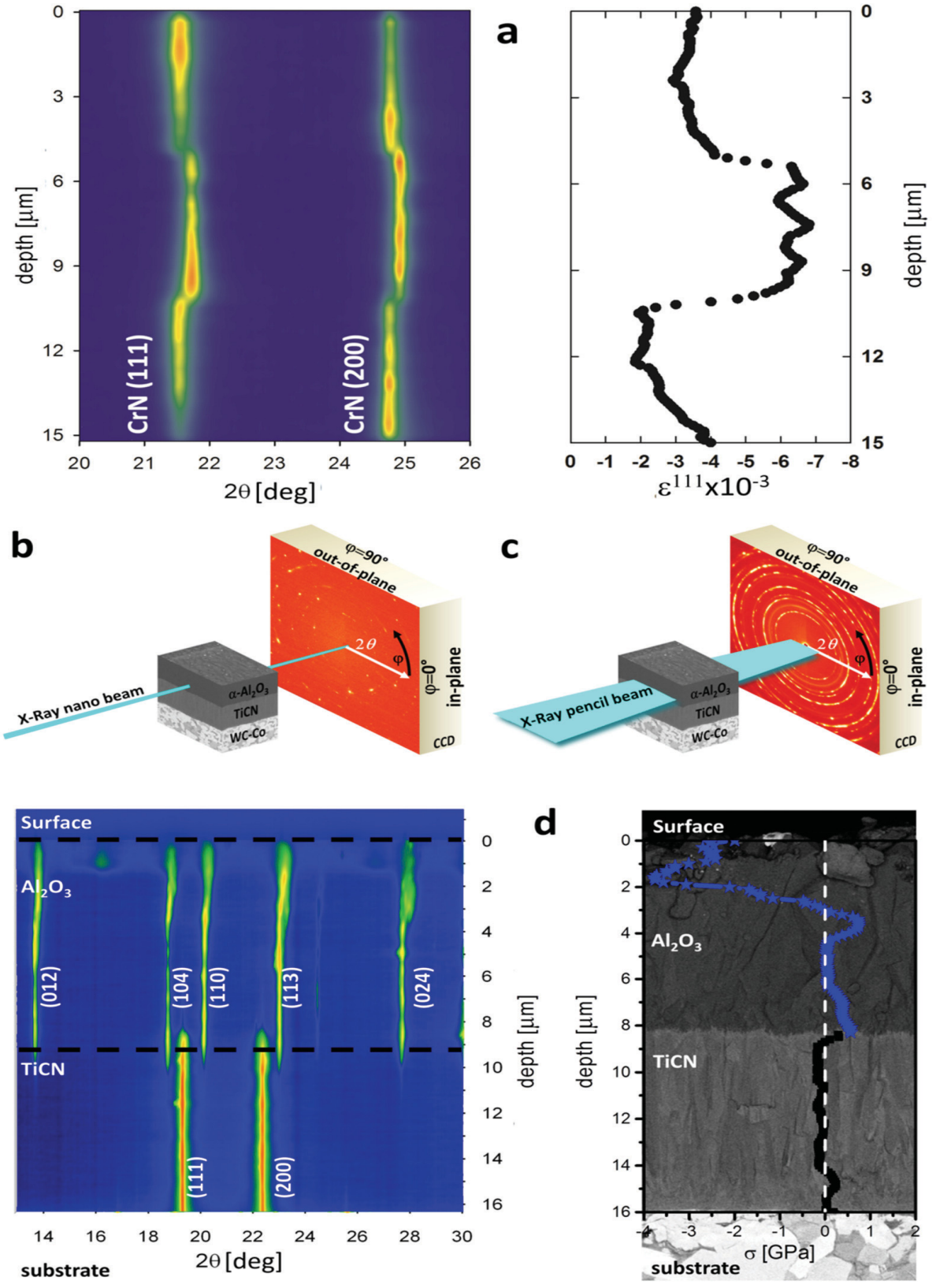

Fig. 4: *(a) In-plane phase and strain analysis of a 15 µm thick sputtered CrN hard coating deposited with varying bias voltage [68]. Schematic of a nanodiffraction experiment using (b) a point focussed X-ray beam and (c) a pencil shaped X-ray beam. (d) In-plane phase and strain/stress analysis of a coarse grained, post-treated CVD α-Al_2O_3/TiCN hard coating [59].*

3. Mechanical and tribological properties

3.1 High-temperature hardness and Young´s modulus

In the last two decades, nanoindentation has become a standard technique for determination of hardness and elastic properties of hard coatings [78–80], providing basic information about their suitability for cutting applications [81,82]. However, since high temperatures occur at the cutting edge during severe cutting applications [6], the temperature dependence of hardness and Young's modulus has gained increasing interest [83–85]. With ongoing development of nanoindentation systems, nowadays devices are available which facilitate indentation testing up to 700 °C or even higher temperatures [83,86–88].

To successfully perform nanoindentation experiments at elevated temperatures, several basic principles need to be considered. First of all, it is necessary to protect the sample as well as the indenter tip from oxidation, which is usually achieved by using an experimental setup allowing experiments in inert gas or under high vacuum [87,89,90]. Furthermore, special attention has to be paid to the used indenter material. At room temperature, diamond indenters are usually favored due to their high hardness and stiffness [91]. However, at elevated temperatures residual oxygen in the system might lead to oxidation and increased chemical wear of a diamond indenter. Thus, the use of chemically stable, oxidation resistant indenter materials such as cubic boron nitride (c-BN) or boron carbide, which both still exhibit a reasonable hardness and stiffness, is favorable [91]. Moreover, the mechanical properties of diamond are significantly affected by temperature, while boron carbide exhibits a high stability of its mechanical properties at elevated temperatures [91]. Independently from the chosen tip material, accelerated tip deterioration can be expected due to decreased hardness of the indenter material at elevated temperatures and possible chemical (i.e. oxidational) and diffusional wear. Consequently, the tip shape has to be monitored constantly by determination of the actual area function of the tip, to consider the deviation of the real indenter shape from the ideal geometry [86]. This is usually realized by a reference measurement on a material with well-known mechanical properties like fused silica or sapphire. In a recently reported approach, an area function of the used tip is determined before and after each set of measurements [85]. The area function determined before the measurement is then used for the evaluation of the initial half of the indents and the area function determined after the measurement is used for the evaluation of the second half of the indents within the measurement to minimize the effect of a continuous tip rounding during the experiment.

Aiming for stable operating conditions to obtain reproducible results, several fundamental steps need to be considered. Thermal equilibration of the system after heating to the desired testing temperature is a crucial factor; thus, typically a waiting period of at least one hour with the tip close to the surface (< 20 µm) is applied [85,87]. After that first step of equilibration, a second thermal compensation step before each indentation, with the tip at the surface (i.e. at a distance of 0-2 µm) should be performed for several minutes [85]. Further reduction of the heat flow between indenter and sample can be achieved by actively heating both the tip and the sample [87]. To avoid creep effects which may occur during unloading, a holding period at maximum load in the range of 10 to 60 s should be performed to allow the system to stabilize [85,87,92,93]. Additionally, the unloading time can be reduced which results in a lower absolute creep value during unloading [85]. To collect data for thermal drift correction, a holding period of > 60 s at 80-90 % of the unloading curve is typically applied, where the first third of the collected data should be skipped since it might be affected by relaxation effects [85,92–94]. Considering these basic principles, it is possible to perform nanoindentation experiments at elevated temperature with drift rates of several tenths of a nm per second [86,87,89,90].

High-temperature data for hardness and Young´s modulus of hard coatings have been reported for physical vapor deposited (PVD) coatings based on TiAlN [83,95–97], AlN/CrN [84] and TiAlCrSiYN [92,93,98]. An example of a high-temperature nanoindentation measurement for a CVD α-Al_2O_3 coating, published by Rebelo de Figueiredo *et al.*, is shown in Fig. 5 [85]. The measurement was performed in inert gas atmosphere up to a temperature of 600 °C, using a c-BN indenter and considering the above mentioned strategies to obtain ideal operating conditions. For comparison, an additional test with a diamond indenter was performed at room temperature. The tests at elevated temperatures indicate no significant change of the reduced Young´s modulus up to 500 °C, while the hardness decreases by about one third of its initial value of 24 GPa at room temperature to 16 GPa at 500 °C. At 600 °C, a slight increase of the reduced Young´s modulus and hardness can be observed, which both might be related to oxidation of the cemented carbide substrate due to residual oxygen within the system. The pronounced scattering at this temperature is assumed to be a result of the increasing surface roughness due to the oxidation.

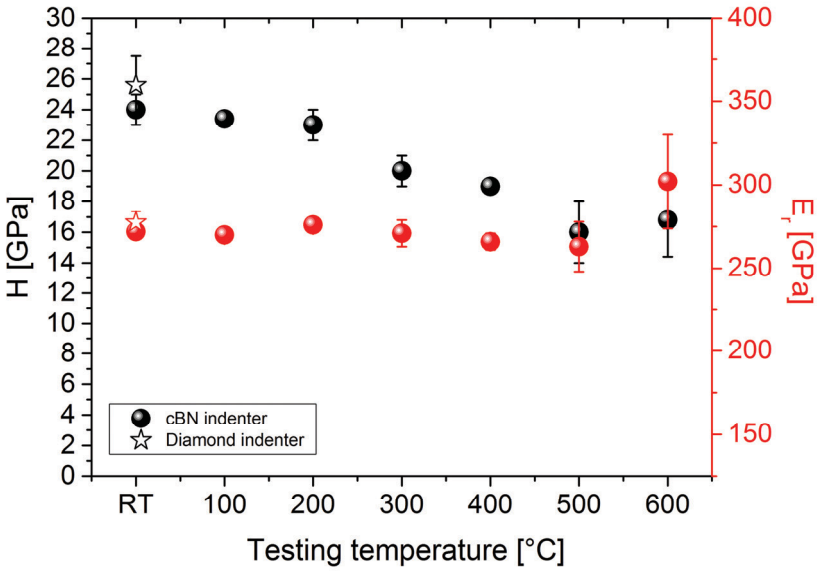

Fig. 5: *Hardness and reduced Young´s modulus of a CVD α-Al_2O_3 hard coating as a function of temperature determined by high-temperature nanoindentation [85].*

3.2 Fracture stress and fracture toughness

The fracture behavior and the determination of the stress intensity factor K_{IC}, which is commonly referred to as fracture toughness, allows differentiation between brittle and ductile materials. Besides the hardness, which represents the resistance of a material to plastic deformation, also the toughness, denoting the resistance to crack propagation or the energy consumption during fracture, is essential for the performance of hard coatings in service [99]. Hard coatings which are still ductile would have the benefit of retarded crack initiation and propagation in addition to high wear resistance. Emerging plastic deformation would dissipate energy resulting in a prolonged lifetime of the tool [99]. Besides conventional techniques for fracture toughness measurements, e.g. compact tension or three-point bending tests [100], strategies to determine the fracture toughness of bulk materials using indentation techniques have been applied for decades [101–103]. Due to achieved establishment of nanoindentation for the characterization of hard coatings, the strategies applied for bulk materials have been adapted to determine the fracture toughness of hard coatings from cracks introduced into the coating by nanoindentation [104–108]. Methods based on the examination of the introduced radial cracks, providing crack length and maximum applied load, have been used as well as energy based methods which utilize circumferential cracking and evaluation of the load-displacement curve to derive the fracture toughness [104,105,109]. Recently, a method has been suggested, which utilizes indentation into a partially coated substrate to determine the fracture toughness of hard coatings [110–112]. In this approach, an impression is made on an uncoated area of the

substrate at a high load by a Vickers indenter to induce cracks, which subsequently propagate into the coated area of the substrate. The difference of the crack lengths in both coated and uncoated areas allows the determination of the fracture toughness of the coating if the fracture toughness of the substrate is known. However, the knowledge of the particular crack geometries is crucial for such techniques and their determination is rather complex, which results in an unpredictable inaccuracy of the mentioned techniques making them still controversial [109].

Modern FIB workstations and the possibility to operate a nanoindentation system in a SEM facilitate fabrication and subsequently, recorded deformation of samples like pillars and cantilevers on the µm scale. Thus, the stress-strain data and fracture behavior of thin films and hard coatings can be determined, as reported for metals and nitrides, yielding their Young´s modulus, yield and fracture strength as well as their fracture toughness [113–120]. Riedl *et al.* [119] presented an approach which combines chemical etching techniques and FIB sample preparation in order to minimize the preparation influence on the obtained mechanical properties. In this approach, surfaces of coatings with a typical thickness of approximately 3 µm deposited on Si (100) strips are scratched in selected areas using a diamond tip, in order to enable interaction of the etching agent with the underlying substrate. Subsequently, the sample is etched for 1 h in a potassium hydroxide (30 wt.%) aqueous solution at 60 °C. After etching, the sample is cleaned in distilled water and ethanol. Due to the chemical inertness of the coating and selective etching of the Si substrate, a freestanding area of the coating, well adhering to the remaining substrate is obtained. Cantilevers of the freestanding coating can be fabricated in this way using a FIB without introducing any ion damage into the surface or the interface, accepting the coating thickness as cantilever height. Micromechanical testing of such cantilevers enables the determination of the Young´s modulus and fracture stress of the coating. Further, it is possible to evaluate the fracture toughness of the coating by testing cantilevers with a pre-assembled notch.

A SEM micrograph of two cantilevers, notched and without a notch, is shown in Fig. 6a. The cantilevers with a length of 10x2 µm² were prepared from a single-layer Cr coating, with a height of 3 µm corresponding to the coating thickness. The results of micromechanical tests of cantilevers without a notch, prepared from sputtered single-layer Cr and CrN and a Cr/CrN multilayer, are shown in Fig. 6b. The load displacement curves indicate significant differences concerning the Young´s modulus and fracture stress between the single-layer Cr and CrN coating. In addition, it can be observed that the multilayer coating exhibits a strong increase of the Young´s modulus, fracture stress and fracture toughness (determined from notched cantilevers) compared to the single-layer coatings [121].

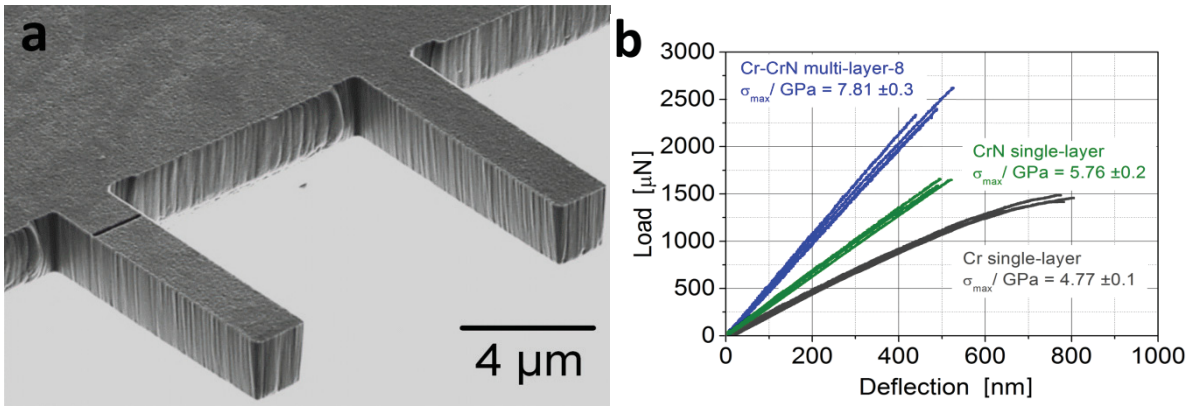

Fig. 6: *(a) Micro-cantilevers with and without notch prepared for fracture toughness and fracture stress measurements. (b) Load-deflection curves obtained by micromechanical tests performed on sputtered single- and multilayered Cr/CrN coatings with different sublayer thickness [121].*

3.3 Friction and wear

The reduction of friction is of vital importance for severe cutting applications, as friction is one of the main factors providing heat at the cutting edge during machining. Further, it determines the magnitude of the forces which are needed for chipping [122–124]. Besides cutting, friction is also of importance in forming applications like deep-drawing and extrusion and for low-friction coatings used e.g. in automotive applications. The term friction is related to the tangential force between two bodies, which move relative to each other while they are in contact, and is controlled by three basic mechanisms; adhesion, ploughing and asperity deformation [125]. As a measure of quantification, the coefficient of friction, representing the ratio of the tangential (i.e. frictional) to the normal force is well accepted [125]. For tools, there is also a demand to minimize wear, which is the removal of material during the contact of two bodies in relative movement to each other, caused by adhesion, abrasion, surface fatigue and chemical reactions [125]. Commonly, it is quantified by the wear rate which is the removed volume divided by the product of the normal load and the sliding distance [125]. Some authors might refer in this case to the wear coefficient which is controversial, and might lead to misunderstanding, as the term wear coefficient is usually referred to a dimensionless constant within the Archard equation [126,127]. Friction and wear can be seen as the often interlinked output of a given tribological system, where the mechanisms determining both suggest different approaches to improve them. To reduce the use of coolants and lubricants during machining and nevertheless improve the performance of cutting tools, two different basic approaches are typically applied. The first one is to utilize hard, wear resistant coatings, usually based on nitrides, carbides, borides and oxides [128]. The other one is to use low friction coatings such as diamond-like carbon [128–135] or MoS_2

[136,137]. These approaches might be combined as well, either by depositing layered structures [138], co-deposition [137,139–143] or by formation of nanocomposites [144–146]. The available large spectrum of materials and coating architectures enables to tailor the friction coefficient in a wide range.

In order to determine the tribological properties such as coefficient of friction and wear rate, a number of different characterization techniques ranging from rather simple ball- or pin-on-disk tests [122,147–149] to highly sophisticated tests which are close to real applications [150,151] can be used. However, due to the increasing complexity of approaches to improve the tribological behavior, also the characterization of tribological contacts is increasingly challenging, in particular to benefit from tribo-chemical reactions in the sliding contact to achieve a self-adaptive behavior. Thus, Raman spectroscopy, energy dispersive X-ray spectroscopy (EDX) and X-ray photoelectron spectroscopy (XPS) have become important tools to determine surface reactions within tribological contacts. For example, Schalk *et al.* [152] investigated different carbon species formed within the wear track surfaces during ball-on-disk tests, responsible for the observed low friction coefficient of their TiAlN-based coatings after post-treatment by annealing in methane, using Raman spectroscopy. Jantschner *et al.* [153] used XPS to examine different Si compounds in wear tracks of Si containing amorphous carbon films after performing ball-on-disk tests. Nohava *et al.* [154] investigated wear tracks utilizing SEM-EDX mapping on both, the surface and in cross-sections prepared by FIB within the wear tracks after ball-on-disk testing of wear resistant nitride, oxynitride and oxide coatings at different temperatures. A friction reduction of CVD α-Al_2O_3 during ball-on-disk testing at 900 °C caused by out-diffusion of rutile TiO_2 from a TiCN sub-layer through the thermal crack network was found by Schalk *et al.* [155] utilizing SEM investigations and EDX measurements. SEM micrographs of the pristine surface and a FIB cross-section within the corresponding wear track are shown in Figs. 7a and b, respectively. The crack network is clearly visible in the SEM micrograph and the rutile formation can be recognized as bright deposit on top of the coating surface (Fig. 7a) and within the crack (Fig. 7b). Tkadletz *et al.* [156] investigated the role of droplets, typically generated during cathodic arc evaporation, on the wear behavior of TiAlTaN hard coatings. A SEM micrograph superimposed by an EDX map of a FIB cross-section of a droplet prepared from the as-deposited coating, revealing its microstructure and chemical composition, is given in Fig. 7c. The response of a droplet to a ball-on-disk test at room temperature is shown in Fig. 7d. Cracks initiated at the droplet can be clearly seen, indicating that droplets promote coating degradation during sliding contact. The combination of EDX measurements, FIB milling of thin slices and subsequent digital gray-scale correlation of the SEM micrographs enables to reconstruct a three-dimensional map of the microstructure and

chemical composition of a large sample volume. An example is shown in Fig. 7e for a droplet embedded in a coating corresponding to the situation presented in Fig. 7d. The resolution is mainly depending on the thickness of the milled slices, which can be in the range of several nm. In this case, the slice thickness was 88.5 nm and the investigated volume was $18\times15\times10$ µm³. Orange, green and yellow areas represent the cemented carbide substrate, while the transparent bluish region represents the coating. Non-transparent blue color indicates Ti, corresponding to the investigated metallic droplets. The reddish network stems from cracks surrounding the droplets, which were formed during the ball-on-disk test, corroborating the assumption that droplets promote defect formation in dry sliding contacts. This example demonstrates the feasibility of the combination of FIB milling, EDX-mapping and digital image processing, in investigating microstructural and chemical features in hard coatings.

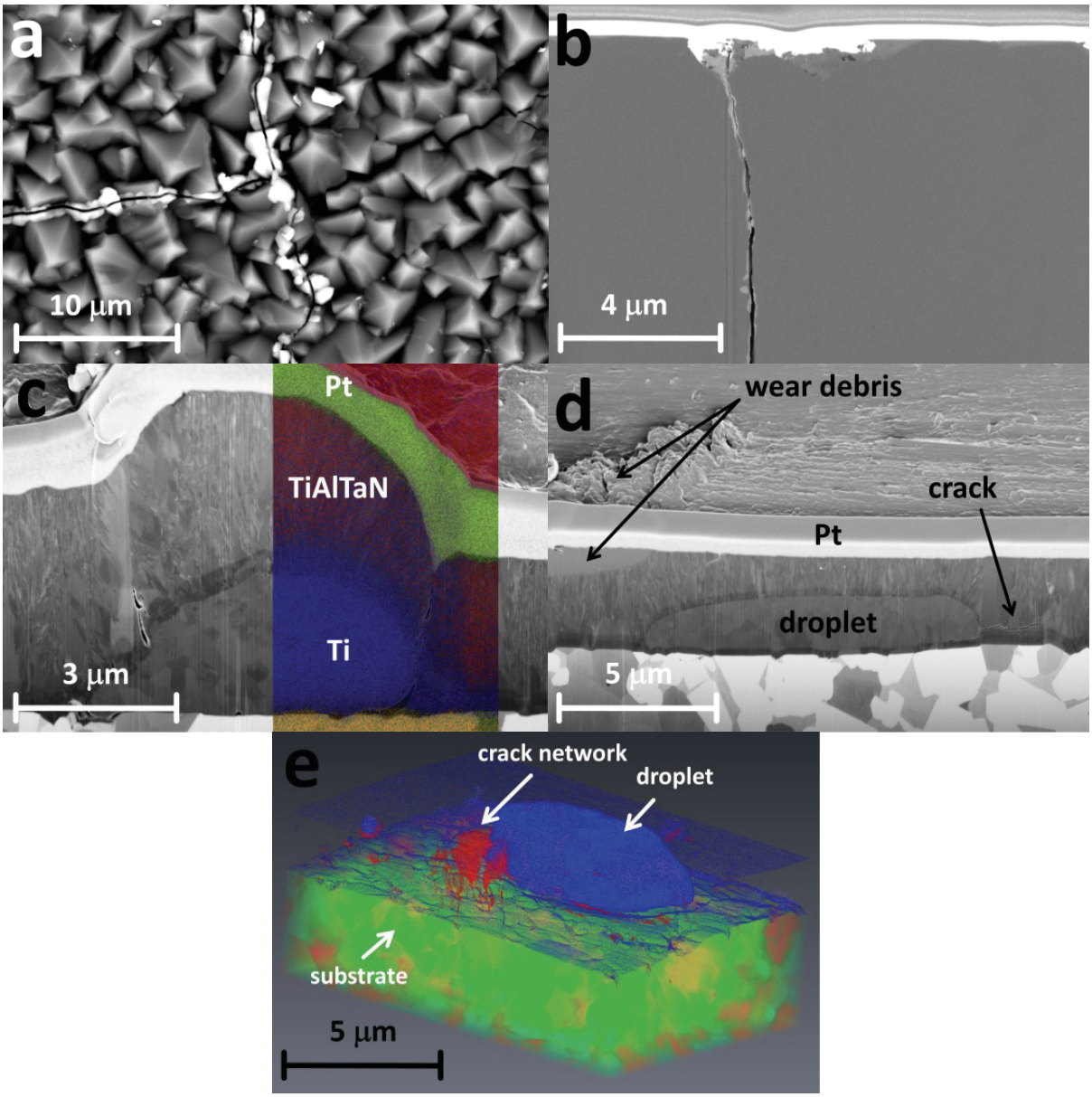

Fig. 7: *SEM micrographs of (a) the surface of a CVD α-Al_2O_3 hard coating after ball-on-disk testing at 700 °C, showing thermal cracks surrounded by out-diffused rutile, (b) a FIB cross-section through a thermal crack filled with rutile [155], (c) a droplet within an arc-evaporated TiAlN coating before ball-on-disk testing, superimposed by an EDX map, (d) a droplet after a ball-on-disk at room temperature [156]. (e) 3D reconstruction of a droplet within a wear track after testing at room temperature, showing the microstructure and formation of cracks due to the mechanical loads.*

The above mentioned techniques are based on *ex-situ* investigations of the wear tracks, while recently approaches expanding to *in-situ* studies of self-adaptive coatings using, e.g. light optical microscopy or Raman spectroscopy, have been suggested [157–160]. Furthermore, the potential of such *in-situ* investigations has been demonstrated for so-called adaptive chameleon coatings, showing reproducible variations of their coefficient of friction with changing atmosphere or temperature [153,161]. Those examples clearly illustrate that recent advanced characterization techniques and their combination help to further advance topics, which already have been subject of research for decades.

4. Thermo-physical Properties

4.1 Thermal expansion

The mismatch of the CTE´s of coating and substrate gives rise to the development of thermal stress in coatings synthesized at elevated temperatures. It can provide a major contribution to the total residual stress, being the sum of thermal, intrinsic and extrinsic components [162]. Several reports describe the positive and negative effects of residual stresses on the performance of wear resistant hard coatings. Increasing compressive stresses are frequently reported to correlate with increasing hardness [163], whereas tensile stresses can be related to decreasing hardness and formation of thermal crack networks within CVD [7–9] and PVD coatings [164]. CTE values for hard coatings are rarely found in literature and frequently bulk values are used to explain the observed results. However, there are studies which indicate that the CTE of hard coatings strongly depends on coating thickness and microstructure (i.e. grain size) [162,165] as well as on the chemical composition [164]. There, the determined values are reported to be either higher [165] or lower [166] than literature values for bulk materials. Post-deposition annealing treatments (resulting in a change of the grain size) have also been reported to change the CTE significantly [165]. In general, the thermal expansion of solids is determined by their potential energy curve, showing an asymmetric shape [167]. Moreover, the CTE is a temperature-dependent material property, which necessitates to distinguish between the mean CTE, i.e. an averaged value over a certain temperature range (which is in many cases not mentioned), and the absolute CTE, given either by a specific value for a certain temperature or by a function of temperature [168,169].

For the in-depth understanding of coating stresses, the high variance of CTE literature values suggests to determine precise values for hard coatings, taking into account their chemical composition, microstructure and thickness. A well-established procedure to determine the CTE is the wafer curvature method applying the modified Stoney equation [170,171], where the curvature of a single-side coated substrate (e.g. Si strips or wafers) is determined by the

deflection of two or more parallel laser beams. Due to the residual stress of the coating, the substrate exhibits an initial curvature after deposition, which is proportional to the magnitude of the total residual stress. With the assumption, that during heating or cooling all other contributions to the residual stress, except the thermal stress, are constant as long as the deposition temperature is not exceeded, the variation of the substrate curvature (i.e. the thermal stress) only depends on the CTE of the coating. If the biaxial modulus (in the ideal case) or the Young´s modulus (as a simplification due to a lack of data) and the Poisson´s ratio of the coating as well as the mean CTE of the substrate are known, the mean CTE of the coating can be determined [165]. Sample heating should ideally be done under vacuum or in inert gas to prevent oxidation, which enables to determine the residual stress of the coating as a function of temperature and, subsequently, the mean CTE can be calculated for the chosen temperature range. This procedure is frequently referred to as biaxial stress temperature measurement (BSTM) [172]. The main benefit of this method is that it can be applied for both, crystalline and amorphous coatings. However, there are also some limitations; since single-side coated substrates are required, the method is hardly applicable for CVD coatings. Further, if exposed to higher temperatures, during deposition or measurement, the commonly used Si might deform plastically which results in errors in the evaluation [173]. Besides that, it has to be noted that the mechanical properties of the coating and the substrate itself as well as the CTE of the substrate are temperature dependent. Therefore, the common assumption that the substrate´s biaxial modulus and CTE, the coating´s Young´s modulus and its Poisson's ratio are constant with increasing temperature could increase the error of the measurement significantly.

Another method which is frequently employed to measure the CTE of crystalline materials [174–178] is based on high-temperature X-ray powder diffraction, where the lattice parameter as a function of temperature can be accurately determined without any knowledge of other properties of the material. Although rarely used for hard coatings, there are reports where this method has been successfully applied [168,169]. In order to perform such a measurement on a coating, first of all, the coating needs to be powdered. This can be achieved by depositing the coating on a soluble substrate like rock salt or iron foil. Subsequently, the substrate is chemically removed using a suitable solvent, where reactions with the coating material itself must be avoided. For iron foil this can either be nitric or hydrochloric acid, where the choice depends on the particular coating material as some coatings might be soluble either by the one or the other. After the substrate is removed, the remaining coating should be purged with, e.g. acetone and ethanol, in order to remove organic impurities. Finally, it is dried and ground with a mortar to obtain a fine grained uniform powder. After this procedure, the powdered hard coating sample can be

investigated by XRD at elevated temperatures. If the sample is sensitive to oxidation, operation under vacuum or inert gas is strongly recommended.

The absolute change of the lattice constants of sputter deposited and subsequently powdered TiN, TiAlN and AlN coatings up to 700 °C, derived from high-temperature XRD measurements in steps of 50 °C, are shown in Fig. 8a. The lattice parameters of the investigated samples were calculated applying Rietveld refinement [179] of the collected X-ray diffractograms. The non-linear development of the lattice constant with increasing temperature reflects the shape of the potential energy curve of the given material. For data processing, the measured values can be fitted using, e.g. a parabolic function, and subsequently, the CTE can be calculated as a function of temperature (Fig. 8b). Yim *et al.* reported on a reasonable agreement between a linear approximation and a parabolic function for the calculation of the mean CTE in the range from 20 to 800 °C, both derived from the same high-temperature XRD measurements on AlN, sapphire and Si samples [168]. The linearly fitted data presented in Fig. 8a up to 400 °C were used to determine mean CTE´s, which were subsequently compared to the mean CTE´s derived from BSTM measurements, performed in the same temperature range. In order to obtain a directionally averaged CTE for the w-AlN phase present in the sputtered AlN coating, the values of the *a* and *c* axis were averaged according to Ref. [174]. The XRD measurements revealed mean CTE values of 4.41×10^{-6}, 2.74×10^{-6} and 4.65×10^{-6} K^{-1} for TiN, AlN and TiAlN, respectively. In comparison, the values of 5.17×10^{-6}, 3.76×10^{-6} and 5.89×10^{-6} K^{-1} for TiN, AlN and TiAlN, respectively, derived from BSTM, are significantly higher. This divergence between the two techniques can be explained by the rather small grain size and high defect density, which is usually obtained for PVD coatings [180]. While the XRD measurements only reveal the change of the lattice constant with respect to the temperature without taking into account the role of non-crystalline phase fractions, BSTM gives a volume-averaged value. In the latter, effects originating from imperfections such as grain boundaries, which are known to have a significant influence on the CTE [165], are considered as well.

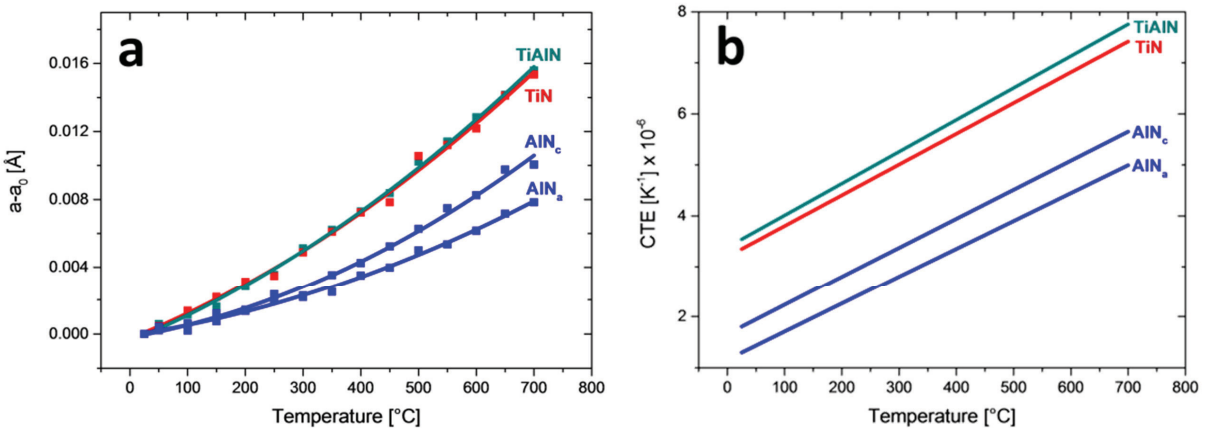

Fig. 8: *(a) Absolute change of the lattice parameter with temperature and (b) the resulting CTE´s of sputtered TiN, TiAlN and AlN coatings*[1].

It can be concluded that both techniques, BSTM (e.g. on coated Si strips) as well as high-temperature X-ray powder diffraction are feasible to determine the CTE of hard coatings. However, one drawback of BSTM is that it is hardly applicable for CVD coatings, as only one side of the wafer is supposed to be coated, whereas the X-ray powder diffraction requires a crystalline material in order to fulfill Bragg´s law. Considering these restrictions, a complementary use of both techniques facilitates the investigation of the CTE on almost every coating sample, independent of its microstructure and the used deposition technique.

[1] The coatings were deposited in an industrial scale PVD plant similar to [223]. The HT-XRD measurements were performed with $Cu_{K\alpha}$ radiation under vacuum using a Bruker D8 Advance diffractometer equipped with a position sensitive detector and an Anton Paar HTK 2000 high temperature chamber (base pressure $<1\times10^{-4}$ mbar). Diffraction patterns were collected from room temperature up to 700 °C, in steps of 50 °C. In order to determine the lattice parameter for each measurement, line-profile analysis was performed according to [224,225].

4.2 Thermal conductivity and specific heat capacity

As already discussed, wear resistant hard coatings are frequently exposed to high temperatures during service [6]. Thus, the thermal conductivity, quantifying the dissipation of heat within a tool material, is an important factor influencing its performance. For cutting applications, a low thermal conductivity is supposed to be beneficial, providing a thermal barrier in order to deflect the heat (and consequently temperature) into the chip and help to prevent overheating of the tool [181–183]. In addition, there is literature available discussing the benefits of anisotropic coating architectures, providing a reasonable heat barrier in cross-plane direction, and a high conductivity in the in-plane direction, guaranteeing pronounced lateral heat dissipation and thus, avoiding hot spots on the tool [181,182]. On the contrary, for molds used for die casting and polymer processing, quick heat dissipation is required to keep the cycle times low [184]. Well established methods for the determination of the thermal conductivity of hard coatings are the 3-ω technique, which is based on temperature dependent electrical measurements, and time-domain thermoreflectance (TDTR), which is based on temperature dependent optical measurements [185,186]. Here, ω refers to the applied current frequency.

The fundamentals of the 3-ω method can be related to Corbino [187], who discovered in the early 1900´s a third-harmonic oscillation of voltage caused by an alternating current applied to a resistive heater. From this harmonic oscillation, Corbino was able to assess the thermal properties of the heater material [187]. Cahill *et al.* [188–190] were the first to determine the thermal conductivity of dielectric solids by combining Corbino´s findings with the deposition of a small heater with the form of a metal strip on the surface of a dielectric specimen in the 1980´s, referring to as 3-ω method. Subsequently, this technique was also successfully applied to dielectric thin film samples with thicknesses of several microns [183,191]. Since then, the method has been permanently enhanced leading to the ability to reliably determine the thermal conductivity of films down to a thickness of ~100 nm [192]. Additional deposition of a dielectric insulation layer, several tens of nm thin, between the micro-heater and the sample surface expands the technique nowadays also to electrically conducting samples [193–195].

To successfully perform a 3-ω measurement on a hard coating, the surface of the sample should exhibit a smooth finish; thus, sample polishing might be necessary. After achieving a satisfying surface quality, the next step is to deposit a uniform dielectric insulation layer on the sample surface, e.g. 180 nm SiN deposited by low pressure CVD [193], in order to avoid fault currents flowing into the sample during the measurement. This is followed by the

deposition of a thin film micro-heater system using sputtering or thermal evaporation. The patterning of the micro-heater can be done either by photolithography and applying etching or lift off techniques, or alternatively by evaporation through masks [190,193]. Typically used materials for heating systems are metals with well-known temperature dependence of their electrical resistivity such as Au, Pt or Ag [186,193,196]. The micro-heating system usually consists of a narrow metal strip which acts as heater and four contacts, representing the two heating contacts to introduce the heating current and two probe contacts to determine the 3-ω signal. If a current with a frequency ω is applied to the heating contacts, the metal strip is heated with a frequency 2ω resulting in a time dependent temperature and, consequently, resistivity signal with a frequency of 2ω. Thereby, a third harmonic voltage with a frequency of 3ω can be determined at the probe contacts, yielding to the terminology 3-ω method. If the thermal excitation frequency is varied during the measurement, and the probe signal is determined as a function of the logarithmic thermal excitation frequency, a linear dependence between both can be found which is proportional to the thermal conductivity of the sample.

In contrast to the 3-ω method, TDTR is an optical method applying pulsed laser light to heat as well as to probe the sample surface. Early studies utilizing thermoreflectance measurements for the determination of the heat conductivity of samples were published by Paddock and Eesley [197] and Young *et al.* [198]. Later on, several authors adopted and improved this technique [199–203]. For TDTR measurements, a ~50 nm thick metallic transducer layer with a well-known temperature dependent optical reflectance such as Al or Au [204] needs to be deposited on the sample surface. In the ideal case, this is done by thermal evaporation under clean room conditions. Since the reflectance of the transducer layer might be affected by impurities and other imperfections, a mirror like surface finish prior to deposition is recommended. During the measurement, the transducer layer is irradiated with pulses of a pump beam exhibiting pulse durations in the picosecond regime. Thereby, the pump beam acts as heat source on the sample surface, consequently causing a slight increase in temperature. A probe beam with a much lower intensity compared to the pump beam is used to determine the time dependent reflectivity of the transducer layer after the pump pulse hits the surface. Once the time dependent reflectivity of the sample is known, the time dependent temperature gradient can be determined. The evolution of the normalized temperature with respect to the time delay can subsequently be used to reveal the thermal diffusivity of the sample, which is given by its thermal conductivity divided by the volumetric heat capacity (i.e. the product of its density and specific heat capacity). Typically, TDTR devices utilize one single laser source and mirrors, beam splitters and polarizers to split and align the pump and probe beams and to adjust their intensity ratio.

The beam path of the probe beam usually includes a mechanical delay stage to vary the path length of the probe beam, enabling the adjustment of the time delay of the probe pulse with respect to the pump pulse. From acoustic echoes appearing in the measured curve, the thickness of the transducer layer, which is needed for the data evaluation, can be determined with nm precision.

Using either the 3-ω or the TDTR method does not restrict the spectrum of coating materials to be investigated. The temperature dependent thermal conductivity of wear resistant CVD α- and κ-Al_2O_3 coatings was investigated using the 3-ω method [183]. For PVD TiAlN and AlCrN based hard coatings, there are studies available discussing the temperature dependent thermal conductivity determined by TDTR measurements [123,205]. In addition, the influence of the spinodal decomposition of metastable c-TiAlN on the thermal conductivity was examined *ex-situ* utilizing the TDTR method [206]. Further, TDTR investigations on the influence of the chemical composition of TiAlN, CrAlN and $TiN_{1-x}O_x$ [207–209] on the thermal conductivity can be found.

In some reports on TDTR measurements, mathematical models for the determination of the thermal diffusivity as well as the thermal effusivity are discussed [210–212], providing access to the whole portfolio of the thermo-physical properties of the investigated sample. However, those analysis methods are restricted to samples with a thermal conductivity below ~1 W/mK, which is limiting their applicability significantly. Hence, TDTR measurements are in general solely applied to reveal the thermal diffusivity of the sample. As mentioned above, for the calculation of the thermal conductivity from the thermal diffusivity, the specific heat capacity and the density of the sample need to be known. The density can be determined for example by X-ray reflectivity measurements [213]; however, the determination of the specific heat capacity is more complex. A frequently used technique to assess the specific heat capacity of solids and powders is differential scanning calorimetry (DSC) [214]. There, usually three measurements are required; *(i)* a blank run with two empty crucibles for the determination of the baseline signal of the apparatus, *(ii)* a measurement of a well-defined reference sample with known specific heat capacity such as sapphire or copper [215–218], and *(iii)* the measurement of the sample itself. The signal ratio of the reference and the actual sample is then used to calculate the specific heat capacity [214]. DSC measurements can be either performed continuously, which means continuous heating and signal recording over a certain temperature range or in steps resulting in averaged values for specific temperatures [219]. Another possibility is to determine the thermal conductivity as well as the volumetric heat capacity of the sample by complementary use of the 3-ω method and TDTR. Thereby, first the thermal conductivity is

determined using the 3-ω method. Afterwards, a TDTR measurement is performed. Within the mathematical model for the data evaluation, the thermal conductivity derived from the 3-ω method is applied and the volumetric heat capacity can be determined.

An example for measurements of the thermal conductivity of TiAlN based coatings in as-deposited state and after annealing at 1200 °C, using TDTR, is shown in Fig. 9a. The measurements on pure c-TiAlN, mixed c/w-TiAlN and mixed c/w-TiAlTaN coatings reveal rather low thermal conductivities in the as-deposited state. Rachbauer *et al.* [206] reported on similar low thermal conductivities for metastable c-TiAlN, which significantly increased after annealing. This could be related to the formation of networks of thermally well conducting TiN and AlN domains due to spinodal decomposition. A similar behavior can be observed in Fig. 9a for the c-TiAlN, while the low initial thermal conductivity can be more or less preserved during annealing of the nanocrystalline c/w-TiAlN and to an even greater extent for the c/w-TiAlTaN coating. This indicates that the initial microstructure and phase composition have a significant influence on microstructure evolution during annealing and thus, on the thermal conductivity. The slight increase with increasing annealing time can be related to recrystallization and recovery of point defects.

The specific heat capacity of TiN, AlN and c-TiAlN, determined by DSC using powdered samples, in the temperature range from 200 to 550 °C is shown in Fig. 9b. The dashed lines indicate the values for TiN and AlN, respectively, provided by NIST [220,221]. In the measured temperature range both, TiN as well as AlN, show almost perfect agreement with the values. For TiAlN, the measurement yields reasonable results, which are in good agreement with a mixture of TiN and AlN [222,223]. This example demonstrates that the specific heat capacity of hard coatings can be determined with adequate precision by DSC measurements of powdered coatings.

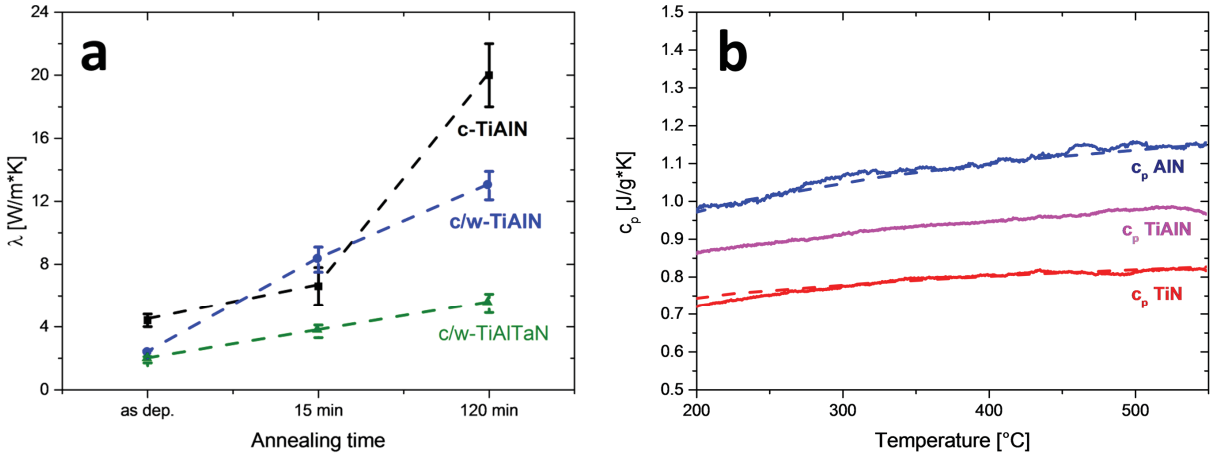

Fig. 9: *(a) Change of the thermal conductivity (λ) with increasing annealing time of TiAlN based coatings with different phase compositions. (b) Specific heat capacity (c_p) of TiN, TiAlN and AlN coatings determined by DSC. The c-TiAlN, TiN and AlN coatings were grown by sputter deposition, whereas cathodic arc evaporation was used for deposition of the mixed phase coatings.*

5. Conclusions

Economical demands to increase the throughput of production processes and consequently to reduce production costs result in constantly increasing mechanical and thermal loads applied to coated tools. Thus, requirements like high hot hardness at still reasonable toughness, good high-temperature stability and oxidation resistance as well as tailored thermo-physical properties become even more important. In that context, advanced characterization techniques for the investigation of coating characteristics like elemental and phase composition and microstructure in the nm regime, mechanical properties at elevated temperatures and correlations between composition and microstructure with thermo-physical properties gain increasing interest. Within the present work, advanced characterization techniques such as atom probe tomography, synchrotron X-ray nanodiffraction, micromechanical testing and methods for the determination of the thermo-physical properties were discussed. The presented portfolio of characterization techniques provides the tools for a future knowledge based design of hard coatings.

Acknowledgements

The authors would like to thank following persons for fruitful discussions or comments on this review, technical assistance and figures: Paul Mayrhofer, Richard Rachbauer, Marisa Rebelo de Figueiredo, Peter Hosemann, Angelika Zeilinger, Wießner Manfred, Alexandre Jacquot and Markus Winkler. Financial support by the Austrian Federal Government (in particular from the Bundesministerium für Verkehr, Innovation und Technologie and the

Bundesministerium für Wissenschaft, Forschung und Wirtschaft) and the Styrian Provincial Government, represented by Österreichische Forschungsförderungsgesellschaft mbH and by Steirische Wirtschaftsförderungsgesellschaft mbH, within the research activities of the K2 Competence Centre on “Integrated Research in Materials, Processing and Product Engineering”, operated by the Materials Center Leoben Forschung GmbH in the framework of the Austrian COMET Competence Centre Programme, is gratefully acknowledged.

Bibliography

[1] M. Kathrein, C. Michotte, M. Penoy, P. Polcik, C. Mitterer, Multifunctional multi-component PVD coatings for cutting tools, Surf. Coat. Technol. 200 (2005) 1867–1871.

[2] P.H. Mayrhofer, C. Mitterer, L. Hultman, H. Clemens, Microstructural design of hard coatings, Prog. Mater. Sci. 51 (2006) 1032–1114.

[3] C. Mitterer, PVD and CVD hard coatings, in: V.K. Sarin, L. Llanes, D. Mari, C.E. Nebel (Eds.), Comprehensive Hard Materials Vol. 2, Elsevier, London, 2014, pp. 449–467.

[4] U. Schleinkofer, C. Czettl, C. Michotte, Coating applications for cutting tools, in: V.K. Sarin, L. Llanes, D. Mari, C.E. Nebel (Eds.), Comprehensive Hard Materials Vol. 1, Elsevier, London, 2014, pp. 453–469.

[5] C. Czettl, Design of CVD Coatings for Cutting Tools, PhD Thesis, Montanuniversität Leoben, 2013.

[6] G. List, G. Sutter, A. Bouthiche, Cutting temperature prediction in high speed machining by numerical modelling of chip formation and its dependence with crater wear, Int. J. Mach. Tools Manuf. 54-55 (2012) 1–9.

[7] A. Osada, E. Nakamura, H. Homma, T. Hayahi, T. Oshika, Wear mechanism of thermally transformed CVD Al_2O_3 layer, Int. J. Refract. Met. Hard Mater. 24 (2006) 387–391.

[8] S. Vuorinen, L. Karlsson, Phase transformation in chemically vapour-deposited κ-alumina, Thin Solid Films 214 (1992) 132–143.

[9] P. Schlund, P. Kindermann, R. Schulte, H.G. Sockel, U. Schleinkofer, K. Görting, W. Heinrich, Mechanical behaviour of PVD/CVD-coated hard metals under cyclic loads, Int. J. Refract. Met. Hard Mater. 17 (1999) 179–185.

[10] E.W. Müller, K. Bahadur, Field ionization of gases at a metal surface and the resolution of the field ion microscope, Phys. Rev. 102 (1956) 624–631.

[11] E.W. Müller, J.A. Panitz, S. Brooks McLane, The atom-probe field ion microscope, Rev. Sci. Instrum. 39 (1968) 83–86.

[12] T.F. Kelly, M.K. Miller, Invited review article: Atom probe tomography, Rev. Sci. Instrum. 78 (2007) 031101.

[13] M.K. Miller, R.G. Forbes, Atom probe tomography, Mater. Charact. 60 (2009) 461–469.

[14] A. Cerezo, P.H. Clifton, M.J. Galtrey, C.J. Humphreys, T.F. Kelly, D.J. Larson, S. Lozano-perez, E.A. Marquis, R.A. Oliver, G. Sha, K. Thompson, M. Zandbergen, R.L. Alvis, Atom probe tomography today, Mater. Today 10 (2007) 36–42.

[15] D.N. Seidman, Three-dimensional atom-probe tomography: Advances and applications, Annu. Rev. Mater. Res. 37 (2007) 127–158.

[16] M.K. Miller, T.F. Kelly, K. Rajan, S.P. Ringer, The future of atom probe tomography, Mater. Today 15 (2012) 158–165.

[17] T.F. Kelly, P.P. Camus, D.J. Larson, L.M. Holzman, S.S. Bajikar, On the many advantages of local-electrode atom probes, Ultramicroscopy 62 (1996) 29–42.

[18] G.L. Kellogg, T.T. Tsong, Pulsed-laser atom-probe field-ion microscopy, J. Appl. Phys. 51 (1980) 1184–1193.

[19] G.L. Kellogg, Field ion microscopy and pulsed laser atom-probe mass spectroscopy of insulating glasses, J. Appl. Phys. 53 (1982) 6383–6386.

[20] M.K. Miller, K.F. Russell, G.B. Thompson, Strategies for fabricating atom probe specimens with a dual beam FIB, Ultramicroscopy 102 (2005) 287–298.

[21] R. Rachbauer, S. Massl, E. Stergar, P. Felfer, P.H. Mayrhofer, Atom probe specimen preparation and 3D interfacial study of Ti-Al-N thin films, Surf. Coat. Technol. 204 (2010) 1811–1816.

[22] M.K. Miller, K.F. Russell, K. Thompson, R. Alvis, D.J. Larson, Review of atom probe FIB-based specimen preparation methods, Microsc. Microanal. 13 (2007) 428–436.

[23] P.-P. Choi, I. Povstugar, J.-P. Ahn, A. Kostka, D. Raabe, Thermal stability of TiAlN/CrN multilayer coatings studied by atom probe tomography, Ultramicroscopy 111 (2011) 518–523.

[24] I. Povstugar, P.-P. Choi, D. Tytko, J.-P. Ahn, D. Raabe, Interface-directed spinodal decomposition in TiAlN/CrN multilayer hard coatings studied by atom probe tomography, Acta Mater. 61 (2013) 7534–7542.

[25] L.J.S. Johnson, M. Thuvander, K. Stiller, M. Odén, L. Hultman, Spinodal decomposition of $Ti_{0.33}Al_{0.67}N$ thin films studied by atom probe tomography, Thin Solid Films 520 (2012) 4362–4368.

[26] R. Rachbauer, E. Stergar, S. Massl, M. Moser, P.H. Mayrhofer, Three-dimensional atom probe investigations of Ti-Al-N thin films, Scripta Mater. 61 (2009) 725–728.

[27] F. Tang, B. Gault, S.P. Ringer, P. Martin, A. Bendavid, J.M. Cairney, Microstructural investigation of Ti-Si-N hard coatings, Scripta Mater. 63 (2010) 192–195.

[28] M. Jílek Jr., M. Jílek, F. Mendez Martin, P.H. Mayrhofer, S. Veprek, High-rate deposition of AlTiN and related coatings with dense morphology by central cylindrical direct current magnetron sputtering, Thin Solid Films 556 (2014) 361–368.

[29] P.H. Mayrhofer, A. Hörling, L. Karlsson, J. Sjölén, T. Larsson, C. Mitterer, L. Hultman, Self-organized nanostructures in the Ti-Al-N system, Appl. Phys. Lett. 83 (2003) 2049–2051.

[30] R. Rachbauer, S. Massl, E. Stergar, D. Holec, D. Kiener, J. Keckes, J. Patscheider, M. Stiefel, H. Leitner, P.H. Mayrhofer, Decomposition pathways in age hardening of Ti-Al-N films, J. Appl. Phys. 110 (2011) 023515.

[31] M. Ibrahim, Z. Balogh, P. Stender, R. Schlesiger, G.-H. Greiwe, G. Schmitz, B. Parditka, G.A. Langer, A. Csik, Z. Erdélyi, On the influence of the stacking sequence in the nucleation of Cu_3Si: Experiment and the testing of nucleation models, Acta Mater. 76 (2014) 306–313.

[32] M. Mühlbacher, F. Mendez-Martin, B. Sartory, N. Schalk, J. Keckes, J. Lu, L. Hultman, C. Mitterer, Copper diffusion into single-crystalline TiN studied by transmission electron microscopy and atom probe tomography, Thin Solid Films 574 (2015) 103–109.

[33] A.J. Schwartz, M. Kumar, B.L. Adams, D.P. Field, Electron Backscatter Diffraction in Materials Science, 2nd ed., Springer, New York, 2009.

[34] W. Zhou, Z.L. Wang, Scanning microscopy for nanotechnology: Techniques and Applications, 1st ed., Springer, New York, 2007.

[35] F.J. Humphreys, Grain and subgrain characterisation by electron backscatter diffraction, J. Mater. Sci. 36 (2001) 3833–3854.

[36] F.J. Humphreys, Quantitative metallography by electron backscattered diffraction, J. Microsc. 195 (1999) 170–185.

[37] D. Dingley, Progressive steps in the development of electron backscatter diffraction and orientation imaging microscopy, J. Microsc. 213 (2004) 214–224.

[38] S.I. Wright, M.M. Nowell, D.P. Field, A review of strain analysis using electron backscatter diffraction, Microsc. Microanal. 17 (2011) 316–329.

[39] D. Stojakovic, Electron backscatter diffraction in materials characterization, Process. Appl. Ceram. 6 (2012) 1–13.

[40] A.J. Wilkinson, T.B. Britton, Strains, planes, and EBSD in materials science, Mater. Today 15 (2012) 366–376.

[41] V. Randle, Electron backscatter diffraction: Strategies for reliable data acquisition and processing, Mater. Charact. 60 (2009) 913–922.

[42] S. Kikuchi, Diffraction of cathode rays by mica, Proc. Imp. Acad. 4 (1928) 271–274.

[43] R.O. Duda, P.E. Hart, Use of the Hough transformation to detect lines and curves in pictures, Commun. ACM 15 (1972) 11–15.

[44] J. Hjelen, R. Ørsund, E. Hoel, P. Runde, T. Furu, E. Nes, EBSP, progress in technique and applications, Texture. Microstruct. 20 (1993) 29–40.

[45] K.Z. Troost, Submicron crystallography in the scanning electron microscope, Philips J. Res 47 (1993) 151–163.

[46] D. Chen, J.-C. Kuo, W.-T. Wu, Effect of microscopic parameters on EBSD spatial resolution, Ultramicroscopy 111 (2011) 1488–1494.

[47] D.P. Field, Improving the spatial resolution of EBSD, Microsc. Microanal. 11 (2005) 52–53.

[48] C.J. Harland, P. Akhter, J.A. Venables, Accurate microcrystallography at high spatial resolution using electron back-scattering patterns in a field emission gun scanning electron microscope, J. Phys. E. Sci. Instrum. 14 (1981) 175–182.

[49] D.R. Steinmetz, S. Zaefferer, Towards ultrahigh resolution EBSD by low accelerating voltage, Mater. Sci. Technol. 26 (2010) 640–645.

[50] F.J. Humphreys, Characterisation of fine-scale microstructures by electron backscatter diffraction (EBSD), Scripta Mater. 51 (2004) 771–776.

[51] S.I. Wright, M.M. Nowell, EBSD image quality mapping, Microsc. Microanal. 12 (2006) 72–84.

[52] S.J. Dillon, G.S. Rohrer, Characterization of the grain-boundary character and energy distributions of yttria using automated serial sectioning and EBSD in the FIB, J. Am. Ceram. Soc. 92 (2009) 1580–1585.

[53] L. Helmick, S.J. Dillon, K. Gerdes, R. Gemmen, G.S. Rohrer, S. Seetharaman, P.A. Salvador, Crystallographic characteristics of grain boundaries in dense yttria-stabilized zirconia, Int. J. Appl. Ceram. Technol. 8 (2011) 1218–1228.

[54] H. Chien, C. Diaz-Jimenez, G.S. Rohrer, Z. Ban, P. Prichard, Y. Liu, The influence of residual thermal stresses on the mechanical properties of multilayer α-Al_2O_3/TiC_xN_{1-x} coatings on WC/Co cutting tools, Surf. Coat. Technol. 215 (2013) 119–126.

[55] H. Chien, M.C. Gao, H.M. Miller, G.S. Rohrer, Z. Ban, P. Prichard, Y. Liu, Microtexture and hardness of CVD deposited α-Al_2O_3 and TiC_xN_{1-x} coatings, Int. J. Refract. Met. Hard Mater. 27 (2009) 458–464.

[56] C.B. Garcia, E. Ariza, C.J. Tavares, P. Villechaise, Electron backscatter diffraction analysis of ZnO:Al thin films, Appl. Surf. Sci. 259 (2012) 590–595.

[57] S.P. Pemmasani, K.V. Rajulapati, M. Ramakrishna, K. Valleti, R.C. Gundakaram, S.V. Joshi, Characterization of multilayer nitride coatings by electron microscopy and modulus mapping, Mater. Charact. 81 (2013) 7–18.

[58] S.A. Lajevardi, T. Shahrabi, J.A. Szpunar, A. Sabour Rouhaghdam, S. Sanjabi, Characterization of the microstructure and texture of functionally graded nickel-Al_2O_3 nano composite coating produced by pulse deposition, Surf. Coat. Technol. 232 (2013) 851–859.

[59] M. Tkadletz, J. Keckes, N. Schalk, I. Krajinovic, M. Burghammer, C. Czettl, C. Mitterer, Residual stress gradients in α-Al_2O_3 hard coatings determined by pencil-beam X-ray nanodiffraction: The influence of blasting media, Surf. Coat. Technol. 262 (2015) 134–140.

[60] J.M. Cowley, Applications of electron nanodiffraction, Micron 35 (2004) 345–360.

[61] J.M. Cowley, Electron nanodiffraction: Progress and prospects, J. Electron Microsc. 10 (1996) 3–10.

[62] J.M. Cowley, Electron nanodiffraction, Microsc. Res. Tech. 46 (1999) 75–97.

[63] W. Yang, B.C. Larson, J.Z. Tischler, G.E. Ice, J.D. Budai, W. Liu, Differential-aperture X-ray structural microscopy: A submicron-resolution three-dimensional probe of local microstructure and strain, Micron 35 (2004) 431–439.

[64] G.E. Ice, J.W.L. Pang, R.I. Barabash, Y. Puzyrev, Characterization of three-dimensional crystallographic distributions using polychromatic X-ray microdiffraction, Scripta Mater. 55 (2006) 57–62.

[65] J.D. Budai, W. Liu, J.Z. Tischler, Z.W. Pan, D.P. Norton, B.C. Larson, W. Yang, G.E. Ice, Polychromatic X-ray micro- and nanodiffraction for spatially-resolved structural studies, Thin Solid Films 516 (2008) 8013–8021.

[66] S. Di Fonzo, W. Jark, S. Lagomarsino, C. Giannini, L. De Caro, A. Cedola, M. Muller, Non-destructive determination of local strain with 100-nanometre spatial resolution, Nature 403 (2000) 638–640.

[67] C. Riekel, M. Burghammer, R. Davies, Progress in micro- and nano-diffraction at the ESRF ID13 beamline, IOP Conf. Ser.: Mater. Sci. Eng. 14 (2010) 012013.

[68] J. Keckes, M. Bartosik, R. Daniel, C. Mitterer, G. Maier, W. Ecker, J. Vila-Comamala, C. David, S. Schoeder, M. Burghammer, X-ray nanodiffraction reveals strain and microstructure evolution in nanocrystalline thin films, Scripta Mater. 67 (2012) 748–751.

[69] N. Vaxelaire, P. Gergaud, G.B.M. Vaughan, Sub-micrometre depth-gradient measurements of phase, strain and texture in polycrystalline thin films: a nano-pencil beam diffraction approach, J. Appl. Cryst. 47 (2014) 495–504.

[70] A.P. Hammersley, S.O. Svensson, M. Hanfland, A.N. Fitch, D. Hausermann, Two-dimensional detector software: From real detector to idealised image or two-theta scan, High Press. Res. 14 (1996) 235–248.

[71] J. Kieffer, D. Karkoulis, PyFAI, a versatile library for azimuthal regrouping, J. Phys. Conf. Ser. 425 (2013) 202012.

[72] J. Kieffer, J. Wright, PyFAI: A python library for high performance azimuthal integration on GPU, Powder Diffr. 28 (2013) 339–350.

[73] M. Stefenelli, J. Todt, A. Riedl, W. Ecker, T. Müller, R. Daniel, M. Burghammer, J. Keckes, X-ray analysis of residual stress gradients in TiN coatings by a Laplace space approach and cross-sectional nanodiffraction: a critical comparison, J. Appl. Cryst. 46 (2013) 1378–1385.

[74] J. Todt, R. Pitonak, A. Köpf, R. Weißenbacher, B. Sartory, M. Burghammer, R. Daniel, T. Schöberl, J. Keckes, Superior oxidation resistance, mechanical properties and residual stresses of an Al-rich nanolamellar $Ti_{0.05}Al_{0.95}N$ coating prepared by CVD, Surf. Coat. Technol. 258 (2014) 1119–1127.

[75] M. Bartosik, R. Daniel, C. Mitterer, I. Matko, M. Burghammer, P.H. Mayrhofer, J. Keckes, Cross-sectional X-ray nanobeam diffraction analysis of a compositionally graded CrN_x thin film, Thin Solid Films 542 (2013) 1–4.

[76] R. Daniel, J. Keckes, I. Matko, M. Burghammer, C. Mitterer, Origins of microstructure and stress gradients in nanocrystalline thin films: The role of growth parameters and self-organization, Acta Mater. 61 (2013) 6255–6266.

[77] N. Schalk, J. Keckes, C. Czettl, M. Burghammer, M. Penoy, C. Michotte, C. Mitterer, Investigation of the origin of compressive residual stress in CVD TiB_2 hard coatings using synchrotron X-ray nanodiffraction, Surf. Coat. Technol. 258 (2014) 121–126.

[78] W.C. Oliver, G.M. Pharr, An improved technique for determining hardness and elastic modulus using load and displacement sensing indentation experiments, J. Mater. Res. 7 (1992) 1564–1583.

[79] W.C. Oliver, G.M. Pharr, Measurement of hardness and elastic modulus by instrumented indentation: Advances in understanding and refinements to methodology, J. Mater. Res. 19 (2004) 3–20.

[80] D.A. Lucca, K. Herrmann, M.J. Klopfstein, Nanoindentation: Measuring methods and applications, CIRP Ann. - Manuf. Technol. 59 (2010) 803–819.

[81] A. Leyland, A. Matthews, On the significance of the H/E ratio in wear control: A nanocomposite coating approach to optimised tribological behaviour, Wear 246 (2000) 1–11.

[82] A. Leyland, A. Matthews, Design criteria for wear-resistant nanostructured and glassy-metal coatings, Surf. Coat. Technol. 177-178 (2004) 317–324.

[83] B.D. Beake, G.S. Fox-Rabinovich, Progress in high temperature nanomechanical testing of coatings for optimising their performance in high speed machining, Surf. Coat. Technol. 255 (2014) 102–111.

[84] F. Giuliani, A. Goruppa, S.J. Lloyd, D. Teer, W.J. Clegg, High temperature deformation of AlN/CrN multilayers using nanoindentation, MRS Proc. 841 (2011) 159–164.

[85] M. Rebelo de Figueiredo, M.D. Abad, A.J. Harris, C. Czettl, C. Mitterer, P. Hosemann, Nanoindentation of CVD Al_2O_3 hard coatings at elevated temperatures, Thin Solid Films 578 (2015) 20–24.

[86] C.A. Schuh, C.E. Packard, A.C. Lund, Nanoindentation and contact-mode imaging at high temperatures, J. Mater. Res. 21 (2006) 725–736.

[87] N.M. Everitt, M.I. Davies, J.F. Smith, High temperature nanoindentation - the importance of isothermal contact, Philos. Mag. 91 (2011) 1221–1244.

[88] Z.C. Duan, A.M. Hodge, High-temperature nanoindentation: New developments and ongoing challenges, JOM 61 (2009) 32–36.

[89] S. Korte, R.J. Stearn, J.M. Wheeler, W.J. Clegg, High temperature microcompression and nanoindentation in vacuum, J. Mater. Res. 27 (2012) 167–176.

[90] J.C. Trenkle, C.E. Packard, C.A. Schuh, Hot nanoindentation in inert environments, Rev. Sci. Instrum. 81 (2010) 073901.

[91] J.M. Wheeler, J. Michler, Invited article: Indenter materials for high temperature nanoindentation, Rev. Sci. Instrum. 84 (2013) 101301.

[92] B.D. Beake, G.S. Fox-Rabinovich, S.C. Veldhuis, S.R. Goodes, Coating optimisation for high speed machining with advanced nanomechanical test methods, Surf. Coat. Technol. 203 (2009) 1919–1925.

[93] G.S. Fox-Rabinovich, S.C. Veldhuis, G.K. Dosbaeva, K. Yamamoto, A.I. Kovalev, D.L. Wainstein, I.S. Gershman, L.S. Shuster, B.D. Beake, Nanocrystalline coating design for extreme applications based on the concept of complex adaptive behavior, J. Appl. Phys. 103 (2008) 083510.

[94] B.D. Beake, J.F. Smith, High-temperature nanoindentation testing of fused silica and other materials, Philos. Mag. A 82 (2002) 2179–2186.

[95] K.D. Bouzakis, M. Pappa, G. Skordaris, E. Bouzakis, S. Gerardis, Correlation between PVD coating strength properties and impact resistance at ambient and elevated temperatures, Surf. Coat. Technol. 205 (2010) 1481–1485.

[96] G.S. Fox-Rabinovich, B.D. Beake, J.L. Endrino, S.C. Veldhuis, R. Parkinson, L.S. Shuster, M.S. Migranov, Effect of mechanical properties measured at room and elevated temperatures on the wear resistance of cutting tools with TiAlN and AlCrN coatings, Surf. Coat. Technol. 200 (2006) 5738–5742.

[97] B.D. Beake, J.F. Smith, A. Gray, G.S. Fox-Rabinovich, S.C. Veldhuis, J.L. Endrino, Investigating the correlation between nano-impact fracture resistance and hardness/modulus ratio from nanoindentation at 25–500 °C and the fracture resistance and lifetime of cutting tools with $Ti_{1-x}Al_xN$ (x=0.5 and 0.67) PVD coatings, Surf. Coat. Technol. 201 (2007) 4585–4593.

[98] B.D. Beake, G.S. Fox-Rabinovich, Y. Losset, K. Yamamoto, M.H. Agguire, S.C. Veldhuis, J.L. Endrino, A.I. Kovalev, Why can TiAlCrSiYN-based adaptive coatings deliver exceptional performance under extreme frictional conditions?, Faraday Discuss. 156 (2012) 267–277.

[99] Y.X. Wang, S. Zhang, Toward hard yet tough ceramic coatings, Surf. Coat. Technol. 258 (2014) 1–16.

[100] D. Gross, T. Seelig, Bruchmechanik - Mit einer Einführung in die Mikromechanik, 5th ed., Springer, Berlin Heidelberg, 2011.

[101] G.R. Anstis, P. Chantikul, B.R. Lawn, D.B. Marshall, A critical evaluation of indentation techniques for measuring fracture toughness: I, direct crack measurements, J. Am. Ceram. Soc. 64 (1981) 533–538.

[102] J. Yan, A.M. Karlsson, X. Chen, On internal cone cracks induced by conical indentation in brittle materials, Eng. Fract. Mech. 74 (2007) 2535–2546.

[103] A. Leonardi, F. Furgiuele, R.J.K. Wood, S. Syngellakis, Numerical analysis of brittle materials fractured by sharp indenters, Eng. Fract. Mech. 77 (2010) 264–276.

[104] J. Chen, S.J. Bull, Modelling the limits of coating toughness in brittle coated systems, Thin Solid Films 517 (2009) 2945–2952.

[105] J. Chen, On the determination of coating toughness during nanoindentation, Surf. Coat. Technol. 206 (2012) 3064–3068.

[106] J. Ding, Y. Meng, S. Wen, Mechanical properties and fracture toughness of multilayer hard coatings using nanoindentation, Thin Solid Films 371 (2000) 178–182.

[107] H. Wang, B. Wang, S. Li, Q. Xue, F. Huang, Toughening magnetron sputtered TiB_2 coatings by Ni addition, Surf. Coat. Technol. 232 (2013) 767–774.

[108] Y.X. Wang, S. Zhang, J.-W. Lee, W.S. Lew, B. Li, Influence of bias voltage on the hardness and toughness of CrAlN coatings via magnetron sputtering, Surf. Coat. Technol. 206 (2012) 5103–5107.

[109] S. Zhang, X. Zhang, Toughness evaluation of hard coatings and thin films, Thin Solid Films 520 (2012) 2375–2389.

[110] Z. Xia, W.A. Curtin, B.W. Sheldon, A new method to evaluate the fracture toughness of thin films, Acta Mater. 52 (2004) 3507–3517.

[111] C. Wang, J. Han, J.M. Pureza, Y.-W. Chung, Structure and mechanical properties of $Fe_{1-x}Mn_x/TiB_2$ multilayer coatings: Possible role of transformation toughening, Surf. Coat. Technol. 237 (2013) 158–163.

[112] C. Wang, K. Shi, C. Gross, J.M. Pureza, M. de Mesquita Lacerda, Y.W. Chung, Toughness enhancement of nanostructured hard coatings: Design strategies and toughness measurement techniques, Surf. Coat. Technol. 257 (2014) 206–212.

[113] M.D. Uchic, D.M. Dimiduk, J.N. Florando, W.D. Nix, Sample dimensions influence strength and crystal plasticity, Science 305 (2004) 986–989.

[114] G. Dehm, H.P. Wörgötter, S. Cazottes, J.M. Purswani, D. Gall, C. Mitterer, D. Kiener, Can micro-compression testing provide stress-strain data for thin films?, Thin Solid Films 518 (2009) 1517–1521.

[115] D. Kiener, C. Motz, G. Dehm, Micro-compression testing: A critical discussion of experimental constraints, Mater. Sci. Eng. A 505 (2009) 79–87.

[116] M. Schlögl, C. Kirchlechner, J. Paulitsch, J. Keckes, P.H. Mayrhofer, Effects of structure and interfaces on fracture toughness of CrN/AlN multilayer coatings, Scripta Mater. 68 (2013) 917–920.

[117] J.M. Wheeler, R. Raghavan, V. Chawla, M. Morstein, J. Michler, Deformation of hard coatings at elevated temperatures, Surf. Coat. Technol. 254 (2014) 382–387.

[118] S. Liu, J.M. Wheeler, P.R. Howie, X.T. Zeng, J. Michler, W.J. Clegg, Measuring the fracture resistance of hard coatings, Appl. Phys. Lett. 102 (2013) 171907.

[119] A. Riedl, R. Daniel, M. Stefenelli, T. Schöberl, O. Kolednik, C. Mitterer, J. Keckes, A novel approach for determining fracture toughness of hard coatings on the micrometer scale, Scripta Mater. 67 (2012) 708–711.

[120] S. Massl, W. Thomma, J. Keckes, R. Pippan, Investigation of fracture properties of magnetron-sputtered TiN films by means of a FIB-based cantilever bending technique, Acta Mater. 57 (2009) 1768–1776.

[121] A. Zeilinger, R. Daniel, M. Stefenelli, B. Sartory, L. Chitu, M. Burghammer, T. Schöberl, O. Kolednik, J. Keckes, C. Mitterer, Mechanical property enhancement in laminates through control of morphology and crystal orientation, J. Phys. D. Appl. Phys. 48 (2015) 295303.

[122] E. Rabinowicz, Friction and wear of materials, 2nd ed., John Wiley & Sons, New York, 1995.

[123] W. Kalss, A. Reiter, V. Derflinger, C. Gey, J.L. Endrino, Modern coatings in high performance cutting applications, Int. J. Refract. Met. Hard Mater. 24 (2006) 399–404.

[124] J. Rech, A. Kusiak, J.L. Battaglia, Tribological and thermal functions of cutting tool coatings, Surf. Coat. Technol. 186 (2004) 364–371.

[125] K. Holmberg, A. Matthews, Coatings Tribology: Properties, Mechanisms, Techniques and Applications in Surface Engineering, 2nd ed., Elsevier Science, Oxford, 2009.

[126] J.F. Archard, Contact and rubbing of flat surfaces, J. Appl. Phys. 24 (1953) 981–988.

[127] J.F. Archard, W. Hirst, The wear of metals under unlubricated conditions, Proc. R. Soc. A 236 (1956) 397–410.

[128] A.A. Voevodin, J.M. Schneider, C. Rebholz, A. Matthews, Multilayer composite ceramic-metal-DLC coatings for sliding wear applications, Tribol. Int. 29 (1996) 559–570.

[129] J. Robertson, Diamond-like amorphous carbon, Mater. Sci. Eng. R Rep. 37 (2002) 129–281.

[130] D.S. Kim, T.E. Fischer, B. Gallois, The effects of oxygen and humidity on friction and wear of diamond-like carbon films, Surf. Coat. Technol. 49 (1991) 537–542.

[131] C. Donnet, A. Grill, Friction control of diamond-like carbon coatings, Surf. Coat. Technol. 94-95 (1997) 456–462.

[132] H. Ronkainen, S. Varjus, J. Koskinen, K. Holmberg, Differentiating the tribological performance of hydrogenated and hydrogen-free DLC coatings, Wear 249 (2001) 260–266.

[133] M. Grischke, K. Bewilogua, K. Trojan, H. Dimigen, Application-oriented modifications of deposition processes for diamond-like-carbon-based coatings, Surf. Coat. Technol. 74-75 (1995) 739–745.

[134] K. Bewilogua, C.V. Cooper, C. Specht, J. Schröder, R. Wittorf, M. Grischke, Effect of target material on deposition and properties of metal-containing DLC (Me-DLC) coatings, Surf. Coat. Technol. 127 (2000) 224–232.

[135] K. Bewilogua, C.V. Cooper, C. Specht, J. Schröder, R. Wittorf, M. Grischke, Erratum to: `Effect of target material on deposition and properties of metal-containing DLC (Me-DLC) coatings' [Surf. Coat. Technol. 127 (2000) 224-234], Surf. Coat. Technol. 132 (2000) 275–283.

[136] J. Rechberger, P. Brunner, R. Dubach, High performance cutting tools with a solid lubricant physically vapour-deposited coating, Surf. Coat. Technol. 62 (1993) 393–398.

[137] R. Gilmore, M.A. Baker, P.N. Gibson, W. Gissler, M. Stoiber, P. Losbichler, C. Mitterer, Low-friction TiN-MoS_2 coatings produced by dc magnetron co-deposition, Surf. Coat. Technol. 108-109 (1998) 345–351.

[138] R. Dubach, H. Curtins, H. Rechberger, Improved tool performance through metastability in hard coatings, Surf. Coat. Technol. 94-95 (1997) 622–626.

[139] Y.W. Bae, W.Y. Lee, T.M. Besmann, C.S. Yust, P.J. Blau, Preparation and friction characteristics of self-lubricating TiN-MoS_2 composite coatings, Mater. Sci. Eng. A 209 (1996) 372–376.

[140] R. Gilmore, M.A. Baker, P.N. Gibson, W. Gissler, Preparation and characterization of low-friction TiB_2-based coatings by incorporation of C or MoS_2, Surf. Coat. Technol. 105 (1998) 45–50.

[141] R. Goller, P. Torri, M.A. Baker, R. Gilmore, W. Gissler, The deposition of low-friction TiN–MoS_x hard coatings by a combined arc evaporation and magnetron sputter process, Surf. Coat. Technol. 120-121 (1999) 453–457.

[142] D.-Y. Wang, C.-L. Chang, Z.-Y. Chen, W.-Y. Ho, Microstructural and tribological characterization of MoS_2-Ti composite solid lubricating films, Surf. Coat. Technol. 120-121 (1999) 629–635.

[143] S. Carrera, O. Salas, J.J. Moore, A. Woolverton, E. Sutter, Performance of CrN/MoS_2(Ti) coatings for high wear low friction applications, Surf. Coat. Technol. 167 (2003) 25–32.

[144] A.A. Voevodin, J.S. Zabinski, Load-adaptive crystalline-amorphous nanocomposites, J. Mater. Sci. 33 (1998) 319–327.

[145] K. Polychronopoulou, C. Rebholz, M.A. Baker, L. Theodorou, N.G. Demas, S.J. Hinder, A.A. Polycarpou, C.C. Doumanidis, K. Böbel, Nanostructure, mechanical and tribological properties of reactive magnetron sputtered TiC_x coatings, Diam. Relat. Mater. 17 (2008) 2054–2061.

[146] C. Tsotsos, K. Polychronopoulou, N.G. Demas, G. Constantinides, S. Gravani, K. Böbel, M.A. Baker, A.A. Polycarpou, C. Rebholz, Mechanical and high pressure tribological properties of nanocrystalline Ti(N,C) and amorphous C:H nanocomposite coatings, Diam. Relat. Mater. 19 (2010) 960–963.

[147] W. Grzesik, Z. Zalisz, P. Nieslony, Friction and wear testing of multilayer coatings on carbide substrates for dry machining applications, Surf. Coat. Technol. 155 (2002) 37–45.

[148] X. Wang, P.Y. Kwon, D. Schrock, D. (Dae-Wook) Kim, Friction coefficient and sliding wear of AlTiN coating under various lubrication conditions, Wear 304 (2013) 67–76.

[149] J.M. Fildes, S.J. Meyers, C.P. Mulligan, R. Kilaparti, Evaluation of the wear and abrasion resistance of hard coatings by ball-on-three-disk test methods-a case study, Wear 302 (2013) 1040–1049.

[150] W. Grzesik, J. Rech, K. Zak, Determination of friction in metal cutting with tool wear and flank face effects, Wear 317 (2014) 8–16.

[151] A. Mkaddem, A. Ben Soussia, M. El Mansori, Wear resistance of CVD and PVD multilayer coatings when dry cutting fiber reinforced polymers (FRP), Wear 302 (2013) 946–954.

[152] N. Schalk, C. Mitterer, I. Letofsky-Papst, C. Czettl, B. Sartory, M. Penoy, C. Michotte, Friction reduction by thermal treatment of arc evaporated TiAlTaN coatings in methane, Tribol. Int. 67 (2013) 54–60.

[153] O. Jantschner, S.K. Field, D. Holec, A. Fian, D. Music, J.M. Schneider, Origin of temperature-induced low friction of sputtered Si-containing amorphous carbon coatings, Acta Mater. 82 (2015) 437–446.

[154] J. Nohava, P. Dessarzin, P. Karvankova, M. Morstein, Characterization of tribological behavior and wear mechanisms of novel oxynitride PVD coatings designed for applications at high temperatures, Tribol. Int. 81 (2015) 231–239.

[155] N. Schalk, C. Mitterer, C. Czettl, B. Sartory, M. Penoy, C. Michotte, Dry-blasting of α- and κ-Al_2O_3 CVD hard coatings: Friction behaviour and thermal stress relaxation, Tribol. Lett. 52 (2013) 147–154.

[156] M. Tkadletz, C. Mitterer, B. Sartory, I. Letofsky-Papst, C. Czettl, C. Michotte, The effect of droplets in arc evaporated TiAlTaN hard coatings on the wear behavior, Surf. Coat. Technol. 257 (2014) 95–101.

[157] A.A. Voevodin, C. Muratore, S.M. Aouadi, Hard coatings with high temperature adaptive lubrication and contact thermal management: review, Surf. Coat. Technol. 257 (2014) 247–265.

[158] M. Rebelo de Figueiredo, C. Muratore, R. Franz, R.R. Chromik, K.J. Wahl, A.A. Voevodin, M. O'Sullivan, M. Lechthaler, C. Mitterer, In situ studies of $TiC_{1-x}N_x$ hard coating tribology, Tribol. Lett. 40 (2010) 365–373.

[159] R.R. Chromik, C.C. Baker, A.A. Voevodin, K.J. Wahl, In situ tribometry of solid lubricant nanocomposite coatings, Wear 262 (2007) 1239–1252.

[160] C. Muratore, J.E. Bultman, S.M. Aouadi, A.A. Voevodin, In situ Raman spectroscopy for examination of high temperature tribological processes, Wear 270 (2011) 140–145.

[161] C.C. Baker, R.R. Chromik, K.J. Wahl, J.J. Hu, A.A. Voevodin, Preparation of chameleon coatings for space and ambient environments, Thin Solid Films 515 (2007) 6737–6743.

[162] R. Daniel, K.J. Martinschitz, J. Keckes, C. Mitterer, The origin of stresses in magnetron-sputtered thin films with zone T structures, Acta Mater. 58 (2010) 2621–2633.

[163] P.H. Mayrhofer, C. Mitterer, J. Musil, Structure-property relationships in single-and dual-phase nanocrystalline hard coatings, Surf. Coat. Technol. 174-175 (2003) 725–731.

[164] P.H. Mayrhofer, C. Mitterer, High-temperature properties of nanocomposite TiB_xN_y and TiB_xC_y coatings, Surf. Coat. Technol. 133-134 (2000) 131–137.

[165] R. Daniel, D. Holec, M. Bartosik, J. Keckes, C. Mitterer, Size effect of thermal expansion and thermal/intrinsic stresses in nanostructured thin films: Experiment and model, Acta Mater. 59 (2011) 6631–6645.

[166] P.H. Mayrhofer, F. Kunc, J. Musil, C. Mitterer, A comparative study on reactive and non-reactive unbalanced magnetron sputter deposition of TiN coatings, Thin Solid Films 415 (2002) 151–159.

[167] D.A. Padmavathi, Potential energy curves & material properties, Mater. Sci. Appl. 22 (2011) 97–104.

[168] W.M. Yim, R.J. Paff, Thermal expansion of AlN, sapphire, and silicon, J. Appl. Phys. 45 (1974) 1456–1457.

[169] M. Halvarsson, V. Langer, S. Vuorinen, Determination of the thermal expansion of κ-Al_2O_3 by high temperature XRD, Surf. Coat. Technol. 76-77 (1995) 358–362.

[170] G.G. Stoney, The tension of metallic films deposited by electrolysis, Proc. R. Soc. A 82 (1909) 172–175.

[171] W.D. Nix, Mechanical properties of thin films, Metall. Trans. A 20A (1989) 2217–2244.

[172] L. Hultman, C. Mitterer, Thermal Stability of Advanced Nanostructured Wear-Resistant Coatings, in: A. Cavaleiro, J.T.M. De Hosson (Eds.), Nanostructured Coatings, Springer, New York, 2006, pp. 464–510.

[173] C. Saringer, M. Tkadletz, C. Mitterer, Restrictions of stress measurements using the curvature method by thermally induced plastic deformation of silicon substrates, Surf. Coat. Technol. 274 (2015) 68–75.

[174] G.A. Slack, S.F. Bartram, Thermal expansion of some diamondlike crystals, J. Appl. Phys. 46 (1975) 89–98.

[175] H. Iwanaga, A. Kunishige, S. Takeuchi, Anisotropic thermal expansion in wurtzite-type crystals, J. Mater. Sci. 35 (2000) 2451–2454.

[176] M.W. Barsoum, C.J. Rawn, T. El-Raghy, A.T. Procopio, W.D. Porter, H. Wang, C.R. Hubbard, Thermal properties of Ti_4AlN_3, J. Appl. Phys. 87 (2000) 8407–8414.

[177] K. Aigner, W. Lengauer, D. Rafaja, P. Ettmayer, Lattice parameters and thermal expansion of $Ti(C_xN_{1-x})$, $Zr(C_xN_{1-x})$, $Hf(C_xN_{1-x})$ and TiN_{1-x} from 298 to 1473 K as investigated by high-temperature X-ray diffraction, J. Alloy. Compd. 215 (1994) 121–126.

[178] H. Kröncke, S. Figge, B.M. Epelbaum, D. Hommel, Determination of the temperature dependent thermal expansion coefficients of bulk AlN by HRXRD, Acta Phys. Pol. A 114 (2008) 1193–1200.

[179] H.M. Rietveld, A profile refinement method for nuclear and magnetic structures, J. Appl. Cryst. 2 (1969) 65–71.

[180] R. Daniel, J. Keckes, I. Matko, M. Burghammer, C. Mitterer, Origins of microstructure and stress gradients in nanocrystalline thin films: The role of growth parameters and self-organization, Acta Mater. 61 (2013) 6255–6266.

[181] L. Braginsky, A. Gusarov, V. Shklover, Models of thermal conductivity of multilayer wear resistant coatings, Surf. Coat. Technol. 204 (2009) 629–634.

[182] P.H.M. Böttger, L. Braginsky, V. Shklover, E. Lewin, J. Patscheider, D.G. Cahill, M. Sobiech, Hard wear-resistant coatings with anisotropic thermal conductivity for high thermal load applications, J. Appl. Phys. 116 (2014) 013507.

[183] D.G. Cahill, S.-M. Lee, T.I. Selinder, Thermal conductivity of κ-Al_2O_3 and α-Al_2O_3 wear-resistant coatings, J. Appl. Phys. (1998).

[184] C. Mitterer, F. Holler, F. Üstel, D. Heim, Application of hard coatings in aluminium die casting - soldering, erosion and thermal fatigue behaviour, Surf. Coat. Technol. 125 (2000) 233–239.

[185] S. Reif-Acherman, Early and current experimental methods for determining thermal conductivities of metals, Int. J. Heat Mass Transf. 77 (2014) 542–563.

[186] Y.K. Koh, S.L. Singer, W. Kim, J.M.O. Zide, H. Lu, D.G. Cahill, A. Majumdar, A.C. Gossard, Comparison of the 3ω method and time-domain thermoreflectance for measurements of the cross-plane thermal conductivity of epitaxial semiconductors, J. Appl. Phys. 105 (2009) 054303.

[187] O.M. Corbino, Thermische Oszillationen wechselstromdurchflossener Lampen mit dünnem Faden und daraus sich ergebende Anwesenheit geradzahliger Oberschwingungen, Phys. Zeitschr 11 (1910) 413–417.

[188] D.G. Cahill, R.O. Pohl, Thermal conductivity of amorphous solids above the plateau, Phys. Rev. B 35 (1987) 4067–4073.

[189] D.G. Cahill, H.E. Fischer, T. Klitsner, E.T. Swartz, R.O. Pohl, Thermal conductivity of thin films: Measurements and understanding, J. Vac. Sci. Technol. A 7 (1989) 1259–1266.

[190] D.G. Cahill, Thermal conductivity measurement from 30 to 750 K: The 3ω method, Rev. Sci. Instrum. 61 (1990) 802–808.

[191] D.G. Cahill, M. Katiyar, J.R. Abelson, Thermal conductivity of a-Si:H thin films, Phys. Rev. B 50 (1994) 6077–6081.

[192] A. Jacquot, F. Vollmer, B. Bayer, M. Jaegle, D.G. Ebling, H. Böttner, Thermal conductivity measurements on challenging samples by the 3 omega method, J. Electron. Mater. 39 (2010) 1621–1626.

[193] J. Alvarez-Quintana, J. Rodríguez-Viejo, Extension of the 3ω method to measure the thermal conductivity of thin films without a reference sample, Sensors Actuat. A Phys. 142 (2008) 232–236.

[194] J.L. Battaglia, C. Wiemer, M. Fanciulli, An accurate low-frequency model for the 3ω method, J. Appl. Phys. 101 (2007) 104510.

[195] K.T. Wojciechowski, R. Zybala, R. Mania, Application of DLC layers in 3-omega thermal conductivity method, J. Achiev. Mater. Manuf. Eng. 37 (2009) 512–517.

[196] S. Ahmed, R. Liske, T. Wunderer, M. Leonhardt, R. Ziervogel, C. Fansler, T. Grotjohn, J. Asmussen, T. Schuelke, Extending the 3ω-method to the MHz range for thermal conductivity measurements of diamond thin films, Diam. Relat. Mater. 15 (2006) 389–393.

[197] C.A. Paddock, G.L. Eesley, Transient thermoreflectance from thin metal films, J. Appl. Phys. 60 (1986) 285–290.

[198] D.A. Young, C. Thomsen, H.T. Grahn, H.J. Maris, J. Tauc, Heat Flow in Glasses on a Picosecond Time Scale, in: A.C. Anderson, J.P. Wolfe (Eds.), Phonon Scattering in Condensed Matter V Springer Series in Solid-State Sciences Volume 68, Springer, Berlin Heidelberg, 1986, pp. 49–51.

[199] C.J. Morath, H.J. Maris, J.J. Cuomo, D.L. Pappas, A. Grill, V. V. Patel, J.P. Doyle, K.L. Saenger, Picosecond optical studies of amorphous diamond and diamondlike carbon: thermal conductivity and longitudinal sound velocity, J. Appl. Phys. 76 (1994) 2636–2640.

[200] W.S. Capinski, H.J. Maris, Improved apparatus for picosecond pump-and-probe optical measurements, Rev. Sci. Instrum. 67 (1996) 2720–2726.

[201] W. Capinski, H. Maris, T. Ruf, M. Cardona, K. Ploog, D. Katzer, Thermal-conductivity measurements of GaAs/AlAs superlattices using a picosecond optical pump-and-probe technique, Phys. Rev. B 59 (1999) 8105–8113.

[202] D.G. Cahill, Analysis of heat flow in layered structures for time-domain thermoreflectance, Rev. Sci. Instrum. 75 (2004) 5119–5122.

[203] D.G. Cahill, W.K. Ford, K.E. Goodson, G.D. Mahan, A. Majumdar, H.J. Maris, R. Merlin, S.R. Phillpot, Nanoscale thermal transport, J. Appl. Phys. 93 (2003) 793–818.

[204] Y. Wang, J.Y. Park, Y.K. Koh, D.G. Cahill, Thermoreflectance of metal transducers for time-domain thermoreflectance, J. Appl. Phys. 108 (2010) 043507.

[205] G.S. Fox-Rabinovich, K. Yamamoto, M.H. Aguirre, D.G. Cahill, S.C. Veldhuis, A. Biksa, G. Dosbaeva, L.S. Shuster, Multi-functional nano-multilayered AlTiN/Cu PVD coating for machining of Inconel 718 superalloy, Surf. Coat. Technol. 204 (2010) 2465–2471.

[206] R. Rachbauer, J.J. Gengler, A.A. Voevodin, K. Resch, P.H. Mayrhofer, Temperature driven evolution of thermal, electrical, and optical properties of Ti-Al-N coatings, Acta Mater. 60 (2012) 2091–2096.

[207] X.Z. Ding, M.K. Samani, G. Chen, Thermal conductivity of PVD TiAlN films using pulsed photothermal reflectance technique, Appl. Phys. A Mater. Sci. Process. 101 (2010) 573–577.

[208] M.K. Samani, G.C.K. Chen, X.Z. Ding, X.T. Zeng, Thermal conductivity of CrAlN and TiAlN coatings deposited by lateral rotating cathode arc, Key Eng. Mater. (2010).

[209] P.H.M. Böttger, E. Lewin, J. Patscheider, V. Shklover, D.G. Cahill, R. Ghisleni, M. Sobiech, Thermal conductivity of hard oxynitride coatings, Thin Solid Films 549 (2013) 232–238.

[210] H.A. Alwi, R. Abd-Shukor, Measurement of thermophysical properties of $YBa_2Cu_3O_{7-x}$ thin film using picosecond thermoreflectance technique, Physica C 471 (2011) 26–28.

[211] H.A. Alwi, Y.Y. Kim, R. Awang, S.A. Rahman, S. Krishnaswamy, Measurement of thermophysical properties of hydrogenated amorphous carbon thin films using picosecond thermoreflectance technique, Int. J. Heat Mass Transf. 63 (2013) 199–203.

[212] J.L. Battaglia, A. Kusiak, C. Rossignol, N. Chigarev, Thermal diffusivity and effusivity of thin layers using time-domain thermoreflectance, Phys. Rev. B 76 (2007) 184110.

[213] D. Windover, E. Barnat, J.Y. Kim, M. Nielsen, T. Lu, A. Kumar, H. Bakhru, Thin film density determination by multiple radiation energy dispersive X-ray reflectivity, Adv. X-Ray Anal. 42 (2000) 590–600.

[214] C.A. Cerdeiriña, J.A. Míguez, E. Carballo, C.A. Tovar, E. de la Puente, L. Romaní, Highly precise determination of the heat capacity of liquids by DSC: calibration and measurement, Thermochim. Acta 347 (2000) 37–44.

[215] G. Della Gatta, M.J. Richardson, S.M. Sarge, S. Stølen, Standards, calibration, and guidelines in microcalorimetry. Part 2. Calibration standards for differential scanning calorimetry** (IUPAC Technical Report), Pure Appl. Chem. 78 (2006) 1455–1476.

[216] D. Ditmars, S. Ishihara, S.S. Chang, G. Bernstein, E.D. West, Enthalpy and heat-capacity standard reference material: synthetic sapphire (α-Al_2O_3) from 10 to 2250 K, J. Res. Natl. Bur. Stand. (1934). 87 (1982) 159–163.

[217] W. Hemminger, S.M. Sarge, Calibration as an aspect of quality assurance in differential scanning calorimetry (DSC) measurements, Thermochim. Acta 245 (1994) 181–187.

[218] S.M. Sarge, G.W.H. Höhne, H.K. Cammenga, W. Eysel, E. Gmelin, Temperature, heat and heat flow rate calibration of scanning calorimeters in the cooling mode, Thermochim. Acta 361 (2000) 1–20.

[219] B. Smetana, M. Žaludová, S. Zlá, J. Dobrovská, P. Klus, S. Rosypalová, Possibilities of heat capacity measurement of metallic systems, Proc. Met. 2012, Brno, Czech Repub. (2012) 1–6.

[220] NIST - Titanium Nitride, http://webbook.nist.gov/cgi/cbook.cgi?ID=C25583204&Type=JANAFS&Table=on, accessed June 2015.

[221] NIST - Aluminum Nitride, http://webbook.nist.gov/cgi/cbook.cgi?ID=C24304005&Type=JANAFS&Table=on#JANAFS, accessed June 2015.

[222] J. Leitner, P. Voňka, D. Sedmidubský, P. Svoboda, Application of Neumann-Kopp rule for the estimation of heat capacity of mixed oxides, Thermochim. Acta 497 (2010) 7–13.

[223] J. Leitner, P. Chuchvalec, D. Sedmidubský, A. Strejc, P. Abrman, Estimation of heat capacities of solid mixed oxides, Thermochim. Acta 395 (2003) 27–46.

[224] N. Schalk, C. Mitterer, J. Keckes, M. Penoy, C. Michotte, Influence of residual stresses and grain size on the spinodal decomposition of metastable $Ti_{1-x}Al_xN$ coatings, Surf. Coat. Technol. 209 (2012) 190–196.

[225] R.W. Cheary, A. Coelho, Fundamental parameters approach to x-ray line-profile fitting, J. Appl. Cryst. 25 (1992) 109–121.

[226] A. Le Bail, Whole powder pattern decomposition methods and applications: A retrospection, Powder Diffr. 20 (2005) 316–326.